AD-A074 141 BELL HELICOPTER TEXTRON FORT WORTH TX F/G 1/3
ANALYSIS OF LOW-SPEED HELICOPTER FLIGHT TEST DATA.(U)
AUG 79 J L TANGLER DAAJ02-77-C-0022
UNCLASSIFIED BHT-699-099-103 USARTL-TR-79-19 NL

1 OF 2
AD A074141

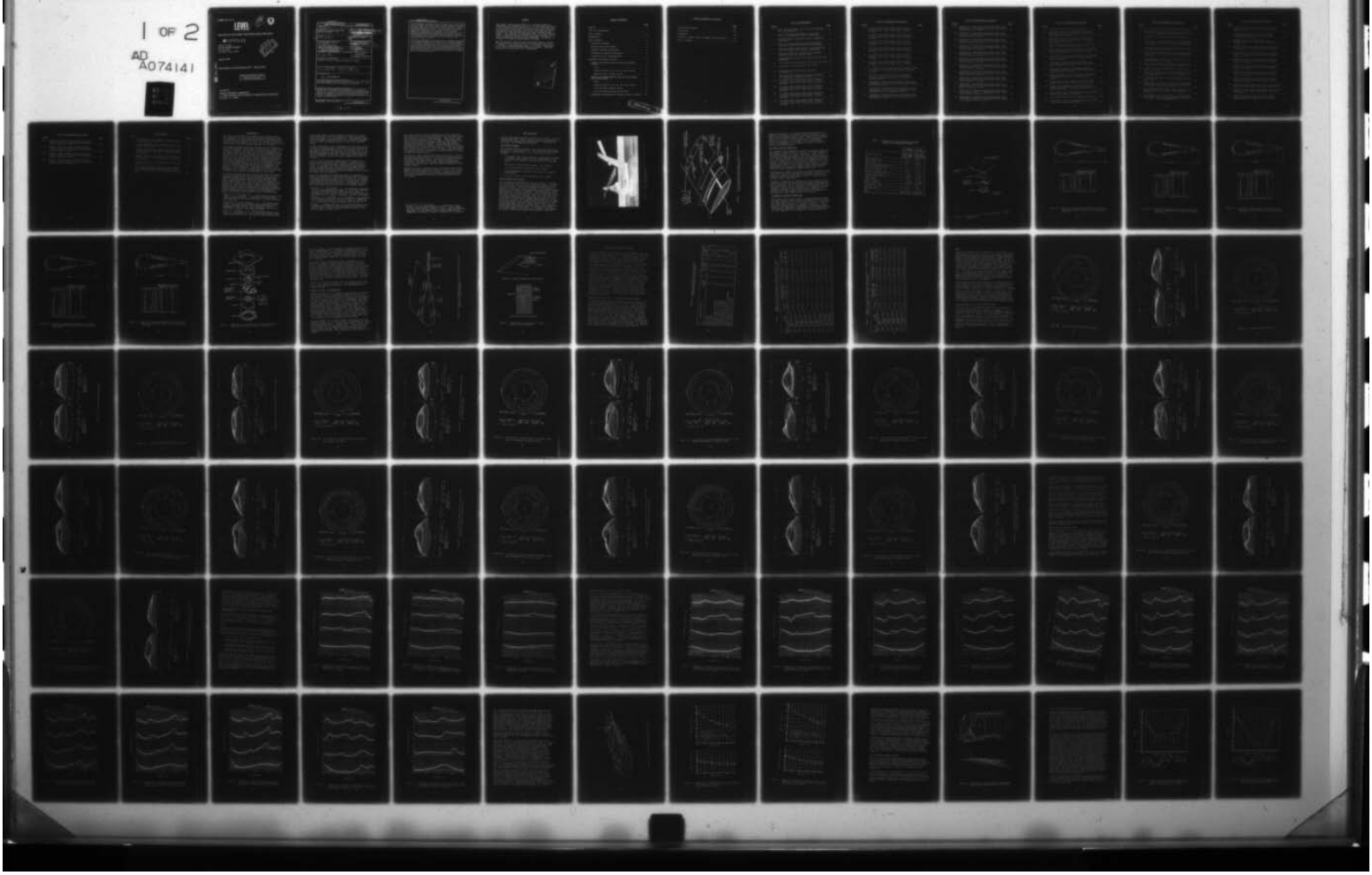

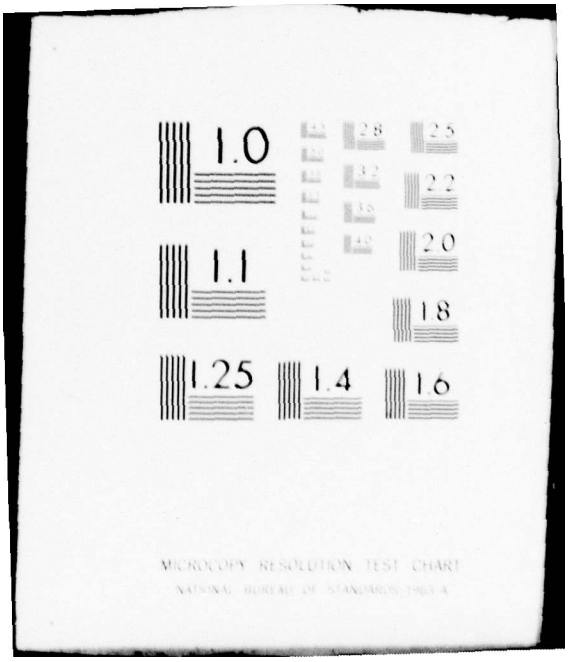
1.0
1.1
1.25
1.4
1.6
2.8
2.5
2.2
2.0
1.8
MICROCOPY RESOLUTION TEST CHART
NATIONAL BUREAU OF STANDARDS 1963-A

USARTL-TR-79-19

LEVEL II

ANALYSIS OF LOW-SPEED HELICOPTER FLIGHT TEST DATA

AD A074141

James L. Tangler
BELL HELICOPTER TEXTRON
P. O. Box 482
Fort Worth, Texas 76101

August 1979

Final Report for Period March 1977 - March 1979

Approved for public release;
distribution unlimited.

Prepared for

APPLIED TECHNOLOGY LABORATORY
U. S. ARMY RESEARCH AND TECHNOLOGY LABORATORIES (AVRADCOM)
Fort Eustis, Va. 23604

UNCLASSIFIED

SECURITY CLASSIFICATION OF THIS PAGE (When Data Entered)

REPORT DOCUMENTATION PAGE	READ INSTRUCTIONS BEFORE COMPLETING FORM
1. REPORT NUMBER: USARTL-TR-79-19	2. GOVT ACCESSION NO. / 3. RECIPIENT'S CATALOG NUMBER
4. TITLE (and Subtitle): ANALYSIS OF LOW-SPEED HELICOPTER FLIGHT TEST DATA	5. TYPE OF REPORT & PERIOD COVERED: Final Report, Mar 77-MAR 79; 6. PERFORMING ORG. REPORT NUMBER: 699-099-103
7. AUTHOR(s): James L. Tangler	8. CONTRACT OR GRANT NUMBER(s): DAAJ02-77-C-0022
9. PERFORMING ORGANIZATION NAME AND ADDRESS: Bell Helicopter Textron, P. O. Box 482, Fort Worth, Texas 76101	10. PROGRAM ELEMENT, PROJECT, TASK AREA & WORK UNIT NUMBERS: 1L262209AH76 00 191 EK
11. CONTROLLING OFFICE NAME AND ADDRESS: Applied Technology Laboratory, U.S. Army Research and Technology Laboratories (AVRADCOM), Ft. Eustis, Virginia 23604	12. REPORT DATE: August 1979; 13. NUMBER OF PAGES: 153
14. MONITORING AGENCY NAME & ADDRESS (if different from Controlling Office): 154 p.	15. SECURITY CLASS. (of this report): UNCLASSIFIED; 15a. DECLASSIFICATION/DOWNGRADING SCHEDULE

16. DISTRIBUTION STATEMENT (of this Report)

Approved for public release; distribution unlimited.

17. DISTRIBUTION STATEMENT (of the abstract entered in Block 20, if different from Report)

USARTL TR-79-19

18. SUPPLEMENTARY NOTES

BHT-699-099-103

19. KEY WORDS (Continue on reverse side if necessary and identify by block number)

Helicopter Blade Loads, Rotor Pressure Distributions, NOE Flight Test, NOE Maneuvers, Rotor Blade/Vortex Interaction

20. ABSTRACT (Continue on reverse side if necessary and identify by block number)

The purpose of this study was to investigate the aerodynamic behavior of a helicopter rotor operating in the low-speed flight regime, particularly in the nap-of-the-earth (NOE) evasive mode. The effort consisted of reducing and analyzing existing AH-1G flight test response data acquired for simulated NOE flight under Contract DAAJ02-73-C-0105. → over

DD FORM 1 JAN 73 1473 EDITION OF 1 NOV 65 IS OBSOLETE

UNCLASSIFIED

SECURITY CLASSIFICATION OF THIS PAGE (When Data Entered)

054200

Data presentation includes steady state speed power polars, blade force and moment coefficients versus azimuth, contour and surface plots of normal force coefficients, control positions, fuselage attitudes, and teetering angles. Time histories of load factor and control positions as well as contour and surface plots of normal force coefficient are presented for the low-speed maneuvers. Measured data are compared to data calculated using blade element and prescribed wake analyses. Specific areas of interest analyzed in this study include blade/vortex interaction at 50 knots and angle-of-attack data derived from hot-wire measurements taken in hover.

Major points concluded from this study are: reasonable estimates of net rotor performance can be obtained from classical methodology (however, detailed blade loading cannot be obtained without a more accurate representation of the nonuniform induced downwash); deficiencies of the flight test data warrant only qualitative comparisons with calculated data; and two-dimensional wind tunnel tests would be desirable in determining the accuracy of analytical methods of relating angle of attack and stagnation point location measured with hot-wire sensors.

PREFACE

This report contains the results of a research program to investigate the aerodynamic behavior of a helicopter operating in the low-speed flight regime, particularly in the NOE (nap-of-the-earth) evasive mode. The effort consisted of reducing and analyzing the existing AH-1G flight test response data acquired for simulated NOE maneuvers under Contract DAAJ02-73-C-0105. This program was conducted by Bell Helicopter Textron (BHT) for Applied Technology Laboratory (ATL), US Army Research and Technology Laboratories (AVRADCOM), from March 1977 to March 1979 under Contract DAAJ02-77-C-0022.

The ATL technical direction was provided by Robert P. Smith. This program was conducted under the technical direction of J. L. Tangler, Project Engineer, and J. D. Kocurek, Group Supervisor, Basic Technology Aerodynamics Development. Technical assistance was provided by N. K. McMennamy.

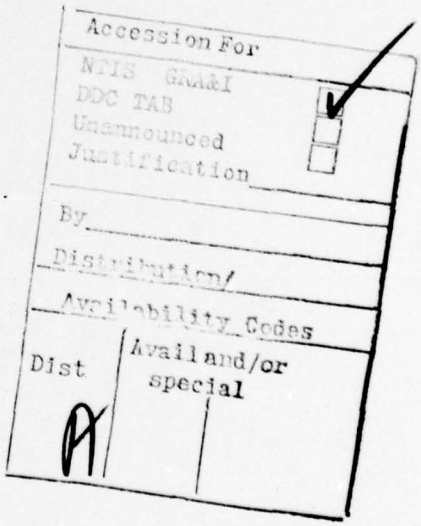

TABLE OF CONTENTS

	Page
PREFACE	3
LIST OF ILLUSTRATIONS	7
LIST OF TABLES	14
INTRODUCTION	15
TEST EQUIPMENT	18
HELICOPTER AIRFRAME	18
MODIFIED MAIN ROTOR BLADES	18
ABSOLUTE PRESSURE TRANSDUCERS	21
DIFFERENTIAL PRESSURE TRANSDUCERS	21
STAGNATION POINT INSTRUMENTATION	30
LOW-SPEED STEADY-STATE FLIGHTS	33
CONTOUR AND SURFACE PLOTS FOR THE STEADY-STATE FLIGHTS	33
Hover	37
Forward Flight 10, 20, 30, 40, and 50 Knots	37
Right and Left Sideward Flight	66
COMPARISON BETWEEN MEASURED AND PREDICTED NORMAL FORCE COEFFICIENTS	71
Hover	71
Forward Flight 10, 20, 30, 40, and 50 Knots	75
Left and Right Sideward Flight	92
Local Flow and Direction at 50 Knots	94
COMPARISON OF MEASURED AND PREDICTED ANGLE OF ATTACK	101

TABLE OF CONTENTS (Concluded)

	Page
NOE MANEUVER FLIGHTS.	103
CONCLUSIONS	134
REFERENCES.	135
APPENDIX A, ROTOR FORCE AND MOMENT COEFFICIENT DATA . . .	136
LIST OF SYMBOLS	152

LIST OF ILLUSTRATIONS

Figure		Page
1	AH-1G test helicopter with the rotor environment test instrumentation.	19
2	AH-1G rotor blade modification, wiring and typical instrumentation sleeve installation	20
3	Component parts of absolute pressure transducer installation.	23
4	Main rotor blade absolute pressure transducer locations, pressure ranges, and identification. . .	24
5	Component parts of BLB velocity gage installation using two differential pressure transducers	29
6	Main rotor blade BLB velocity gage locations, pressure ranges, and identification	31
7	Installation and location of leading edge hot-wire anemometer.	32
8	C_N contour and surface plots (OGE hover at 50 feet)	38
9	C_N contour and surface plots (IGE hover).	40
10	C_N contour and surface plots (OGE hover at 100 feet).	42
11	C_N contour and surface plots (hover 360-degree turn record at 0 degree at 50 feet)	44
12	C_N contour and surface plots (level flight at 10 knots, gross weight 8100 pounds, altitude 50 feet).	46
13	C_N contour and surface plots (level flight at 10 knots, gross weight 9000 pounds, altitude 50 feet).	48
14	C_N contour and surface plots (level flight at 20 knots, gross weight 8100 pounds, altitude 50 feet).	50
15	C_N contour and surface plots (level flight at 20 knots, gross weight 9000 pounds, altitude 50 feet).	52

LIST OF ILLUSTRATIONS (Continued)

Figure		Page
16	C_N contour and surface plots (level flight at 30 knots, gross weight 8100 pounds, altitude 50 feet)	54
17	C_N contour and surface plots (level flight at 30 knots, gross weight 9000 pounds, altitude 50 feet)	56
18	C_N contour and surface plots (level flight at 40 knots, gross weight 8100 pounds, altitude 50 feet)	58
19	C_N contour and surface plots (level flight at 40 knots, gross weight 9000 pounds, altitude 50 feet)	60
20	C_N contour and surface plots (level flight at 50 knots, gross weight 8100 pounds, altitude 50 feet)	62
21	C_N contour and surface plots (level flight at 50 knots, gross weight 9000 pounds, altitude 50 feet)	64
22	C_N contour and surface plots (right sideward flight at 30 knots, gross weight 8100 pounds, altitude 50 feet)	67
23	C_N contour and surface plots (left sideward flight at 30 knots, gross weight 8100 pounds, altitude 50 feet)	69
24	Comparison of measured and predicted normal force coefficients, record 723, 8100 pounds gross weight, OGE hover at 100 feet	72
25	Comparison of measured and predicted normal force coefficients, record 736, 8100 pounds gross weight, 360-degree turn at 0 degrees at 50 feet	73
26	Comparison of measured and predicted normal force coefficients, record 685, 9000 pounds gross weight, OGE hover at 50 feet	74

LIST OF ILLUSTRATIONS (Continued)

Figure		Page
27	Comparison of measured and predicted normal force coefficients, record 724, 8100 pounds gross weight, forward flight at 10 knots	76
28	Comparison of measured and predicted normal force coefficients, record 686, 9000 pounds gross weight, forward flight at 10 knots	77
29	Comparison of measured and predicted normal force coefficients, record 725, 8100 pounds gross weight, forward flight at 20 knots	78
30	Comparison of measured and predicted normal force coefficients, record 687, 9000 pounds gross weight, forward flight at 20 knots	79
31	Comparison of measured and predicted normal force coefficients, record 726, 8100 pounds gross weight, forward flight at 30 knots	80
32	Comparison of measured and predicted normal force coefficients, record 688, 9000 pounds gross weight, forward flight at 30 knots	81
33	Comparison of measured and predicted normal force coefficients, record 727, 8100 pounds gross weight, forward flight at 40 knots	82
34	Comparison of measured and predicted normal force coefficients, record 689, 9000 pounds gross weight, forward flight at 40 knots	83
35	Comparison of measured and predicted normal force coefficients, record 728, 8100 pounds gross weight, forward flight at 50 knots	84
36	Comparison of measured and predicted normal force coefficients, record 690, 9000 pounds gross weight, forward flight at 50 knots	85
37	Comparison of measured and predicted normal force coefficients, record 717, 8100 pounds gross weight, right sideward flight at 30 knots.	86
38	Comparison of measured and predicted normal force coefficients, record 720, 8100 pounds gross weight, left sideward flight at 30 knots	87

LIST OF ILLUSTRATIONS (Continued)

Figure		Page
39	Calculated distorted wake at 50 knots.	89
40	Comparison of measured and predicted main rotor power and collective pitch from 0 to 50 knots, 8100 pounds gross weight	90
41	Comparison of measured and predicted main rotor power and collective pitch from 0 to 50 knots, 9000 pounds gross weight	91
42	Distorted tip vortex geometry, 9000 pounds gross weight, forward flight at 50 knots	93
43	Lower surface flow direction measured at r/R=0.864, record 690, 9000 pounds gross weight, forward flight at 50 knots	95
44	Upper surface flow direction measured at r/R=0.864, record 690, 9000 pounds gross weight, forward flight at 50 knots	96
45	Lower surface resultant velocity measured at r/R=0.864, record 690, 9000 pounds gross weight, forward flight at 50 knots	97
46	Upper surface resultant velocity measured at r/R=0.864, record 690, 9000 pounds gross weight, forward flight at 50 knots	98
47	Measured chordwise force coefficient, record 690, 9000 pounds gross weight, forward flight at 50 knots	99
48	Measured moment coefficients, record 690, 9000 pounds gross weight, forward flight at 50 knots. . .	100
49	Comparison of measured and calculated angle of attack, record 723, 8100 pounds gross weight, OGE hover at 100 feet.	102
50	Load factor, cyclic and collective stick positions versus time (pop-up IGE to OGE).	105
51	C_N contour and surface plots (pop-up IGE to OGE) . .	106
52	Load factor, cyclic and collective stick positions versus time (pop-up NOE to OGE).	108

LIST OF ILLUSTRATIONS (Continued)

Figure		Page
53	C_N contour and surface plots (pop-up NOE to OGE)	109
54	Load factor, cyclic and collective stick positions versus time (descent from OGE to IGE)	111
55	C_N contour and surface plots (descent from OGE to IGE)	112
56	Load factor, cyclic and collective stick positions versus time (90-degree right turn and acceleration to 70 knots)	114
57	C_N contour and surface plots (90-degree right turn and acceleration to 70 knots)	115
58	Load factor, cyclic and collective stick positions versus time (90-degree left turn and acceleration to 70 knots)	119
59	C_N contour and surface plots (90-degree left turn and acceleration to 70 knots)	120
60	Load factor, cyclic and collective stick positions versus time (decelerate 50 knots to OGE hover)	122
61	C_N contour plot and surface plots (decelerate 50 knots to OGE hover)	123
62	Load factor, cyclic and collective stick positions versus time (decelerate 50 knots to OGE hover - level attitude)	125
63	C_N contour and surface plots (decelerate 50 knots to OGE hover)	126
64	Load factor, cyclic and collective stick positions versus time (directional reversal and acceleration to 30 knots - left sideward flight)	128
65	C_N contour and surface plots (directional reversal and acceleration to 30 knots - left sideward flight)	129
66	Load factor, cyclic and collective stick positions versus time (directional reversal and acceleration to 30 knots - right sideward flight)	131

LIST OF ILLUSTRATIONS (Continued)

Figure		Page
67	C_N contour plot and surface plots (directional reversal and acceleration to 30 knots - right sideward flight)	132
A-1	Comparison of measured and predicted normal force coefficient, record 722, 8100 pounds gross weight, IGE hover.	137
A-2	Measured chord force coefficient versus azimuth, record 722, 8100 pounds gross weight, IGE hover.	138
A-3	Measured chord force coefficient versus azimuth, record 723, 8100 pounds gross weight, OGE hover at 100 feet.	139
A-4	Measured chord force coefficient versus azimuth, record 724, 8100 pounds gross weight, forward flight at 10 knots	140
A-5	Measured chord force coefficient versus azimuth, record 725, 8100 pounds gross weight, forward flight at 20 knots	141
A-6	Measured chord force coefficient versus azimuth, record 726, 8100 pounds gross weight, forward flight at 30 knots	142
A-7	Measured chord force coefficient versus azimuth, record 727, 8100 pounds gross weight, forward flight at 40 knots	143
A-8	Measured chord force coefficient versus azimuth, record 728, 8100 pounds gross weight, forward flight at 50 knots	144
A-9	Measured pitching moment coefficient versus azimuth, record 722, 8100 pounds gross weight, IGE hover.	145
A-10	Measured pitching moment coefficient versus azimuth, record 723, 8100 pounds gross weight, OGE hover at 100 feet.	146
A-11	Measured pitching moment coefficient versus azimuth, record 724, 8100 pounds gross weight, forward flight at 10 knots	147

LIST OF ILLUSTRATIONS (Concluded)

Figure		Page
A-12	Measured pitching moment coefficient versus azimuth, record 725, 8100 pounds gross weight, forward flight at 20 knots.	148
A-13	Measured pitching moment coefficient versus azimuth, record 726, 8100 pounds gross weight, forward flight at 30 knots.	149
A-14	Measured pitching moment coefficient versus azimuth, record 727, 8100 pounds gross weight, forward flight at 40 knots.	150
A-15	Measured pitching moment coefficient versus azimuth, record 728, 8100 pounds gross weight, forward flight at 50 knots.	151

LIST OF TABLES

Table		Page
1	COMPARISON OF ROTOR PARAMETERS BETWEEN STANDARD AND GLOVED AH-1G ROTORS	22
2	FLIGHT CONDITIONS AND RECORD NUMBERS FOR THE NOE STEADY-STATE FLIGHTS.	34
3	SUMMARY OF MAIN ROTOR TORQUE, FUSELAGE ATTITUDE, CONTROL POSITION, AND HUB FLAPPING, 8100 POUNDS GROSS WEIGHT.	35
4	SUMMARY OF MAIN ROTOR TORQUE, FUSELAGE ATTITUDE, CONTROL POSITION, AND HUB FLAPPING, 9000 POUNDS GROSS WEIGHT.	36
5	FLIGHT CONDITIONS AND RECORD NUMBERS FOR THE NOE MANEUVER FLIGHTS.	104
A-1	NOE STEADY FLIGHT CONDITIONS AND RECORD NUMBERS FOR PRESENTED NORMAL FORCE COEFFICIENT, CHORD FORCE COEFFICIENT AND PITCHING MOMENT COEFFICIENT DATA.	136

INTRODUCTION

The use of a helicopter in a combat role can require extensive operation in a low-speed, terrain-following flight region. This technique is used to minimize exposure of the helicopter to enemy detection and hostile fire. Called nap-of-the-earth (NOE) flight, this regime also coincides with the forward flight transition region which extends from hover to 60 knots.

The transition region shares the complexities of aerodynamic environment normally associated with either hover, level flight cruise, or maneuver. As in hover, an accurate prediction of the blade loading is dependent on an accurate determination of the wake-induced inflow. The wake structure and behavior thus dictate not only the induced power associated with the inflow field, but also, through blade loading, the power required to overcome airfoil profile drag. Further complicating the problem in the low-speed flight region are the numerous blade/vortex interactions that occur. As in forward flight or maneuver, the nonsteady character of the wake in proximity to the rotor in transition further complicates the aerodynamic environment to the extent that a conclusive assessment of its impact on rotor performance, loads, and vibration is indeed a formidable task. However, such assessment is an integral part of improving the predictive methodology in those areas.

To provide the needed insight as to how the flow field about the rotor varies for both hover and forward flight conditions, including the NOE region, several Bell Helicopter Textron (BHT) and Army-sponsored research programs have been undertaken. Beginning in 1965, the first of these (Reference 1) studied the boundary layer and flow field of a hovering rotor. This effort indicated the need for special instrumentation to measure and record the helicopter rotor's flow environment. Through follow-on research programs, the necessary instrumentation needed to survey a rotor's flow field was designed and tested. References 2 and 3 document the development of a blade surface-flow measuring sensor, known as the boundary

---

[1]Tanner, W. H., and Yaggy, P. F., "Experimental Boundary Layer Study of Hovering Rotors, " presented at the 22nd Annual National Forum of the American Helicopter Society, Washington D.C., May 1966.

[2]Tanner, W. H., and Van Wyckhouse, J. F., "Wind Tunnel Tests of Full-Scale Rotors Operating at High Advancing Tip Mach Numbers and Advance Ratios," Bell Helicopter Textron, USAAVLABS TR68-44, US Army Aviation Materiel Laboratories, Fort Eustis, Virginia, July 1968, AD 674188.

[3]Burpo, F., and Tanner, W. H., "Two-Dimensional Tests of Advanced Instrumentation for Rotors," Bell Helicopter Company Report Number 606-099-001, Fort Worth, Texas, December 1968.

layer button (BLB), which provides the capability for measuring both flow velocity and direction. Also discussed in these references is the development of a leading-edge stagnation point sensor comprised of an array of hot-wire anemometers to relate the stagnation point to the local angle of attack.

In 1969 a UH-1H main rotor instrumented at one radial station with BLBs, hot-wire sensors, and static pressure transducers was tested in the NASA Ames 40- by 80-foot wind tunnel.[4] An important finding of this test was that differential pressure measurements between upper and lower surface mask the detail of the aerodynamic environment. These tests established the need for separate, absolute pressure transducers on the two surfaces.

In 1971 a whirl stand test demonstrated the feasibility of using a time division multiplex system to transfer large quantities of aerodynamic data through a space-limited slip ring.[5] In the same time frame, subminiature signal conditioners and voltage controlled oscillators became available, permitting BHT to develop an improved frequency division multiplex system that provides improved signal-to-noise ratios and fewer slip ring elements.[6]

Using the technology previously developed, a comprehensive flight test program was conducted by BHT under US Army sponsorship during the period of June 1974 to April 1976. A heavily instrumented AH-1G helicopter rotor was flight tested through a wide range of operating conditions. The objective of this investigation was to record the rotor's aerodynamic environment, associated controls positions, and airframe response.

---

[4] Shockey, G. A., and Bowden, T. H., "A Wind-Tunnel Investigation of the Aerodynamic Environment of a Full-Scale Helicopter Rotor in Forward Flight," Bell Helicopter Textron, USAAVLABS TR 70-35, Eustis Directorate, US Army Air Mobility R&D Laboratory, Fort Eustis, Virginia, July 1970, AD 875744.

[5] Shockey, G. A., and Bowden, T. H., "Evaluation of an Advanced Instrumentation System for Helicopter Rotors," USAAMRDL TR 71-72, Eustis Directorate, US Army Air Mobility R&D Laboratory, Fort Eustis, Virginia, February 1972, AD 740773.

[6] Goodman, J., "Buildup and Test of a Rotating Frequency Division Multiplex System for Data Transmission from Rotating Systems," Bell Helicopter Company Report 0072R-001, Fort Worth, Texas, 5 January 1972.

The flight conditions can be divided into three categories: basic operational conditions, NOE conditions, and those associated with main rotor noise measurements. The analog flight test data were digitized onto 175 tapes. These tapes constitute a library of well-cataloged flight test data ready to be analyzed and compared to present aerodynamic and dynamic performance prediction methods. A data management program recently developed under Contract DAAJ02-77-C-0053 facilitates data extraction, processing, and reduction.[7] The data management program consists of a variety of computer programs that can present pertinent parameters in various formats, including surface and contour plots.

The purpose of the research described herein was to investigate the aerodynamic behavior of a helicopter operating in the low-speed, NOE flight region. The effort consisted of reducing the existing AH-1G flight test data for these flight conditions. The analysis included comparisons between predicted and measured blade loads with special emphasis on wake induced effects.

Appendix A presents chordwise force coefficient and pitching moment data versus azimuth for hover, 10, 20, 30, 40, and 50 knots at a gross weight of 8100 pounds. Normal force coefficient data is presented only for IGE hover because data for the other above-mentioned cases are presented and discussed in the text.

---

[7]Philbrick, R. B., and Eubanks, A. L., "Operational Loads Survey - Data Management System," Volume I - User's Manual, Bell Helicopter Textron, USARTL TR 78-52A, Applied Technology Laboratory, US Army Research and Technology Laboratories (AVRADCOM), Fort Eustis, Virginia, January 1979, AD A065129.

TEST EQUIPMENT

The test equipment consisted of an AH-1G helicopter, a set of modified main rotor blades, numerous types of transducers, a rotating FM frequency-division multiplex, a stationary FM multiplex, and a shipboard tape deck.

HELICOPTER AIRFRAME

The airframe, shown in Figure 1, was a bailed US Army AH-1G helicopter, Serial Number 20391. In addition to the standard equipment in the helicopter, the following items were installed:

- A 28-track, AR-728 tape recorder, a stationary multiplex, a telemetry (TM) transmitter, and power supplies, all mounted on an equipment rack and installed in the ammo bay.
- Twenty-two accelerometers mounted on the fuselage.
- A rotating multiplex mounted on the trunnion.
- A nose boom mounted forward of the ship for airspeed measurements.
- A hot-wire fault indicator mounted in the cockpit.

MODIFIED MAIN ROTOR BLADES

The "gloved blade" approach was used to maintain a structurally sound rotor and a smooth aerodynamic surface. All rotating transducers and associated wiring were embedded within the glove contour. The glove extended from the root-end doublers to the blade tip and consisted of an aluminum leading edge and thin fiberglass afterbody skins supported by a Nomex honeycomb core, as seen in Figure 2. The leading-edge abrasion strip was stretch-formed aluminum alloy, using the standard blade as the stretch fixture. The glove skins were made of pre-preg fiberglass cloth approximately 0.008 inch thick and bonded to 0.10-inch-thick Nomex honeycomb prior to installation on the blade. Five aluminum sleeves housing the transducers and sensors were wrapped around the airfoil at the selected measurement stations. These sleeves mated with the leading-edge strip and the afterbody skins. The sleeves were roll-formed from aluminum sheet. Two aluminum attachment strips were bonded to the blade at each station and served as nut plates to which the sleeves were fastened. After the

Figure 1. AH-1G test helicopter with the rotor environment test instrumentation.

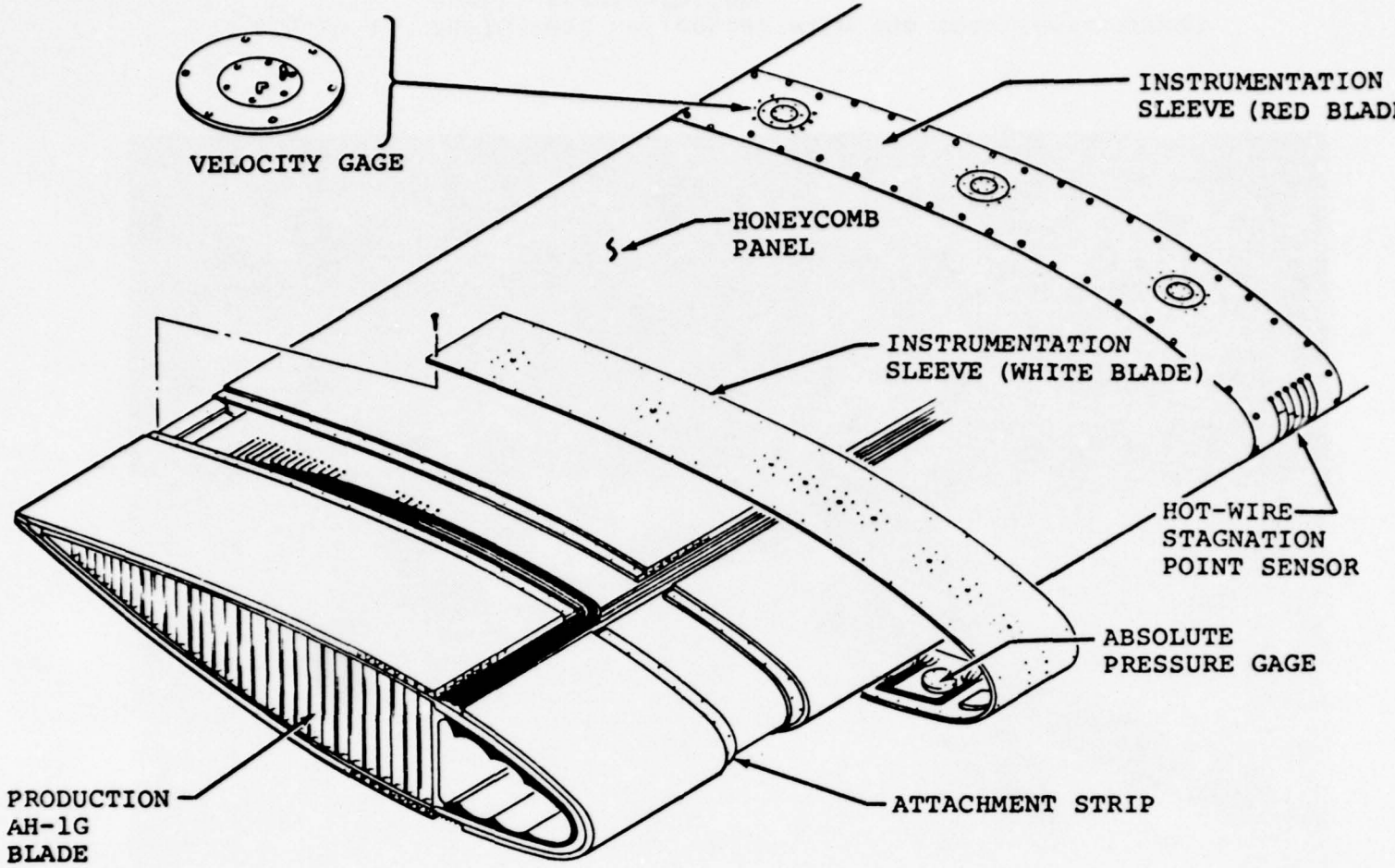

Figure 2. AH-1G rotor blade modification, wiring and typical instrumentation sleeve installation.

blades were painted, the aluminum instrumentation sleeve assemblies containing the absolute pressure transducers, the BLBs, and the hot-wire sensors were fastened to the attachment strips with flat-head machine screws. The final glove thickness was 0.130 inch. The trailing edge was extended 1.5 inches, terminating in a thickness of 0.10 inch. Table 1 gives the parameters for the production AH-1G blade and the gloved instrumented blade.

ABSOLUTE PRESSURE TRANSDUCERS

The aluminum sleeve assemblies, mounted around the contour of the blade at each of the five stations, house the transducers. Each assembly consists of three main parts: outer sleeve, transducer chamber, and gasket. The outer sleeve is a piece of 0.025-inch, 2024-T3 aluminum sheet rolled to the blade contour. The appropriate static ports and attachment holes are drilled in this sleeve. The transducer chamber contains the pressure transducer cavity milled on the top side. It is attached to the underside of the outer sleeve with six countersunk machine screws. A soft rubber gasket seals the attachment between the transducer chamber and the outer sleeve. Details of this assembly are shown in Figure 3.

One-hundred-ten subminiature absolute-pressure transducers were used to measure static pressure on the upper and lower airfoil surfaces. Figures 4-a through 4-e identify locations and pressure ranges for blade stations 40, 60, 75, 86.4 and 95.5 percent radius, respectively.

Pressure transducers are concentrated at the outboard radial stations to record the major pressure peaks and the important shock formations. The 52 pressure transducers located at the two outboard stations are recorded on the 400-Hertz response channels. Hence, events occurring within approximately five degrees of change in rotor azimuth can be measured. At a given station, the chordwise distribution of transducers on the upper and lower blade surfaces is the same.

DIFFERENTIAL PRESSURE TRANSDUCERS

The boundary layer button (BLB), a pressure measuring device, is used to measure flow direction and magnitude on the upper and lower blade surfaces. The BLB consists of two total pressure tubes and a static port, as seen in Figure 5. Each of the total pressure tubes is connected to the top of a diaphragm of the temperature-compensated, subminiature differential pressure transducer. The backsides of the diaphragms of the two transducers are connected to a common static port.

TABLE 1. COMPARISON OF ROTOR PARAMETERS BETWEEN STANDARD AND GLOVED AH-1G ROTORS

	Standard AH-1G Rotor	Gloved AH-1G Rotor
Airfoil Section	Stretched, Slab Sided, NACA 0012	Stretched, Slab Sided, Gloved, 0012
Rotor Radius, ft	22.0	22.0
Blade Chord, in.	27.0	28.63
Trailing Edge Extension, in.	--	1.5
Airfoil Thickness, in.	2.52	2.78
Airfoil Thickness Ratio, %	9.33	9.71
Leading Edge Radius, in.	1.229	1.596
Aspect Ratio	9.78	9.22
Rotor Solidity	0.0651	0.0690
Linear Twist, deg	-10.0	-10.0
Precone, deg	2.75	2.75
Hub	Teetering	Teetering

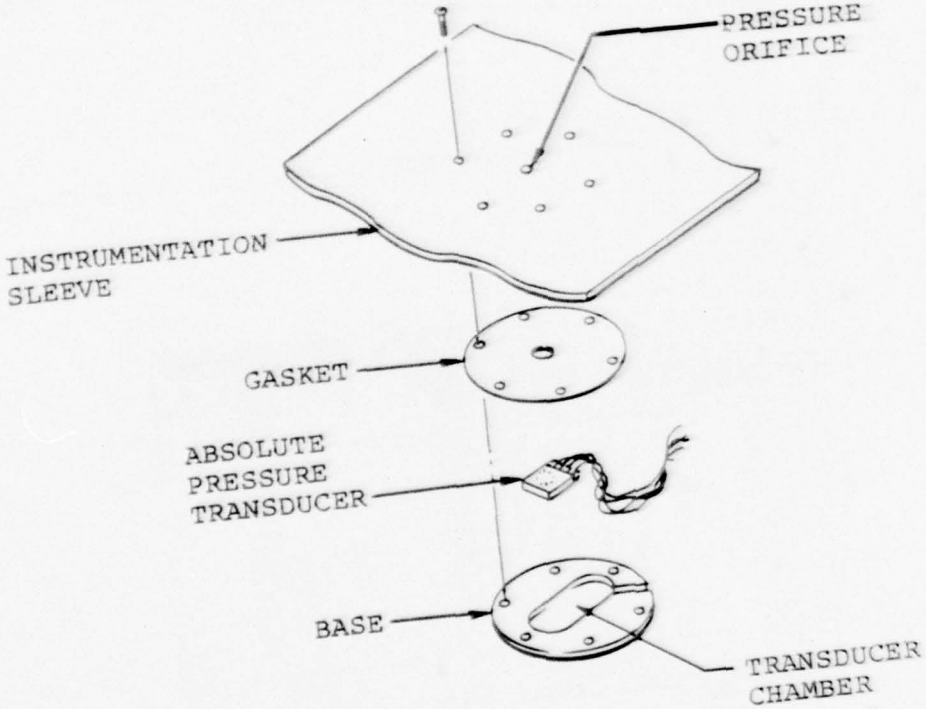

Figure 3. Component parts of absolute pressure transducer installation.

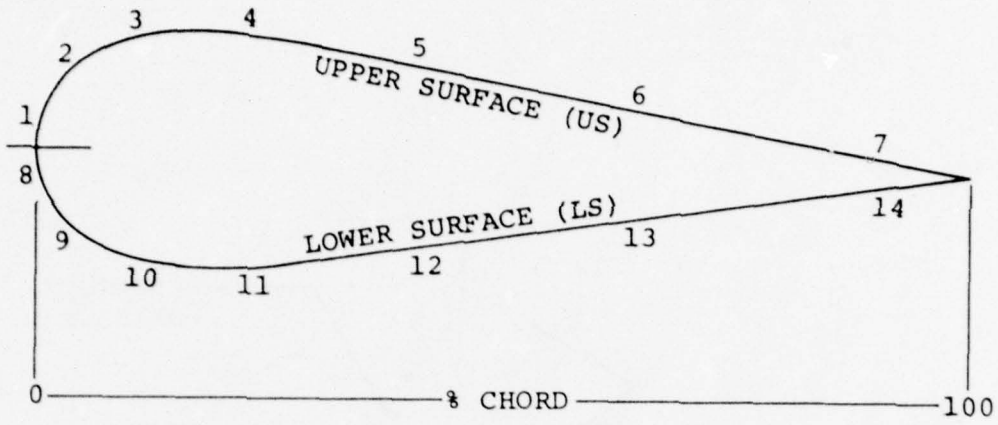

			MAXIMUM ANTICIPATED PRESSURE IN PSI *	
% CHORD	US	LS	US	LS
1	1	8	20	15
3	2	9	20	15
8	3	10	20	15
25	4	11	10	10
45	5	12	5	5
70	6	13	5	5
92	7	14	5	5

* ±Deviation from atmospheric pressure

Figure 4-a. Main rotor blade absolute pressure transducer locations, pressure ranges, and identification, r/R =0.40.

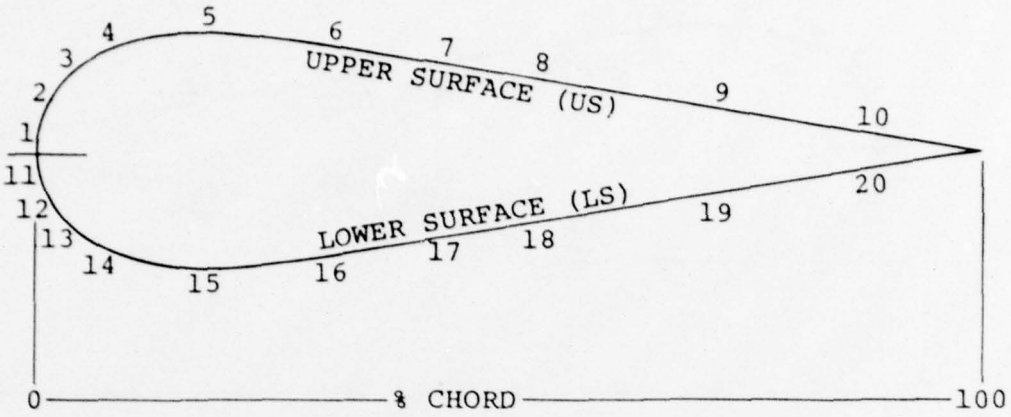

% CHORD	US	LS	MAXIMUM ANTICIPATED PRESSURE IN PSI * US	LS
1	1	11	20	15
3	2	12	20	15
8	3	13	20	10
15	4	14	20	10
25	5	15	10	5
35	6	16	10	5
45	7	17	10	5
55	8	18	5	5
70	9	19	5	5
92	10	20	5	5

* ±Deviation from atmospheric pressure

Figure 4-b. Main rotor blade absolute pressure transducer locations, pressure ranges, and identification, r/R = 0.060.

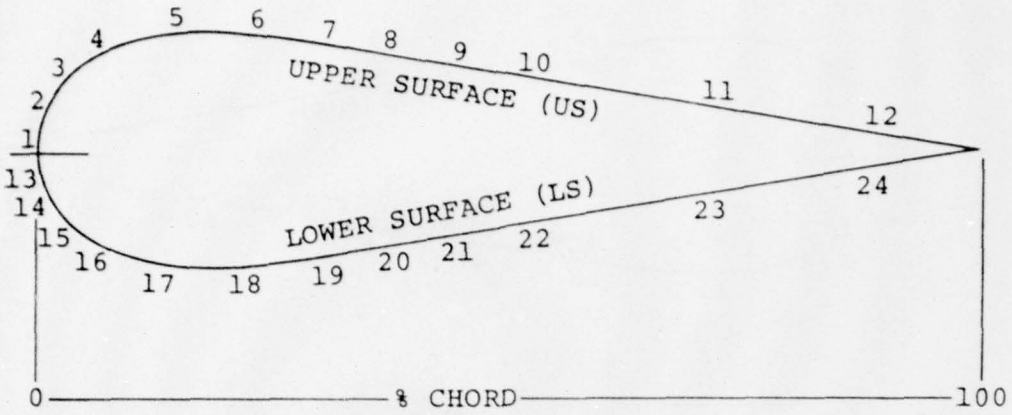

			MAXIMUM ANTICIPATED PRESSURE IN PSI *	
% CHORD	US	LS	US	LS
1	1	13	20	15
3	2	14	20	15
8	3	15	20	10
15	4	16	20	10
20	5	17	20	10
25	6	18	15	5
35	7	19	15	5
40	8	20	15	5
45	9	21	10	5
55	10	22	10	5
70	11	23	5	5
92	12	24	5	5

* ±Deviation from atmospheric pressure

Figure 4-c. Main rotor blade absolute pressure transducer locations, pressure ranges, and identification, r/R = 0.75.

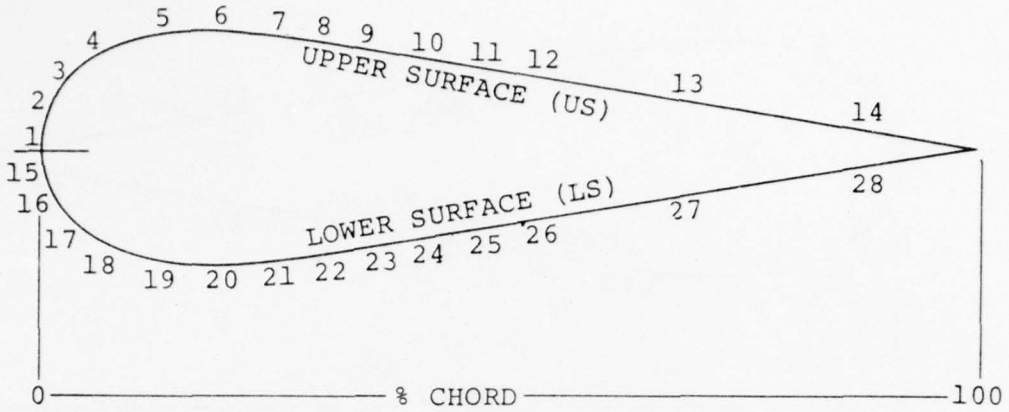

			MAXIMUM ANTICIPATED PRESSURE IN PSI *	
% CHORD	US	LS	US	LS
1	1	15	20	15
3	2	16	20	15
8	3	17	20	10
15	4	18	20	10
20	5	19	20	10
25	6	20	15	5
35	7	21	15	5
40	8	22	15	5
45	9	23	15	5
50	10	24	15	5
55	11	25	15	5
60	12	26	10	5
70	13	27	10	5
92	14	28	5	5

* ±Deviation from atmospheric pressure

Figure 4-d. Main rotor blade absolute pressure transducer locations, pressure ranges, and identification, r/R = 0.864.

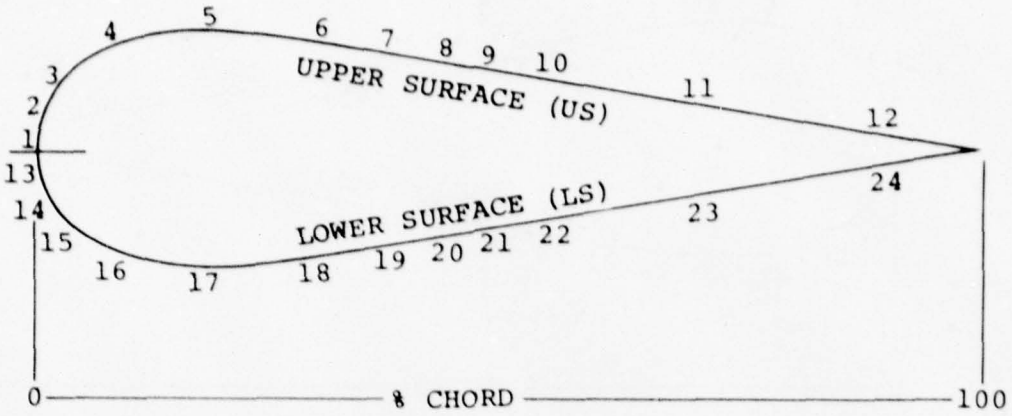

% CHORD	US	LS	MAXIMUM ANTICIPATED PRESSURE IN PSI * US	LS
1	1	13	20	15
3	2	14	20	15
8	3	15	20	10
15	4	16	20	10
25	5	17	15	5
35	6	18	15	5
40	7	19	15	5
45	8	20	15	5
50	9	21	15	5
55	10	22	10	5
70	11	23	10	5
92	12	24	5	5

* ±Deviation from atmospheric pressure

Figure 4-e. Main rotor blade absolute pressure transducer locations, pressure ranges, and identification, r/R = 0.955.

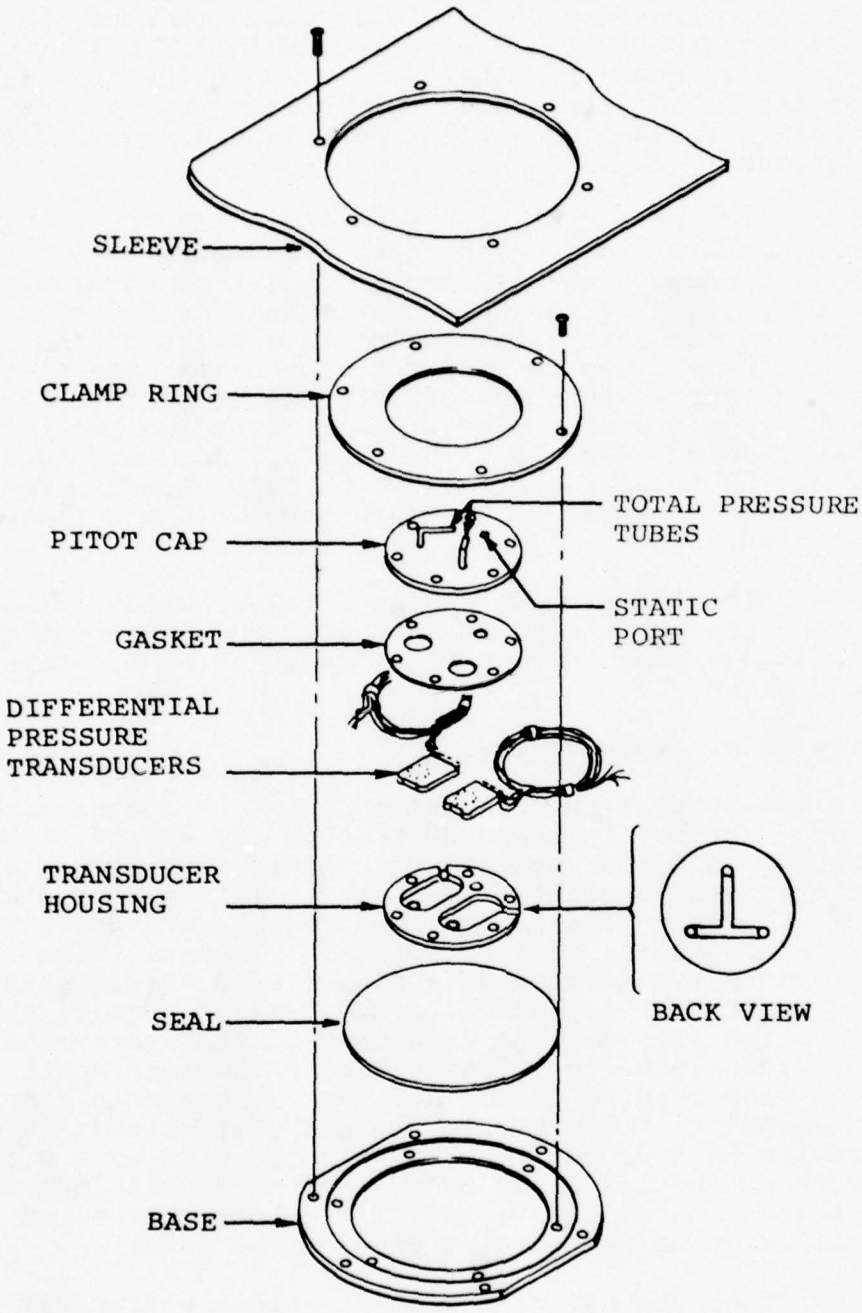

Figure 5. Component parts of BLB velocity gage installation using two differential pressure transducers.

Hence, the output of each transducer is dynamic pressure. Using the dynamic pressure, the velocity magnitude can be calculated. Each sensor is calibrated for an included flow-direction angle of 32 degrees. Analyses indicate that the flow direction excursion will exceed the linear range of the BLB over certain azimuth ranges for some flight speeds and spanwise locations.

The sensor's two differential pressure transducers are installed in a stainless-steel housing consisting of a base plate, a main body, a gasket, and a total-tube cover plate. The main body contains the pressure transducer cavities milled on the top and the static interconnecting ports milled on the bottom. The base plate is bonded to the lower side of the main body and serves to close off the static ports. The total tube pitot cap contains a single static port and two total tubes silver-soldered to it. The tube orifices are located at the apex of the triangle formed by the total tubes. The total tube pitot cap is bolted to the main body with six flat-head machine screws.

Six BLBs are located at each of the five selected radial stations. They are positioned at 30-, 60- and 90-percent chord locations as sketched in Figure 6. Anticipated pressure ranges are shown.

STAGNATION POINT INSTRUMENTATION

Chordwise movement of the stagnation point along the airfoil's leading edge surface is measured through the use of 80 hot-wire sensors. A higher density of hot wires is placed at the outboard stations to achieve greater resolution at low angles of attack. The hot-wire sensor is a temperature-differentiating device consisting of from 10 to 19 elements. The individual elements are mounted on a flexible, 0.004-inch-thick printed circuit that is bonded to the leading edge of the instrumentation sleeve. The printed circuit layout is a series of 0.020-inch-wide lines spaced 0.110 inch apart with the 0.020 lines running chordwise. Hot-wire elements are soldered normal to the 0.020 lines in a stair-step fashion at the chordwise contour positions. Each hot wire is a 0.110-inch length of special alloy Balco wire of 0.0012-inch diameter. Figure 7 shows the layout of the hot-wire sensor and its installation on the leading edge of the rotor.

At each station, the hot-wire elements are electrically connected in series, so that the circuit is energized by a single constant voltage source. Voltage drops across individual hot-wire elements provide the output signal. In operation, the wire closest to or at stagnation heats rapidly, producing a large voltage increase, while other wire voltages are decreased by cooling flow, thus accentuating the stagnation wire signal.

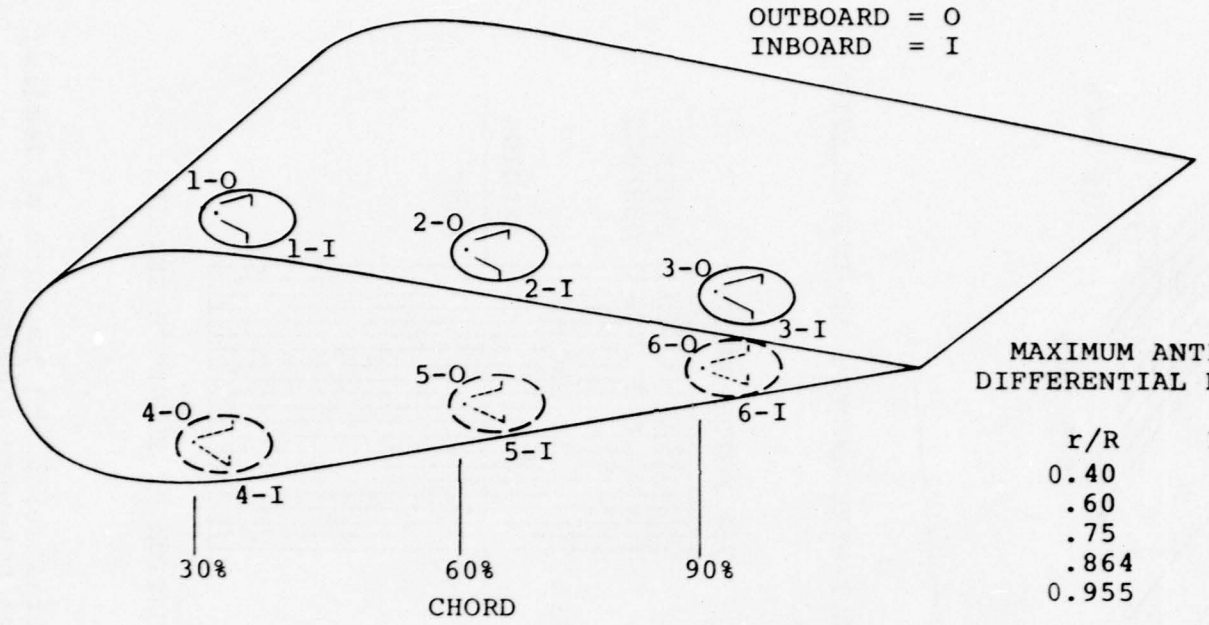

MAXIMUM ANTICIPATED DIFFERENTIAL PRESSURES:

r/R	PSI
0.40	3
.60	5
.75	6
.864	7
0.955	8

Figure 6. Main rotor blade BLB velocity gage locations, pressure ranges, and identification.

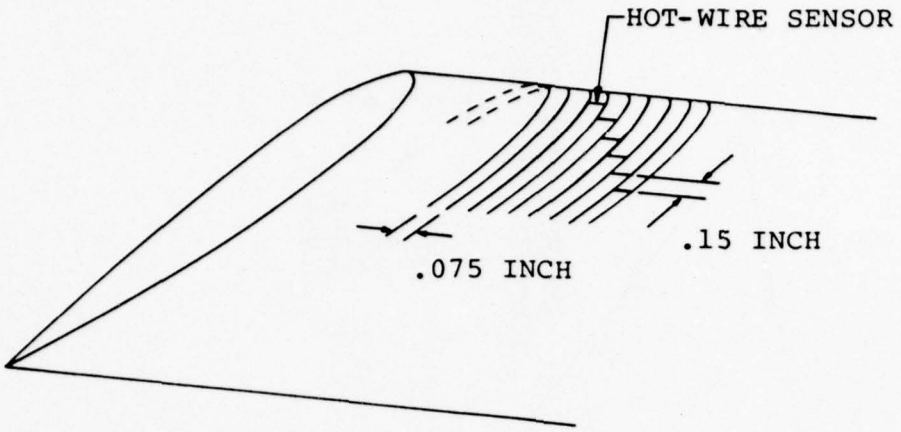

SKETCH OF HOT-WIRE ANEMOMETER INSTALLATION

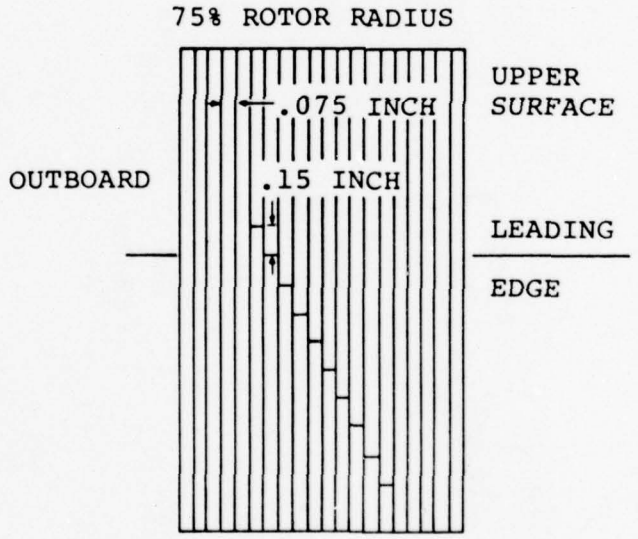

LOCATION OF HOT-WIRE SENSORS

Figure 7. Installation and location of leading edge hot-wire anemometer.

LOW-SPEED STEADY-STATE FLIGHTS

Data were reduced and analyzed for the low-speed steady-state flight conditions shown in Table 2. These flights, which were conducted at gross weights of 8100 and 9000 pounds, cover the speed range of 0 to 50 knots. In investigating the rotor's aerodynamic behavior in this flight region, primary emphasis was placed on analyzing the normal force coefficient (C_N) distributions using contour and surface plots obtained from the newly developed "Data Management System." Detailed comparisons between the measured C_N distributions and those calculated using three different performance methods were then made for the instrumented radial stations. For hover, measured values of C_N were compared to those obtained from Bell Helicopter Textron's (BHT) Prescribed Wake Lifting Surface Method (AR79DK). In forward flight the comparisons were made with BHT's blade/element momentum analysis (ARAM42) and BHT's distorted wake analysis (ARAP2MWK). To support these analyses, data concerning the rotor mast torque, fuselage attitudes, control positions, and hub flapping are included in Tables 3 and 4 for the two gross weight conditions of 8100 and 9000 pounds. A cursory examination was also made of the flow direction and magnitude for the 50-knot, 9000-pound flight condition (record 690) using the boundary layer button data. In addition, for hover, a comparison was made between the blade's angle of attack as determined from hot-wire stagnation point data and that calculated using BHT's prescribed Wake Lifting Surface Method.

CONTOUR AND SURFACE PLOTS FOR THE STEADY-STATE FLIGHTS

Contour and surface plots of the normal force coefficient for the steady-state flight conditions of Table 2 were derived from four radial stations (r/R = 0.40, 0.75, 0.864, 0.955) of absolute pressure data that is averaged for three continuous cycles. The fifth station (r/R = 0.60) was deleted since its integrated pressure data is in error due to an inoperative upper-surface leading-edge pressure transducer. The inside and outside limit of each plot is bounded by radial station r/R = 0.4 and r/R = 0.955, respectively, with data from stations r/R = 0.75 and r/R = 0.864 lying in between. Spanwise interpolation at each azimuth is through a cubic polynomial. Each contour interval on the plots depicts a 0.1 change in the normal force coefficient. Two surface plots are presented for each flight record to supplement the contour plot. A side and front perspective, with respect to the fuselage, were found to best illustrate the three-dimensional C_N distribution.

TABLE 2. FLIGHT CONDITIONS AND RECORD NUMBERS FOR THE NOE STEADY-STATE FLIGHTS

Flight Conditions	Altitude (feet)	GW = 8100 lb CG (Mid) Flt/Record	GW = 9000 lb CG (Mid) Flt/Record
OGE Hover	50	———	37B 685
IGE Hover	-	37D 722	———
OGE Hover	100	723	———
Forward Flight at 10 KIAS	50	724	37B 686
Forward Flight at 20 KIAS	50	725	687
Forward Flight at 30 KIAS	50	726	688
Forward Flight at 40 KIAS	50	727	689
Forward Flight at 50 KIAS	50	728	690
360-Degree Turn Record at 0 Degrees	50	736	———
Right Sideward Flt at 30 KIAS	50	717	———
Left Sideward Flt at 30 KIAS	50	720	———

TABLE 3. SUMMARY OF MAIN ROTOR TORQUE, FUSELAGE ATTITUDE, CONTROL POSITIONS, AND HUB FLAPPING, 8100 POUNDS GROSS WEIGHT

Record	Flight Description	M/R Torque in-lb	Fuselage Attitude			Control Positons			Hub Flapping		
			Pitch deg	Roll deg	Yaw deg	θ_0 %	A_{1C} %	B_{1C} %	a_0 deg	a_1 deg	b_1 deg
722	IGE Hover	147,000	-5.0	-0.8	3.2	34.0	49.4	36.8	-1.6	1.9	-1.3
723	OGE Hover @ 100 Feet	163,000	-3.3	-3.4	3.7	36.2	46.5	36.0	-1.6	1.9	-2.2
724	Forward Flight @ 10 KIAS	137,000	-6.0	-1.7	4.0	29.8	48.8	40.0	-1.5	0.4	0.2
725	Forward Flight @ 20 KIAS	118,000	-3.5	-2.4	3.0	26.7	49.5	45.6	-1.4	0.5	0.4
726	Forward Flight @ 30 KIAS	107,000	-2.0	-1.4	3.7	24.6	51.0	48.4	-1.4	0.9	0.5
727	Forward Flight @ 40 KIAS	93,000	-1.8	-1.2	5.5	22.7	51.5	49.0	-1.7	1.1	0.3
728	Forward Flight @ 50 KIAS	107,000	-5.5	0.5	3.7	24.7	53.7	50.0	-1.4	0.5	-0.1
736	360 Degree Turn-Record at 0 Deg	164,000	-2.0	-0.8	4.5	36.4	51.2	36.2	-1.7	2.3	-1.8
717	Right Sideward Flight @ 30 KIAS	124,000	-4.0	3.5	2.0	30.2	50.9	38.0	-1.6	4.9	-2.2
720	Left Sideward Flight @ 30 KIAS	131,000	-2.0	-6.9	4.0	31.7	48.1	36.4	-1.6	-1.0	-1.3

TABLE 4. SUMMARY OF MAIN ROTOR TORQUE, FUSELAGE ATTITUDE, CONTROL POSITIONS, AND HUB FLAPPING, 9000 POUNDS GROSS WEIGHT

Record	Flight Description	M/R Torque in-lb	Fuselage Attitude			Control Positons			Hub Flapping		
			Pitch deg	Roll deg	Yaw deg	θ_0 %	A_{1C} %	B_{1C} %	a_0 deg	a_1 deg	b_1 deg
685	OGE Hover @ 50 Feet	190,000	-4.7	-1.1	4.5	39.6	47.5	36.2	-1.5	1.6	-1.5
686	Forward Flight @ 10 KIAS	152,000	-4.3	-2.2	6.7	33.0	47.5	44.7	-1.5	0.2	0.1
687	Forward Flight @ 20 KIAS	137,000	-2.0	-0.7	3.5	29.0	49.0	45.7	-1.8	0.6	0.4
688	Forward Flight @ 30 KIAS	122,000	-0.8	-0.2	3.2	26.9	50.4	49.2	-1.5	0.3	0.4
689	Forward Flight @ 40 KIAS	105,000	-3.4	-2.4	2.0	22.7	52.6	49.6	-1.5	1.0	0.4
690	Forward Flight @ 50 KIAS	110,000	-4.6	-1.2	3.1	24.1	53.4	50.0	-1.5	0.3	0.2

Hover

Contour and surface plots of normal force coefficient, C_N, for four separate hover records are shown in Figures 8 through 11. Record 685 was recorded at a gross weight of 9000 pounds and 50-foot altitude, whereas record 722 was recorded at a gross weight of 8100 pounds and in ground effect (IGE). Records 723 and 736 are at the same condition of 8100 pounds gross weight at 100- and 50-foot altitudes, respectively. Both the 50- and 100-foot altitude cases are considered to be out of ground effect, which is taken to be beyond one rotor diameter from the ground. Examination of the hover records shows substantial deviations from the anticipated symmetrical C_N distribution. Only record 722 comes reasonably close to being symmetrical. Any perturbation that alters the inflow through the rotor disc affects the symmetry of the C_N distribution. Ambient winds and turbulence, along with recirculation from both main and tail rotor, are almost always present during hover and contribute to the asymmetry.

Control-tower-reported winds during these flight records were in the range of 5 to 8 knots. However, local wind conditions present when the data are recorded most likely differ from those reported. Significant wind effects appear to be present for OGE hover (Figure 8A). The C_N distribution is somewhat similar to that obtained for a 10-knot forward-flight condition (Figure 12). In Tables 3 and 4, it is seen that some left and aft cyclic control is usually present during hover to compensate for the tail rotor rolling moment and center of gravity pitching moment. However, these cyclic inputs only tilt the main rotor's thrust vector and should have no effect on the symmetry of the C_N distribution in the tip-path plane.

Forward Flight 10, 20, 30, 40, and 50 Knots

Upon analyzing the low-speed forward-flight C_N distributions of normal force coefficient (Figures 12 through 21), the following trends are seen to occur with increased airspeed. Going from hover to 10 knots, the quasi-symmetric C_N distribution is considerably altered. At 10 knots the magnitude of the C_N distribution increases across the back of the disc to compensate for the decreases over the front of the disc. The decrease in C_N at the front of the disc is due to the blade passing over the preceding blade's vortex, resulting in a sharp rise in the C_N distribution along the leading edge of the disc.

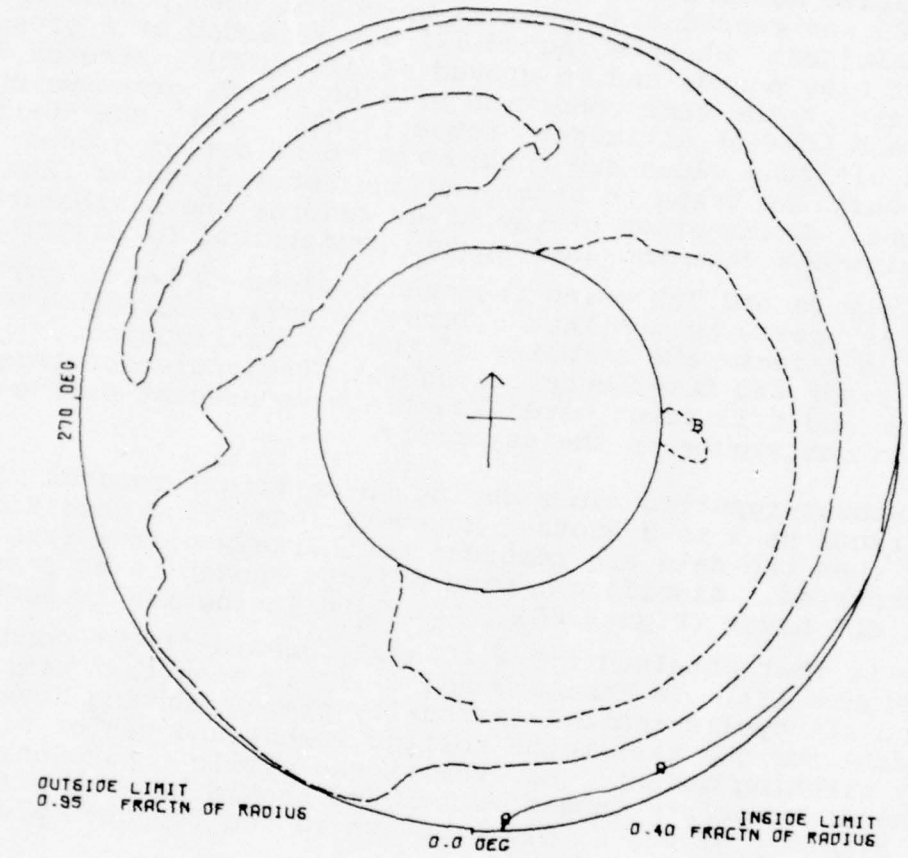

DERIVED PARAMETER - NORMAL FORCE COEFFICIENT

COUNTER 685

GROSS WT 9000. SHIP MODEL AH-1G
LONG CG 196.2 SHIP ID 20391

A ——— 0.3 CN
B - - - - - 0.6 CN

Figure 8A. C_N contour plot (OGE hover at 50 feet).

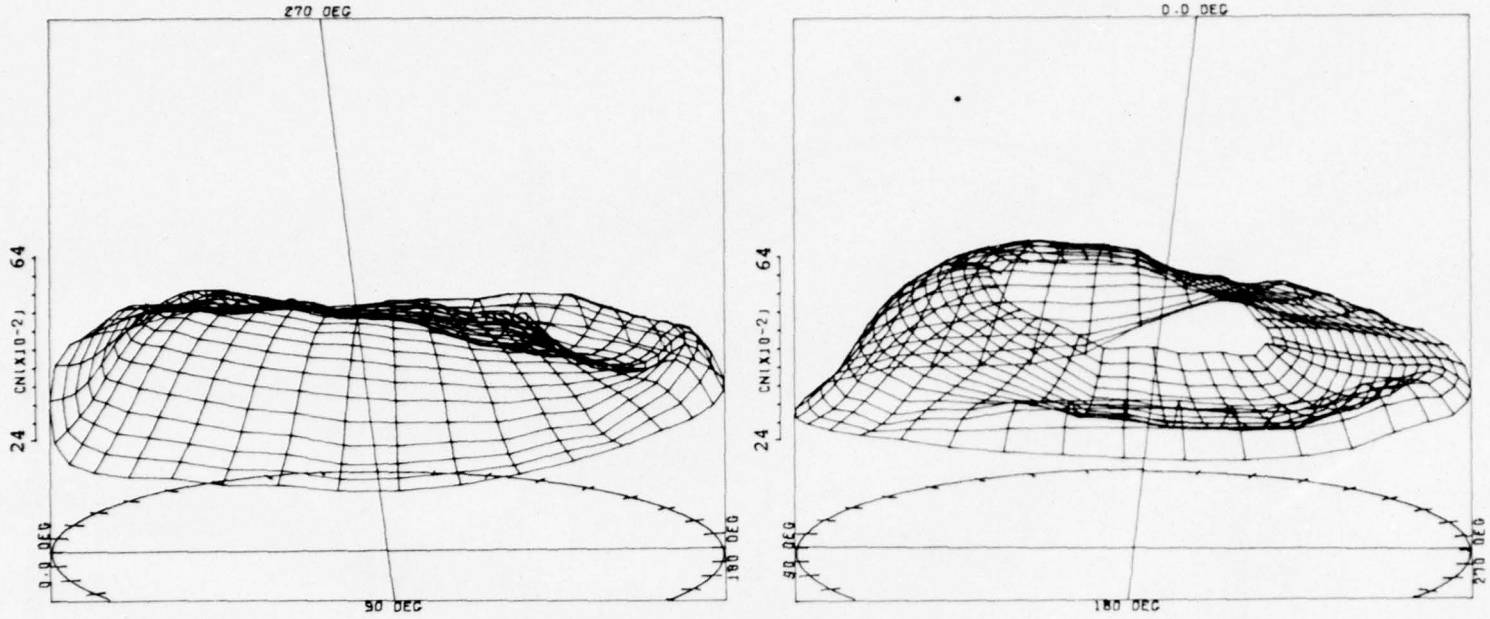

Figure 8B. C_N surface plots (OGE hover at 50 feet).

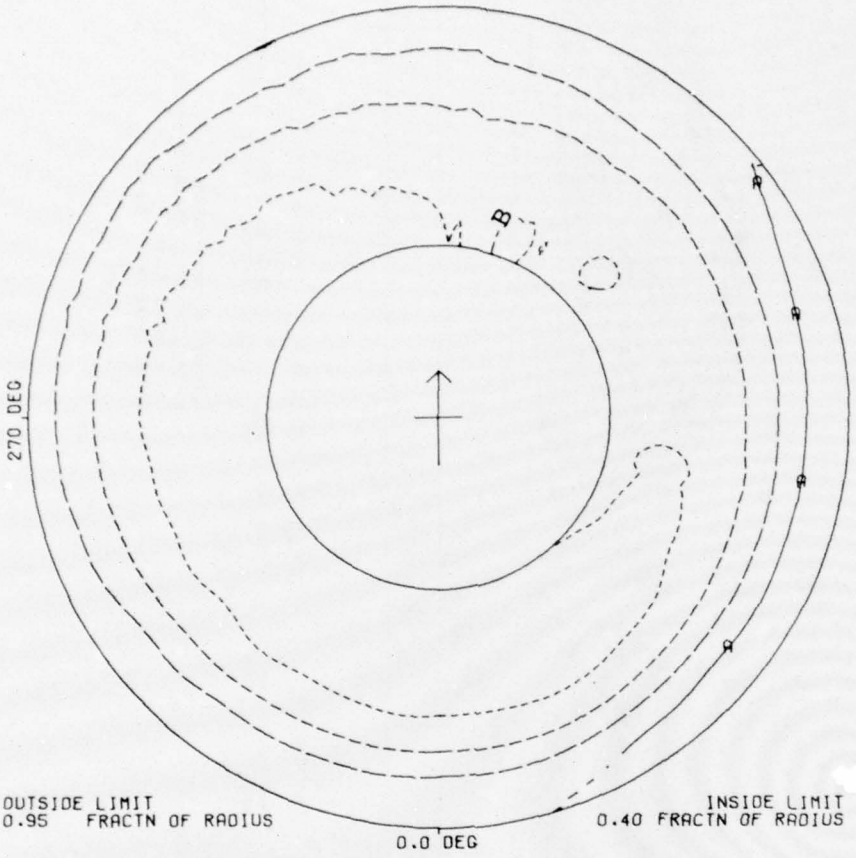

DERIVED PARAMETER - NORMAL FORCE COEFFICIENT

COUNTER	722	GROSS WT	8100	SHIP MODEL	AH-1G
		LONG CG	196.5	SHIP ID	20391

A ———— 0.3 CN
B - - - - - 0.6 CN

Figure 9A. C_N contour plot (IGE hover).

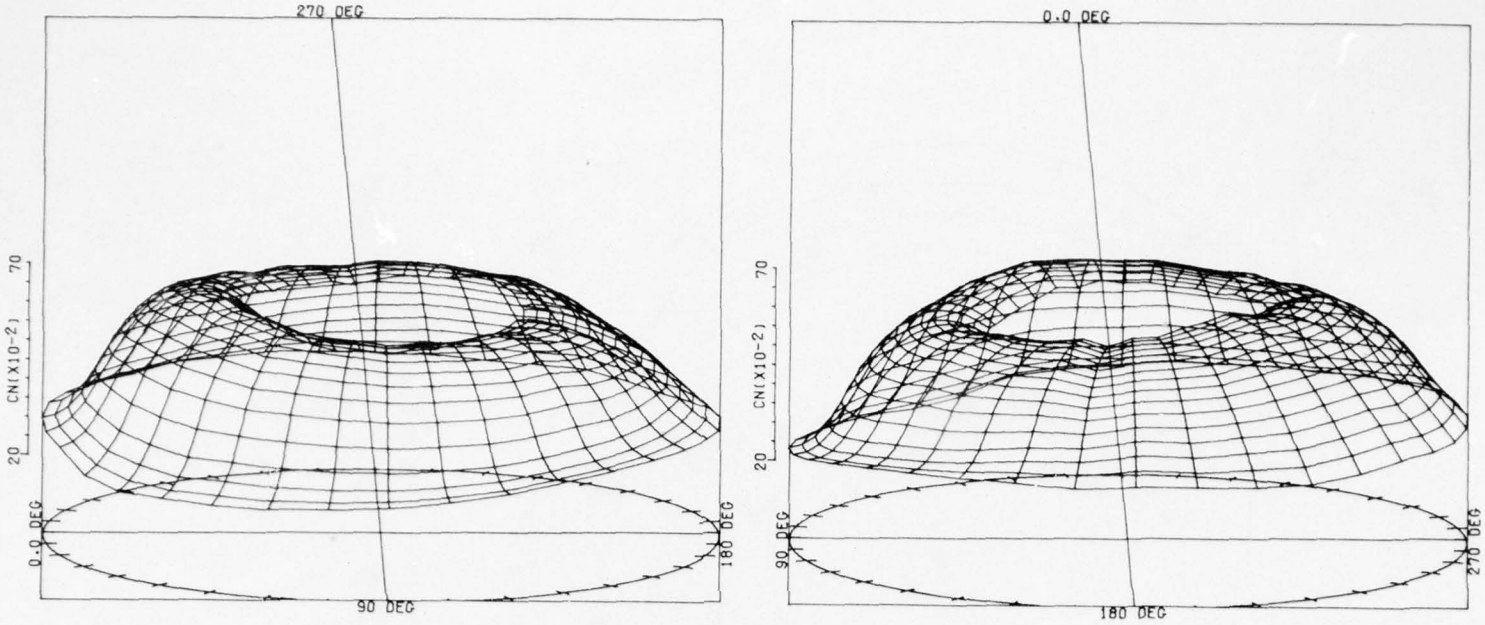

Figure 9B. C_N surface plots (IGE hover).

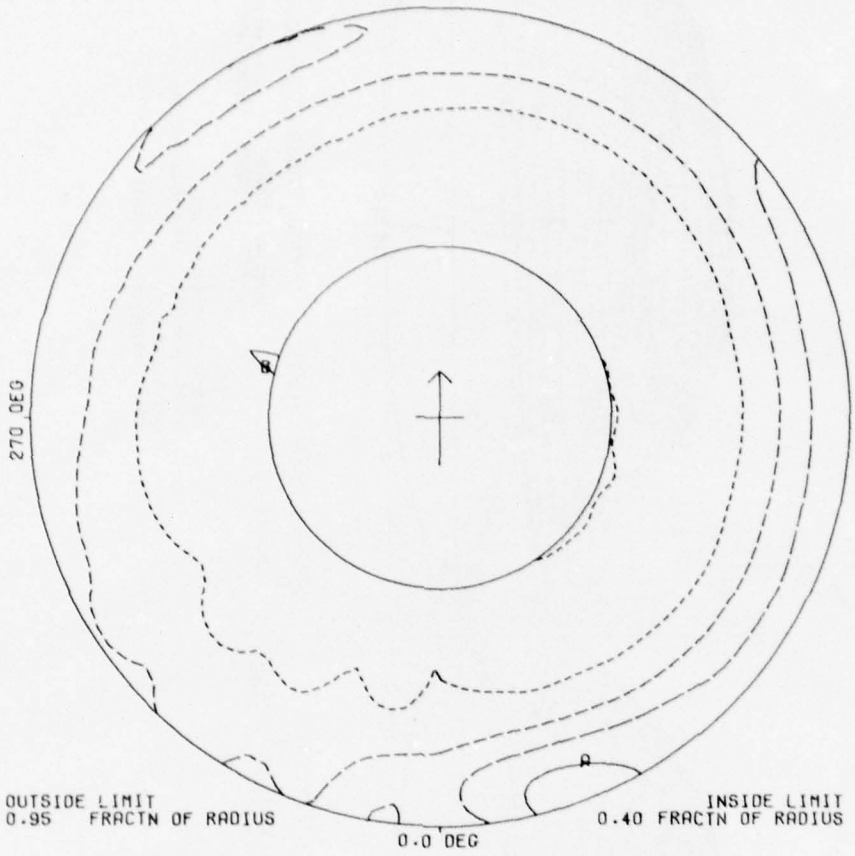

DERIVED PARAMETER - NORMAL FORCE COEFFICIENT

COUNTER	723	GROSS WT	8100.	SHIP MODEL	AH-1G
		LONG CG	196.5	SHIP ID	20391

A ——— 0.2 CN
B ——— 0.6 CN

Figure 10A. C_N contour plot (OGE hover at 100 feet).

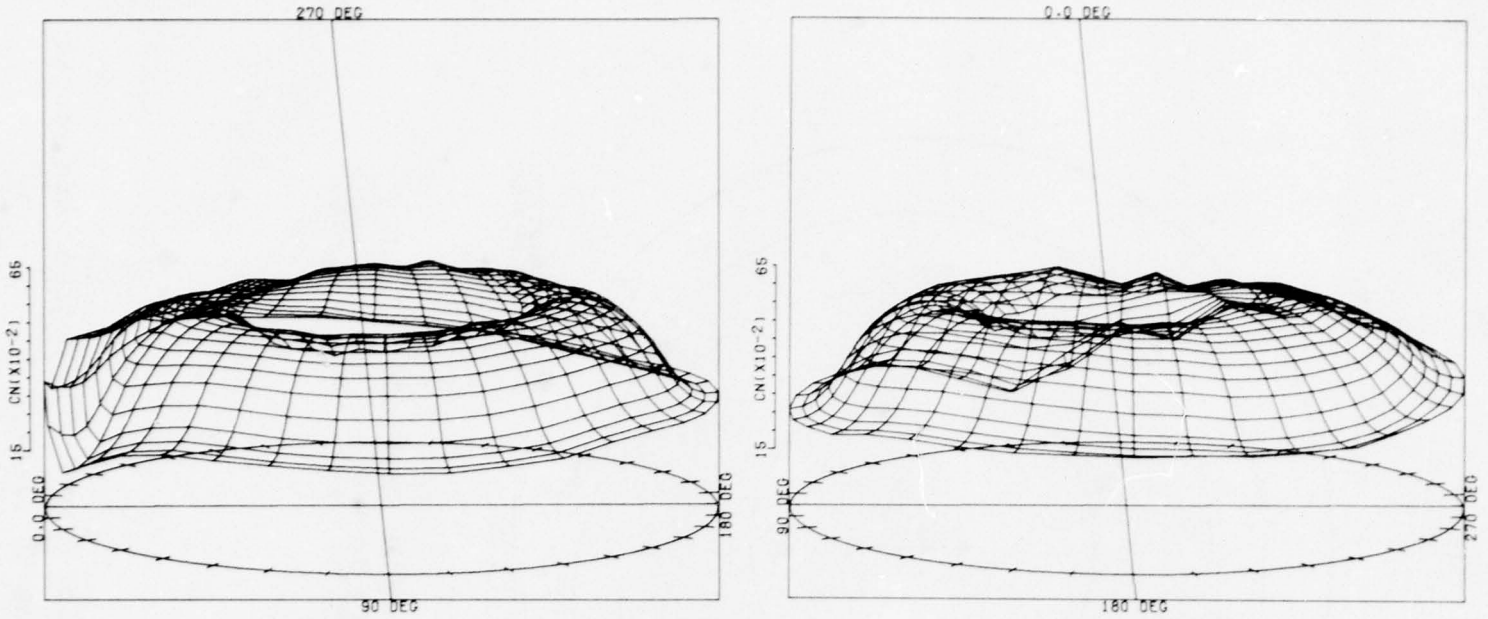

DERIVED PARAMETER - NORMAL FORCE COEFFICIENT

COUNTER 723 GROSS WT 8100 SHIP MODEL AH-1G
LONG CG 196.5 SHIP ID 20391

ANGULAR INCREMENT 10 DEG
RADIAL QUANTITY FRACTN OF RADIUS
MAX RADIUS 0.955
RADIAL INCREMENT 0.0370

DERIVED PARAMETER - NORMAL FORCE COEFFICIENT

COUNTER 723 GROSS WT 8100 SHIP MODEL AH-1G
LONG CG 196.5 SHIP ID 20391

ANGULAR INCREMENT 10 DEG
RADIAL QUANTITY FRACTN OF RADIUS
MAX RADIUS 0.955
RADIAL INCREMENT 0.0370

Figure 10B. C_N surface plots (OGE hover at 100 feet).

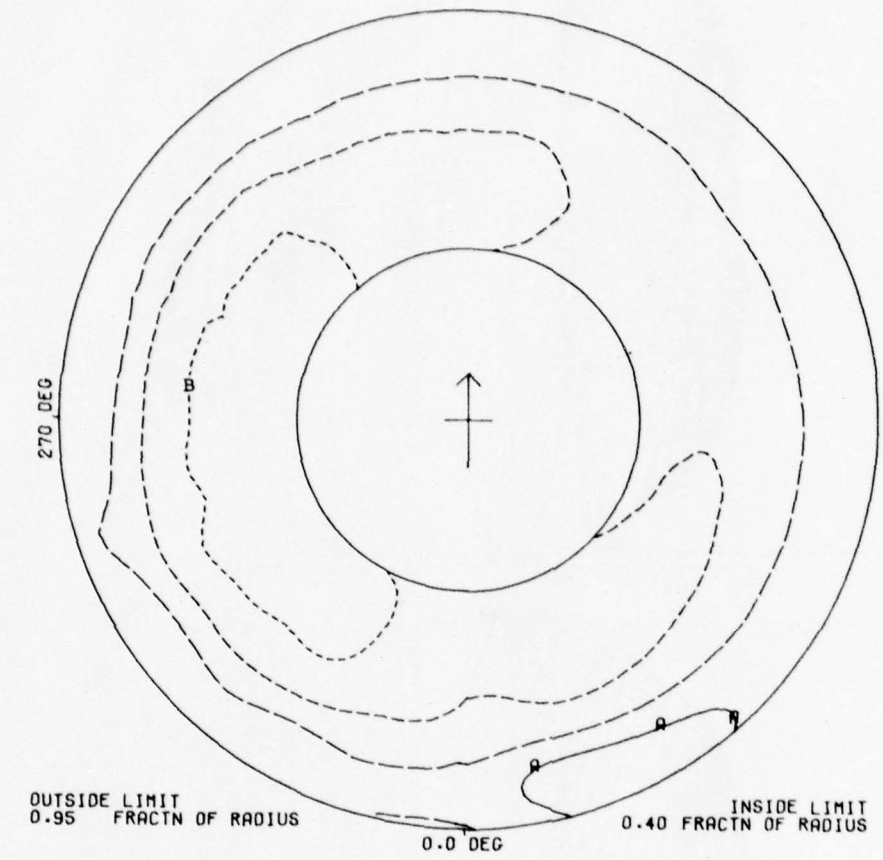

DERIVED PARAMETER - NORMAL FORCE COEFFICIENT

COUNTER 736

GROSS WT 8100 SHIP MODEL AH-1G
LONG CG 196.5 SHIP ID 20391

A ——— 0.3 CN
B - - - - - - - 0.6 CN

Figure 11A. C_N contour plot (hover 360-degree turn record at 0 degree at 50 feet).

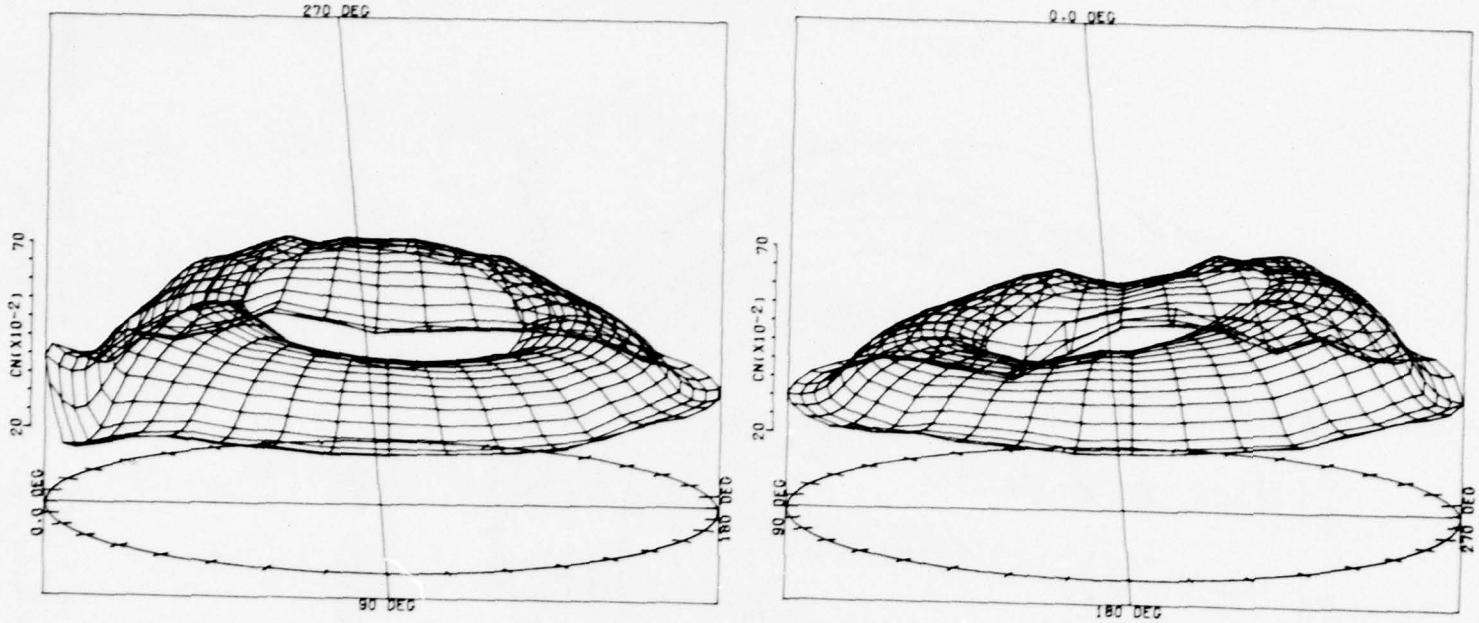

DERIVED PARAMETER - NORMAL FORCE COEFFICIENT

COUNTER 736 GROSS WT 8100 SHIP MODEL AH-1G
LONG CG 196.5 SHIP ID 20991

ANGULAR INCREMENT 10 DEG
RADIAL QUANTITY FRACTN OF RADIUS
MAX RADIUS 0.955
RADIAL INCREMENT 0.0370

DERIVED PARAMETER - NORMAL FORCE COEFFICIENT

COUNTER 736 GROSS WT 8100 SHIP MODEL AH-1G
LONG CG 196.5 SHIP ID 20991

ANGULAR INCREMENT 10 DEG
RADIAL QUANTITY FRACTN OF RADIUS
MAX RADIUS 0.955
RADIAL INCREMENT 0.0370

Figure 11B. C_N surface plots (hover 360-degree turn record at 0 degree at 50 feet).

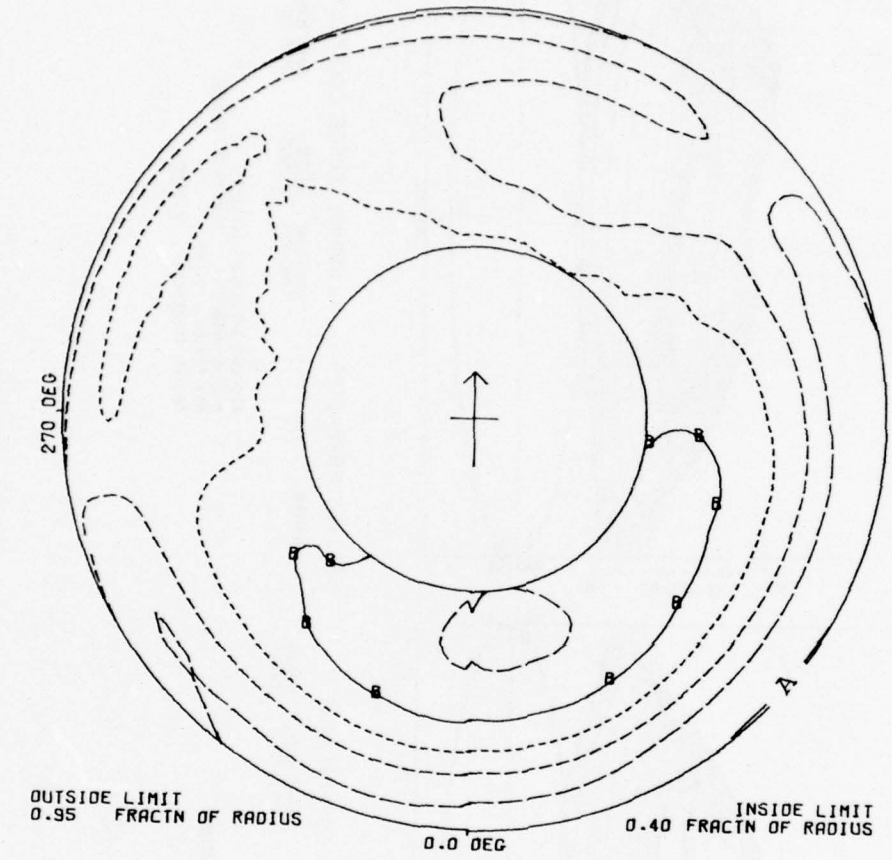

Figure 12A. C_N contour plot (level flight at 10 knots, gross weight 8100 pounds, altitude 50 feet).

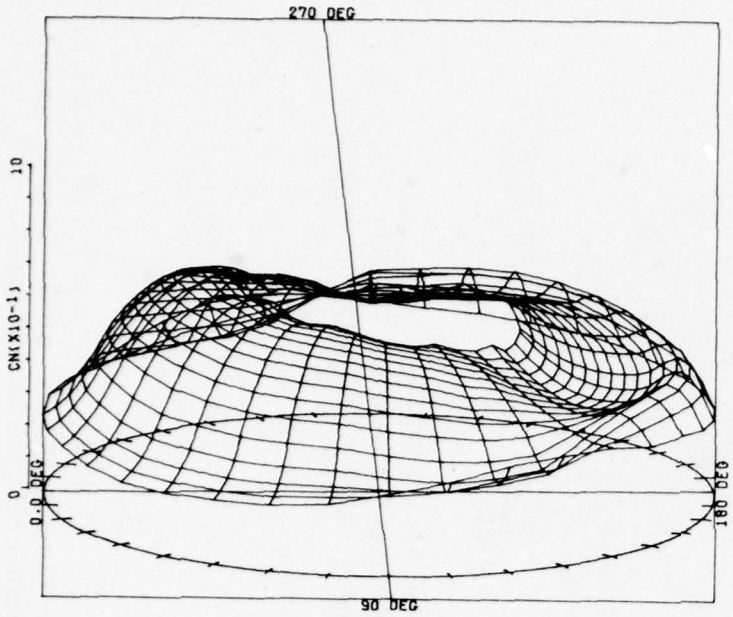

DERIVED PARAMETER - NORMAL FORCE COEFFICIENT

COUNTER 724 GROSS WT 8100 SHIP MODEL AH-1G
LONG CG 196.5 SHIP ID 20391

ANGULAR INCREMENT 10 DEG
RADIAL QUANTITY FRACTN OF RADIUS
MAX RADIUS 0.955
RADIAL INCREMENT 0.0370

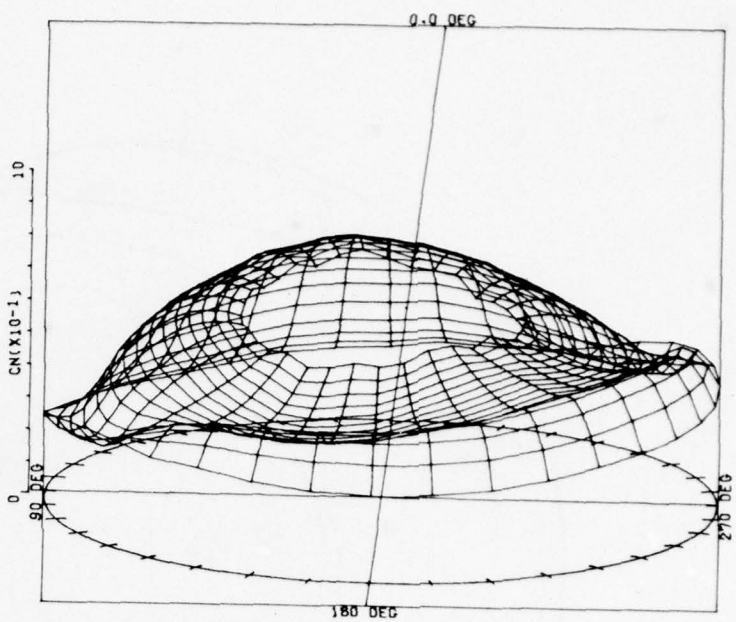

DERIVED PARAMETER - NORMAL FORCE COEFFICIENT

COUNTER 724 GROSS WT 8100 SHIP MODEL AH-1G
LONG CG 196.5 SHIP ID 20391

ANGULAR INCREMENT 10 DEG
RADIAL QUANTITY FRACTN OF RADIUS
MAX RADIUS 0.955
RADIAL INCREMENT 0.0370

Figure 12B. C_N surface plots (level flight at 10 knots, gross weight 8100 pounds, altitude 50 feet).

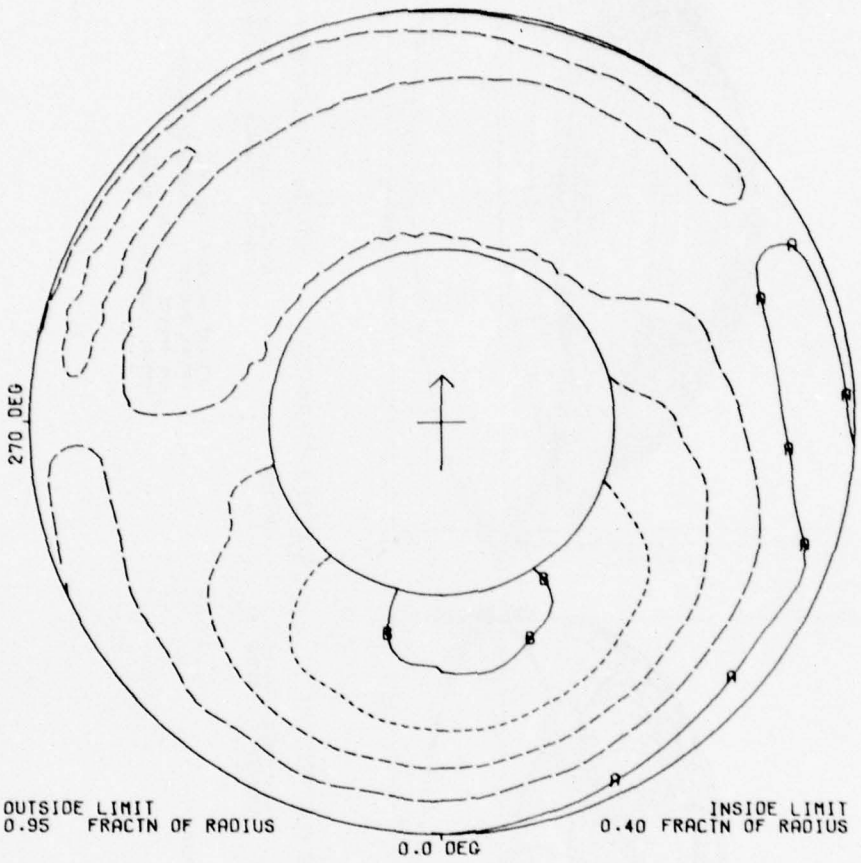

Figure 13a. C_N contour plot (level flight at 10 knots, gross weight 9000 pounds, altitude 50 feet).

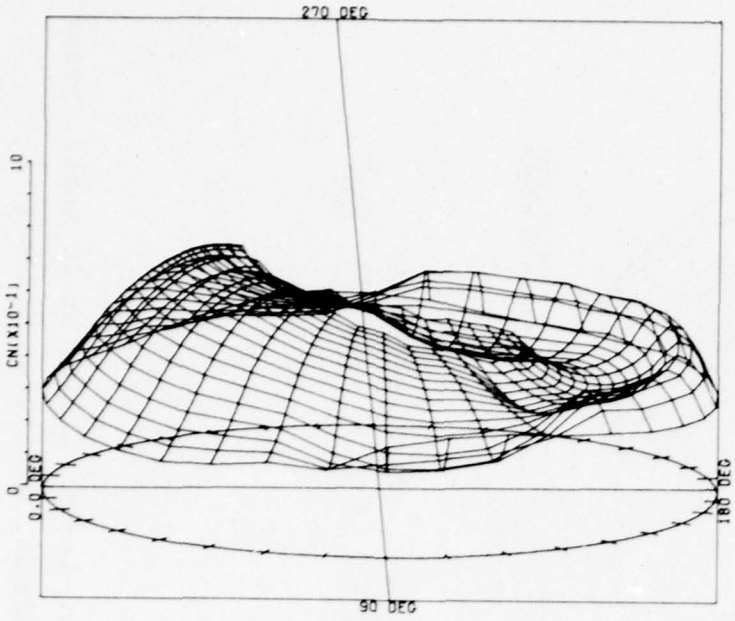

DERIVED PARAMETER - NORMAL FORCE COEFFICIENT

COUNTER 686 GROSS WT 9000. SHIP MODEL AH-1G
LONG CG 196.2 SHIP ID 20391

ANGULAR INCREMENT 10 DEG
RADIAL QUANTITY FRACTN OF RADIUS
MAX RADIUS 0.955
RADIAL INCREMENT 0.0370

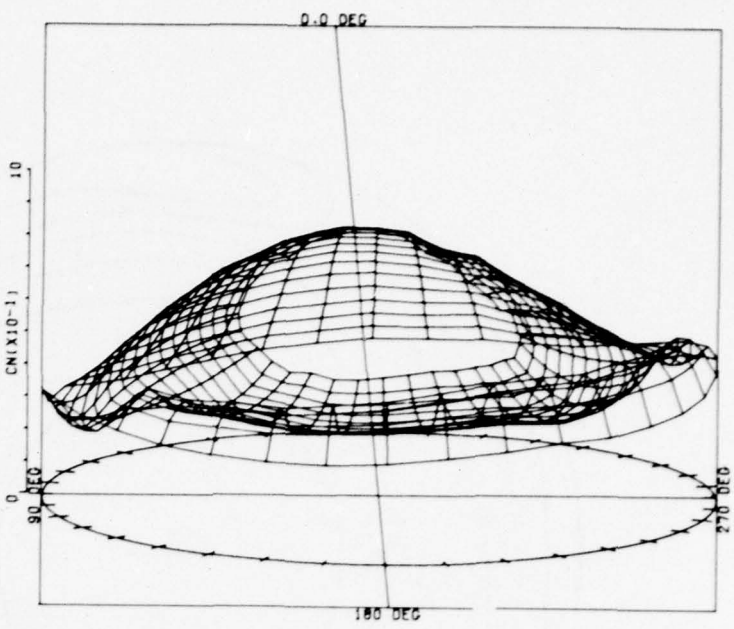

DERIVED PARAMETER - NORMAL FORCE COEFFICIENT

COUNTER 686 GROSS WT 9000. SHIP MODEL AH-1G
LONG CG 196.2 SHIP ID 20391

ANGULAR INCREMENT 10 DEG
RADIAL QUANTITY FRACTN OF RADIUS
MAX RADIUS 0.955
RADIAL INCREMENT 0.0370

Figure 13B. C_N surface plot (level flight at 10 knots, gross weight 9000 pounds, altitude 50 feet).

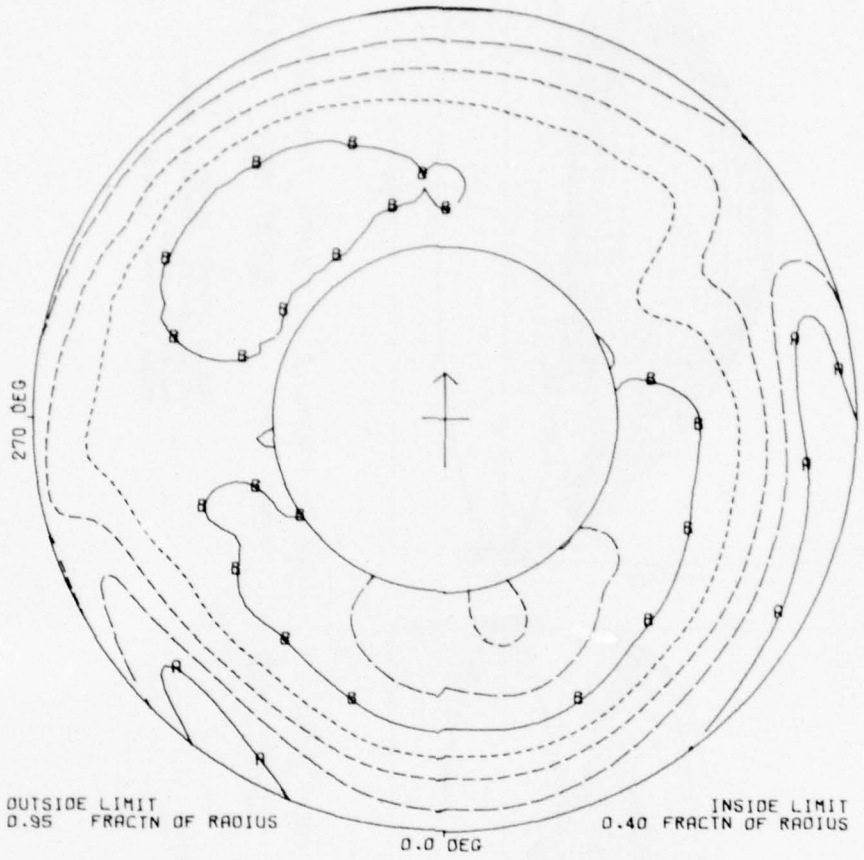

Figure 14A. C_N contour plot (level flight at 20 knots, gross weight 8100 pounds, altitude 50 feet).

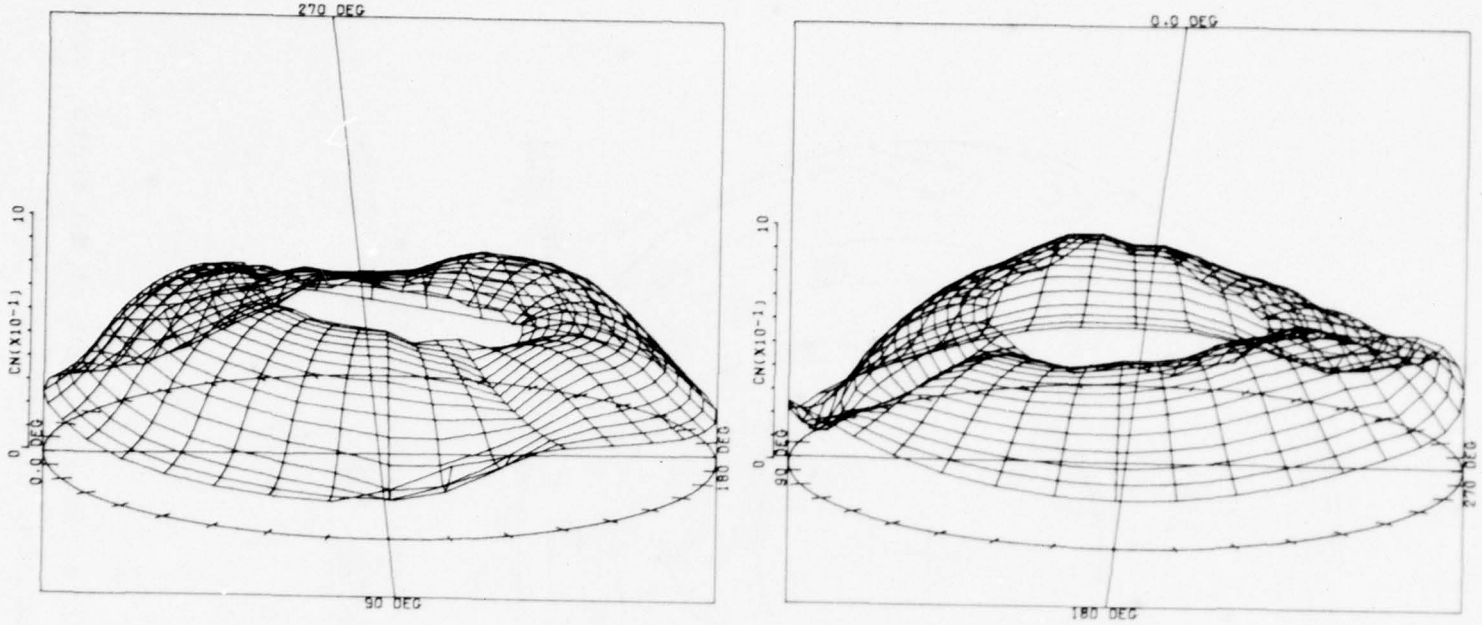

DERIVED PARAMETER - NORMAL FORCE COEFFICIENT

COUNTER 725 GROSS WT 8100 SHIP MODEL AH-1G
LONG CG 196.5 SHIP ID 20391

ANGULAR INCREMENT 10 DEG
RADIAL QUANTITY FRACTN OF RADIUS
MAX RADIUS 0.955
RADIAL INCREMENT 0.0370

DERIVED PARAMETER - NORMAL FORCE COEFFICIENT

COUNTER 725 GROSS WT 8100 SHIP MODEL AH-1G
LONG CG 196.5 SHIP ID 20391

ANGULAR INCREMENT 10 DEG
RADIAL QUANTITY FRACTN OF RADIUS
MAX RADIUS 0.955
RADIAL INCREMENT 0.0370

Figure 14B. C_N surface plots (level flight at 20 knots, gross weight 8100 pounds, altitude 50 feet).

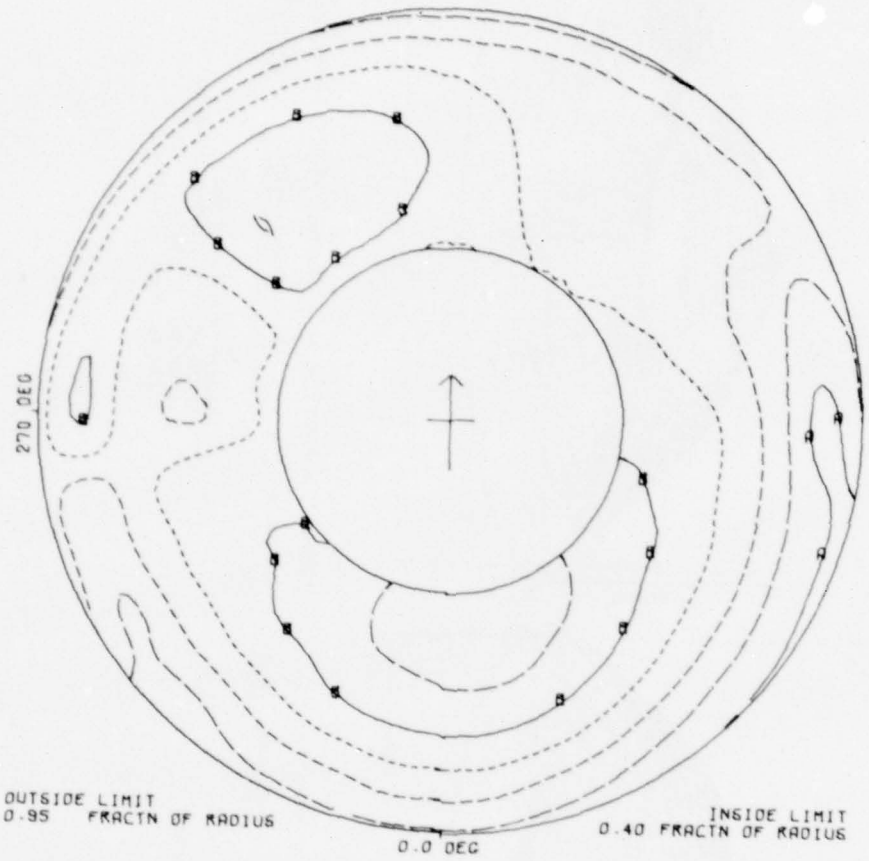

Figure 15A. C_N contour plots (level flight at 20 knots, gross weight 9000 pounds, altitude 50 feet).

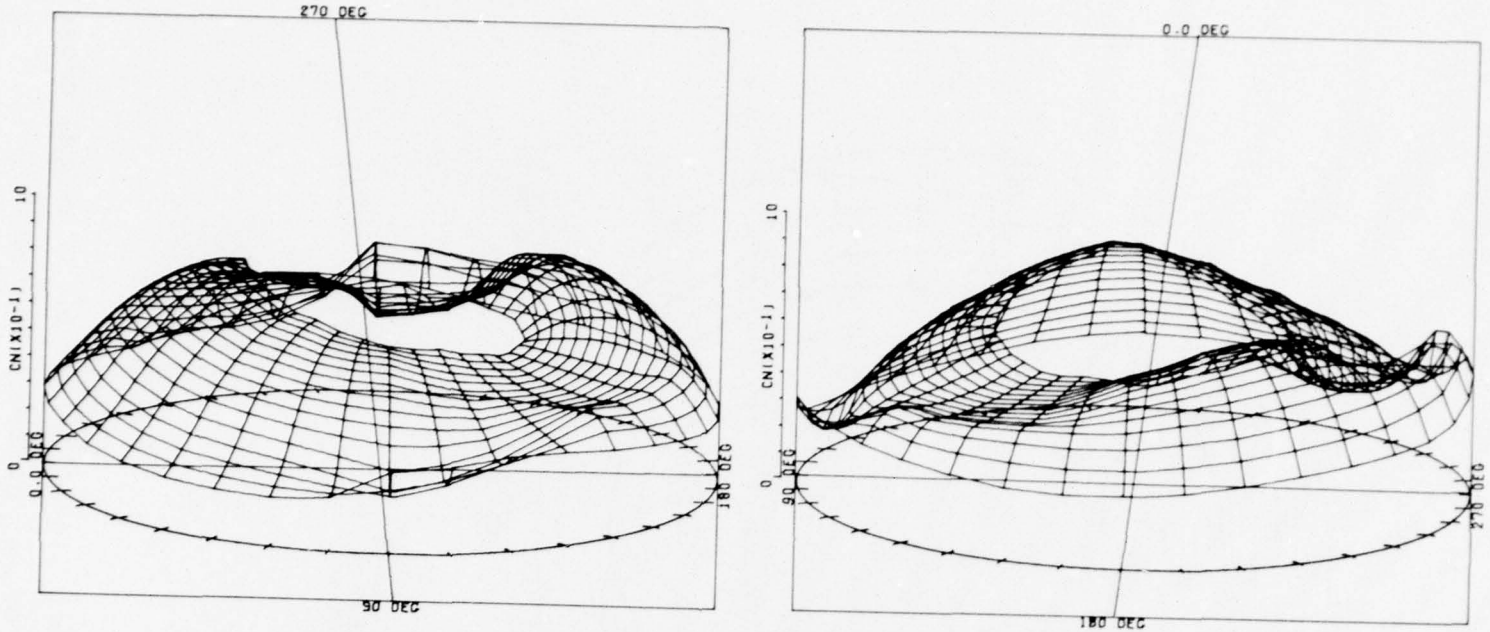

Figure 15B. C_N surface plots (level flight at 20 knots, gross weight 9000 pounds, altitude 50 feet).

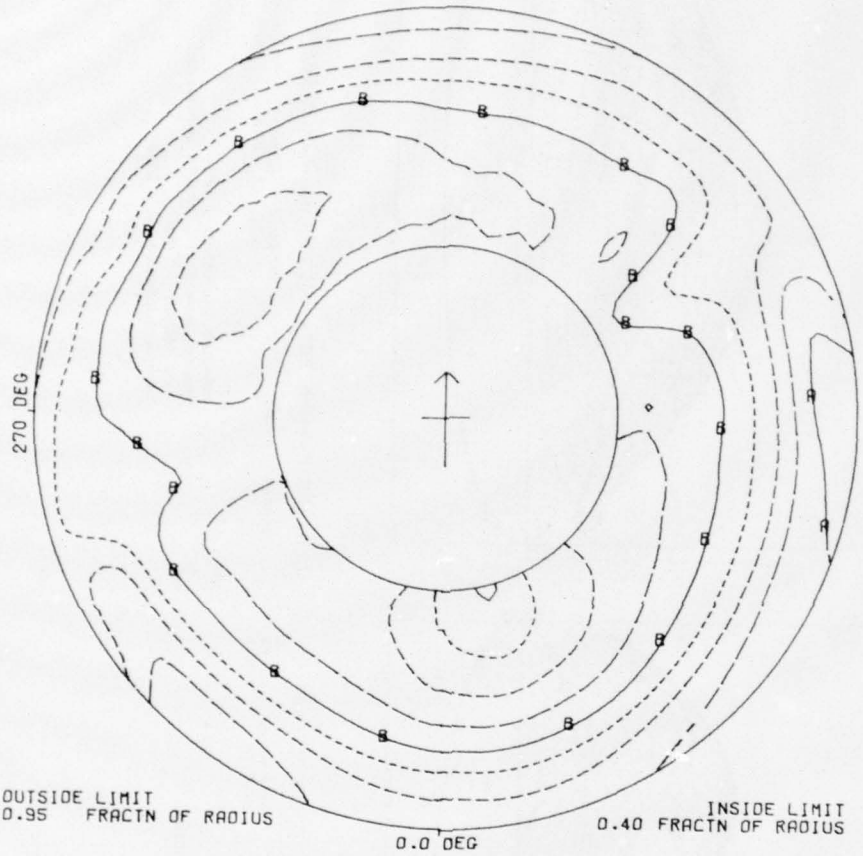

Figure 16A. C_N contour plot (level flight at 30 knots, gross weight 8100 pounds, altitude 50 feet).

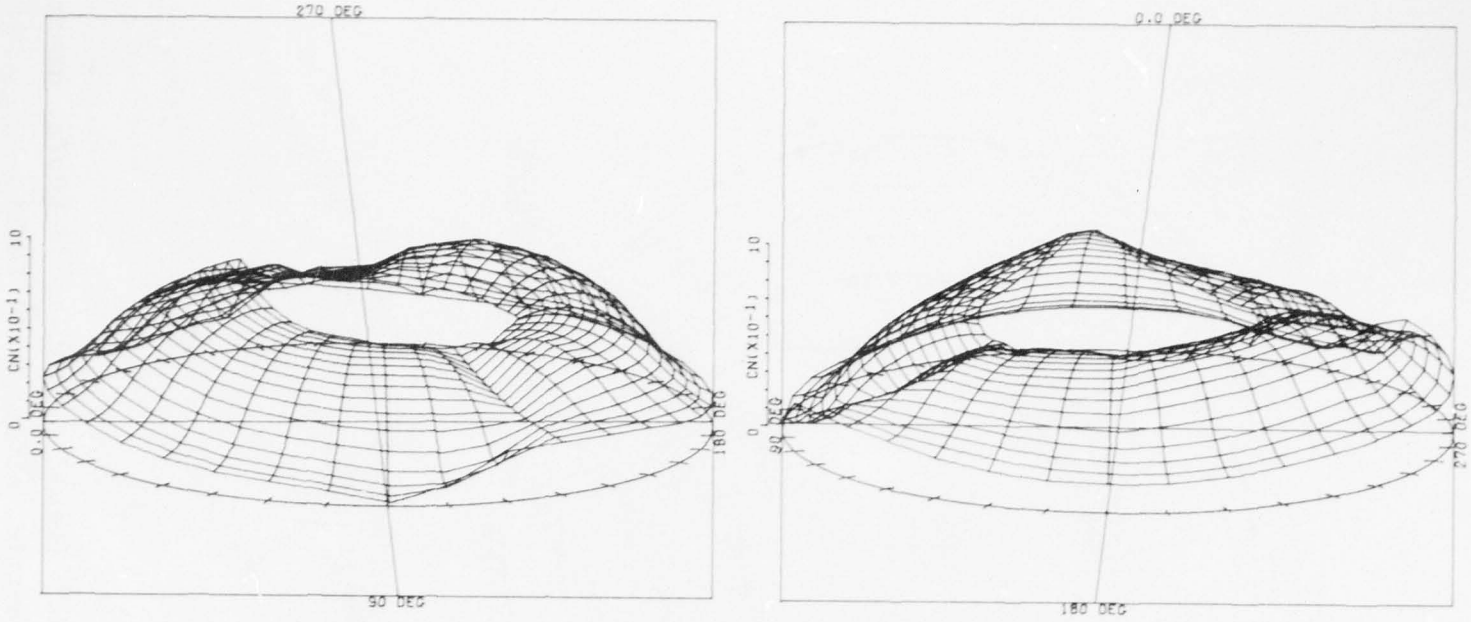

DERIVED PARAMETER - NORMAL FORCE COEFFICIENT

COUNTER 726 GROSS WT 8100 SHIP MODEL AH-1G
LONG CG 196.5 SHIP ID 20391

ANGULAR INCREMENT 10 DEG
RADIAL QUANTITY FRACTN OF RADIUS
MAX RADIUS 0.955
RADIAL INCREMENT 0.0370

DERIVED PARAMETER - NORMAL FORCE COEFFICIENT

COUNTER 726 GROSS WT 8100 SHIP MODEL AH-1G
LONG CG 196.5 SHIP ID 20391

ANGULAR INCREMENT 10 DEG
RADIAL QUANTITY FRACTN OF RADIUS
MAX RADIUS 0.955
RADIAL INCREMENT 0.0370

Figure 16B. C_N surface plots (level flight at 30 knots, gross weight 8100 pounds, altitude 50 feet).

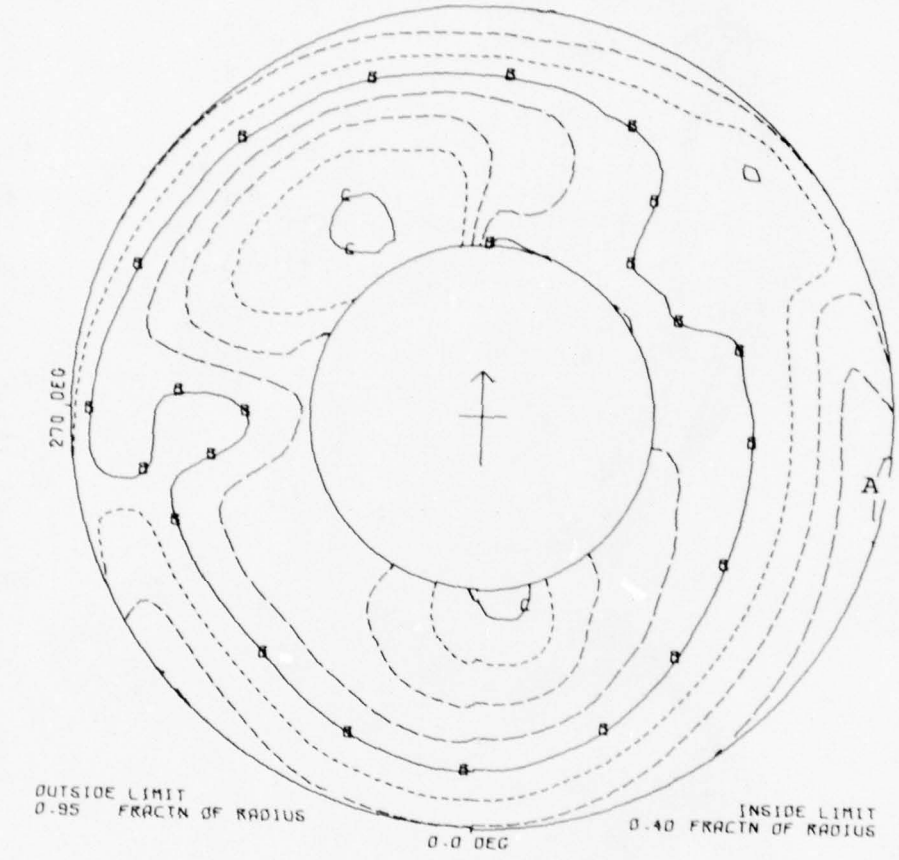

Figure 17A. C_N contour plot (level flight at 30 knots, gross weight 9000 pounds, altitude 50 feet).

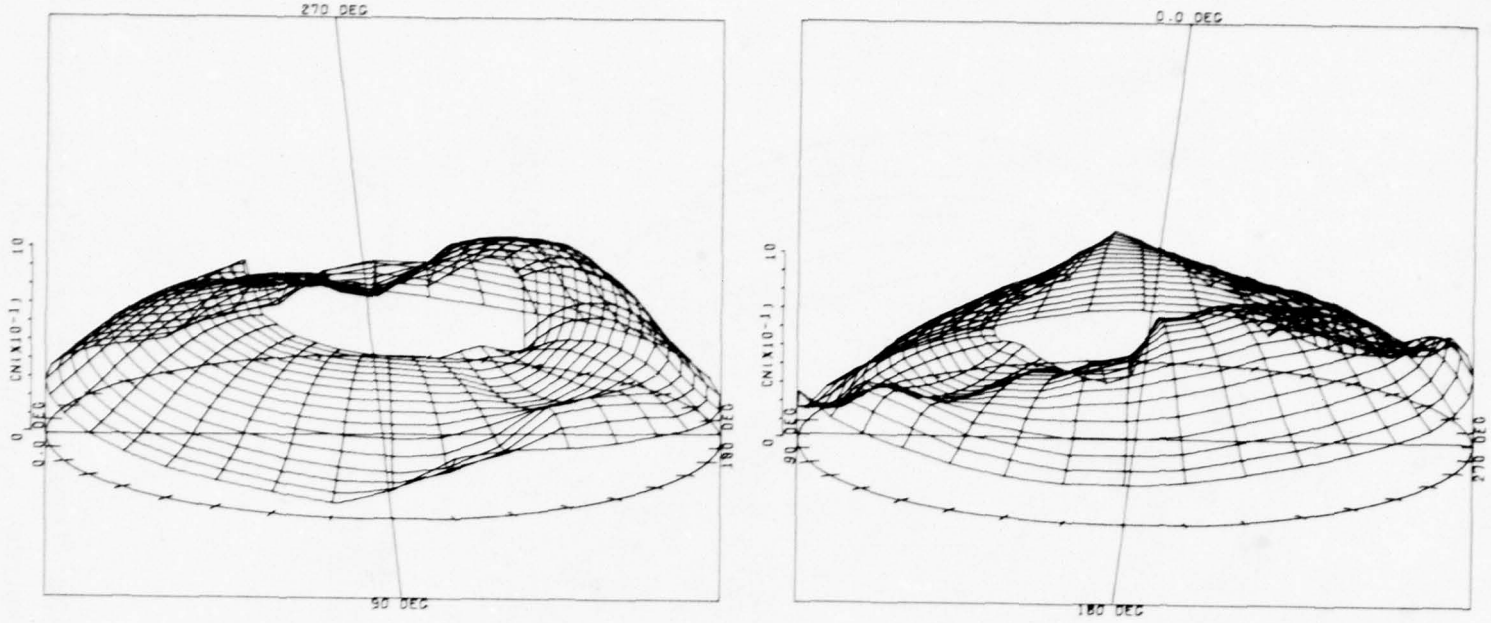

Figure 17B. C_N surface plots (level flight at 30 knots, gross weight 9000 pounds, altitude 50 feet).

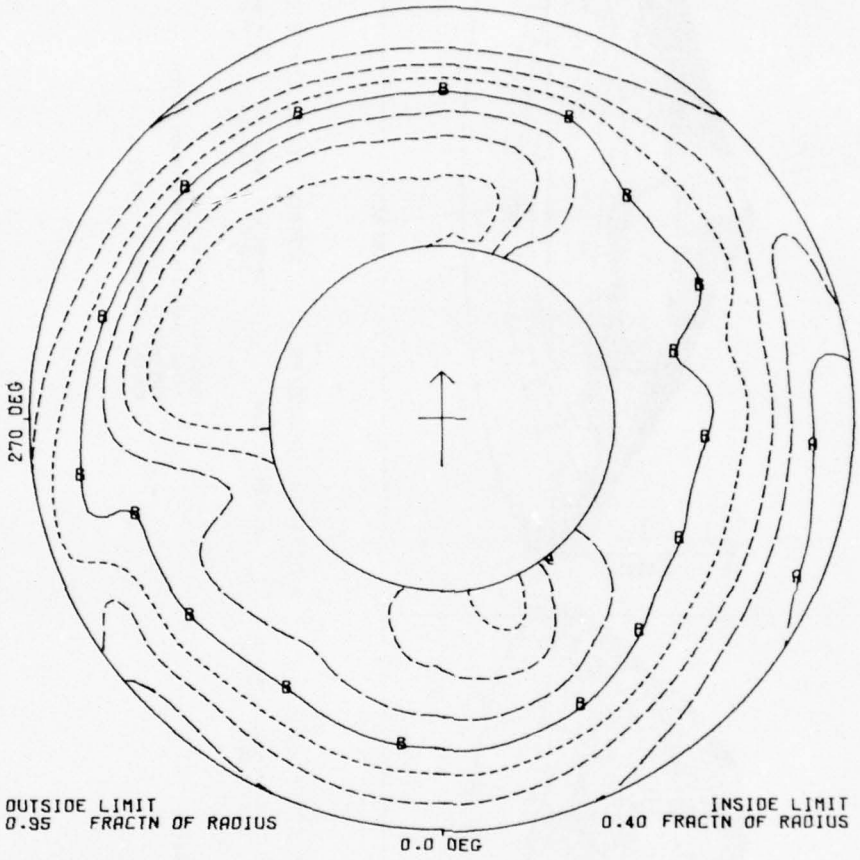

DERIVED PARAMETER - NORMAL FORCE COEFFICIENT

COUNTER 727

GROSS WT 8100. SHIP MODEL AH-1G
LONG CG 196.5 SHIP ID 20391

A ——— 0.1 CN
B ——— 0.5 CN

Figure 18A. C_N contour plot (level flight at 40 knots, gross weight 8100 pounds, altitude 50 feet).

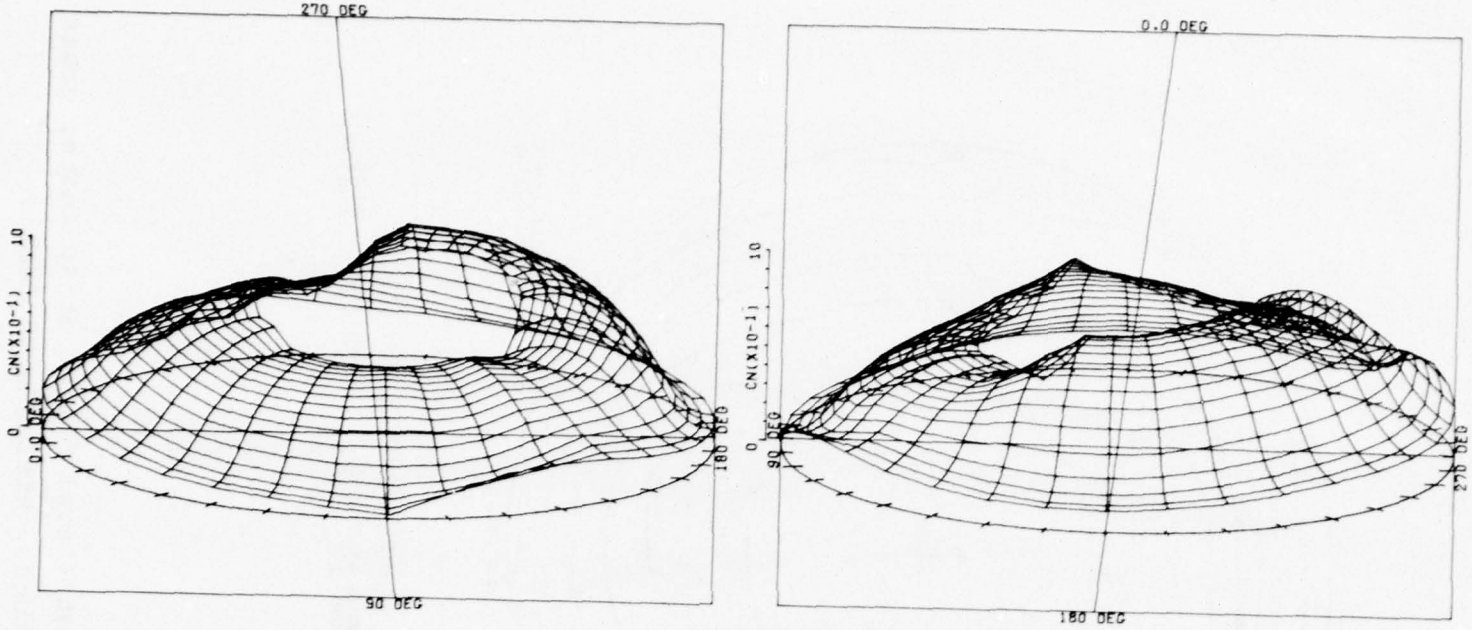

Figure 18B. C_N surface plots (level flight at 40 knots, gross weight 8100 pounds, altitude 50 feet).

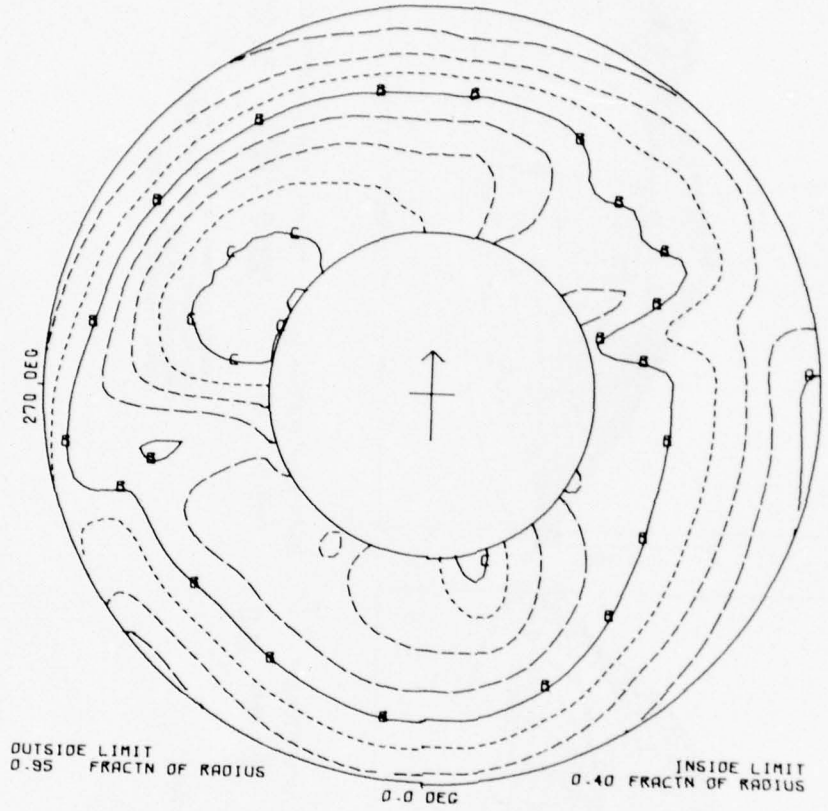

Figure 19A. C_N contour plot (level flight at 40 knots, gross weight 9000 pounds, altitude 50 feet).

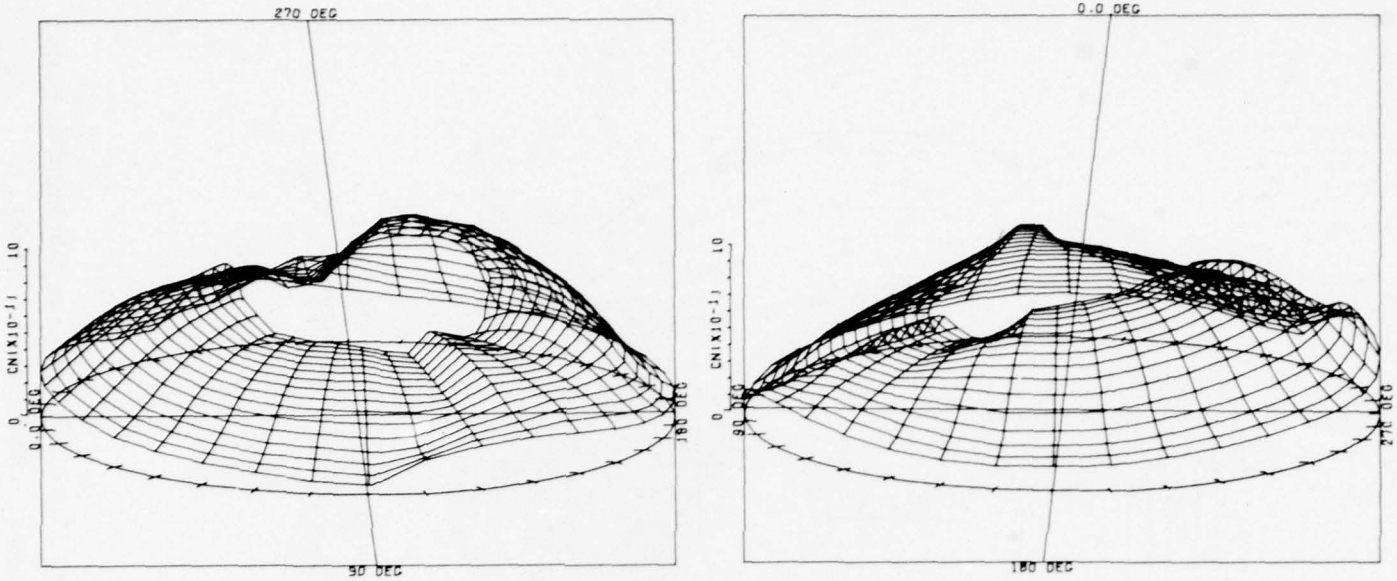

Figure 19B. C_N surface plots (level flight at 40 knots, gross weight 9000 pounds, altitude 50 feet).

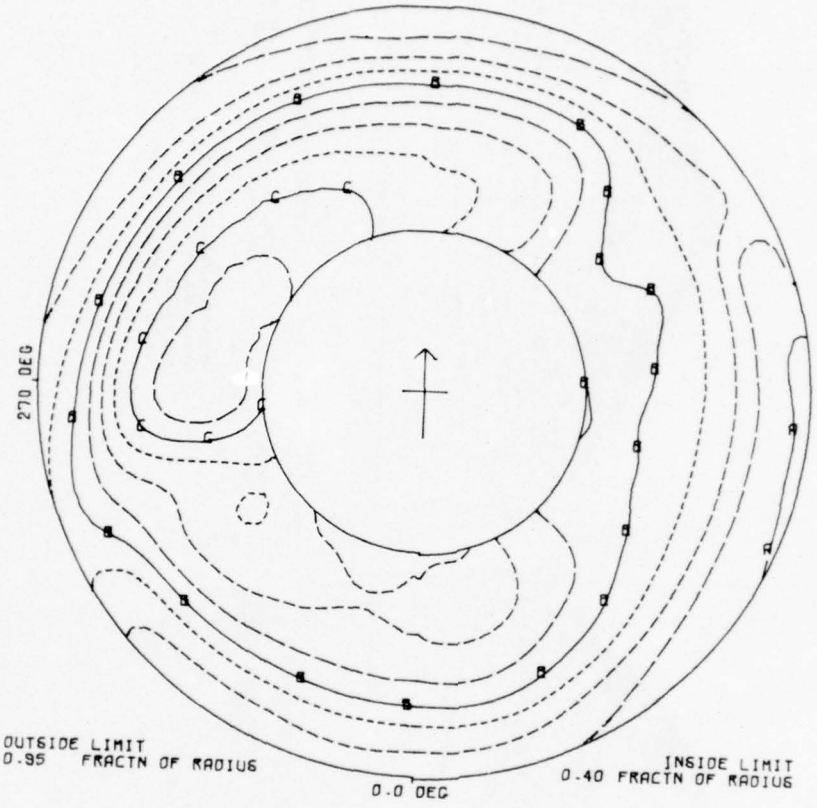

Figure 20A. C_N contour plot (level flight at 50 knots, gross weight 8100 pounds, altitude 50 feet).

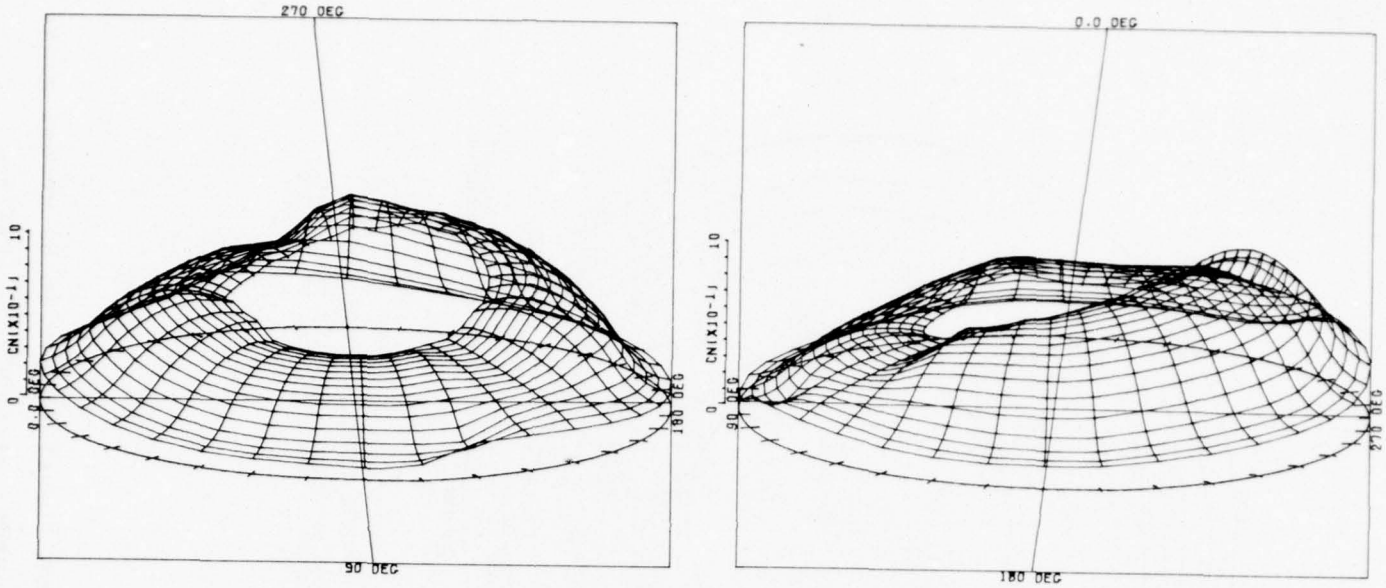

Figure 20B. C_N surface plots (level flight at 50 knots, gross weight 8100 pounds, altitude 50 feet).

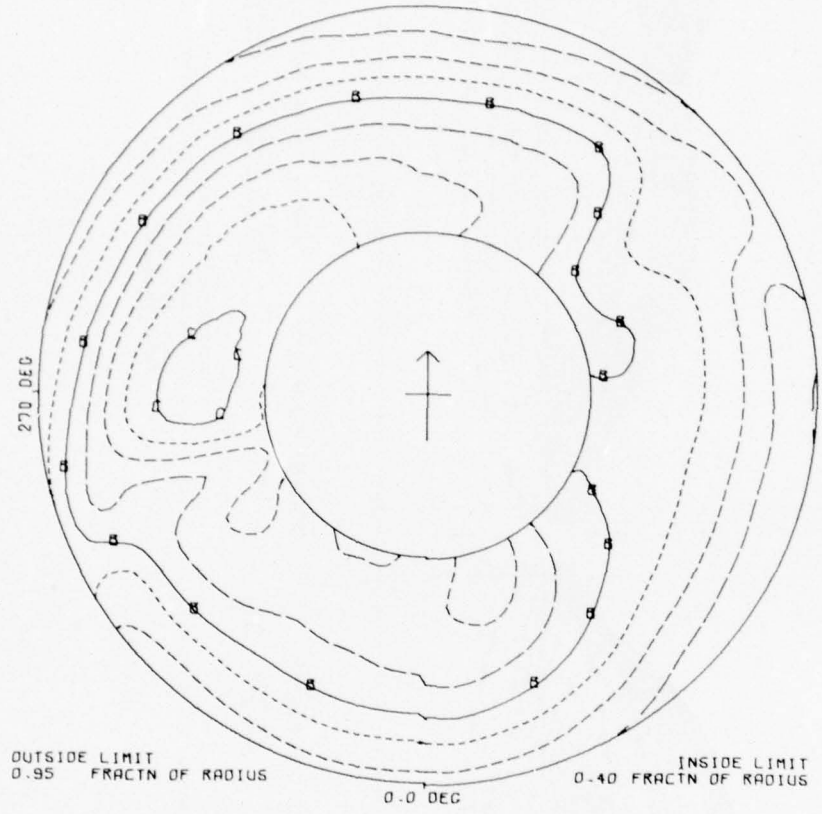

Figure 21A. C_N contour plot (level flight at 50 knots, gross weight 9000 pounds, altitude 50 feet).

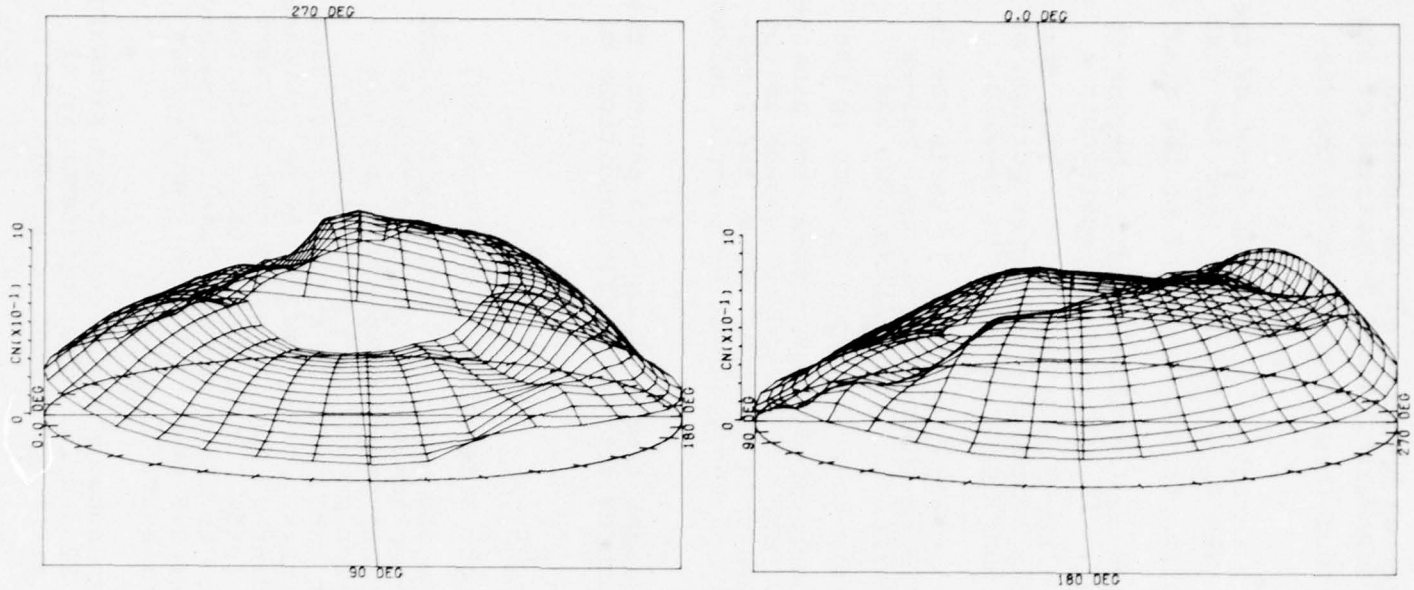

DERIVED PARAMETER - NORMAL FORCE COEFFICIENT

COUNTER 690 GROSS WT 9000. SHIP MODEL AH-1G
LONG CG 196.2 SHIP ID 20391

ANGULAR INCREMENT 10 DEG
RADIAL QUANTITY FRACTN OF RADIUS
MAX RADIUS 0.955
RADIAL INCREMENT 0.0370

DERIVED PARAMETER - NORMAL FORCE COEFFICIENT

COUNTER 690 GROSS WT 9000. SHIP MODEL AH-1G
LONG CG 196.2 SHIP ID 20391

ANGULAR INCREMENT 10 DEG
RADIAL QUANTITY FRACTN OF RADIUS
MAX RADIUS 0.955
RADIAL INCREMENT 0.0370

Figure 21B. C_N surface plots (level flight at 50 knots, gross weight 9000 pounds, altitude 50 feet).

The upwash induced by the vortex upstream of its location increases the C_N while the downwash induced downstream of its location decreases the C_N, thus forming a valley in the distribution.

At 20 knots the tip vortex interaction across the front of the disc begins to disappear. The C_N distribution over the disc evens out as the loading shifts toward the front of the disc.

At 30 knots the blade loading in the third quadrant begins to build up midway out the span. In addition, C_N approaches a value of 1.0 over the engine nacelle at $r/R = 0.4$. This rise appears to be due to the wake coming off the upper portion of the sail and the plate surrounding the top of the nacelle.

With a further increase in airspeed to 40 and 50 knots the inboard blade loading in the third quadrant approaches values of C_N of 1.0 or more. Concurrently, the C_N bump over the engine nacelle begins to diminish. The rapid C_N drop in the region of $\psi = 280$ degrees corresponds to a vortex core passage parallel to the blade span. The vortex induces upwash as the blade approaches and downwash upon passage. Thus, the interaction results in a gradual loading followed by a rapid unloading of the blade.

With an increase in gross weight from 8100 to 9000 pounds, the gradients become more pronounced for the flight conditions of 20, 30, 40, and 50 knots.

Right and Left Sideward Flight

The C_N distributions for right sideward flight (Figure 22) compare favorably with those shown for 30-knot forward flight (Figure 16). However, some noticeable differences between these two flight conditions are seen in Table 3. In right sideward flight the main rotor power is 16 percent higher than for the forward flight case. Simple energy methods show that approximately half of this increase is due to an increase in equivalent fuselage drag area from 12 square feet (forward flight) to 150 square feet (sideward flight). Also, with the rotor's thrust vector tilted to the right the fuselage reaches an equilibrium roll angle of 3.5 degrees to the right versus 1.4 degrees to the left in forward flight.

Left sideward flight differs substantially from right sideward flight, as seen in Figures 22 and 23. The difference is attributed to the change in tail rotor thrust direction. In

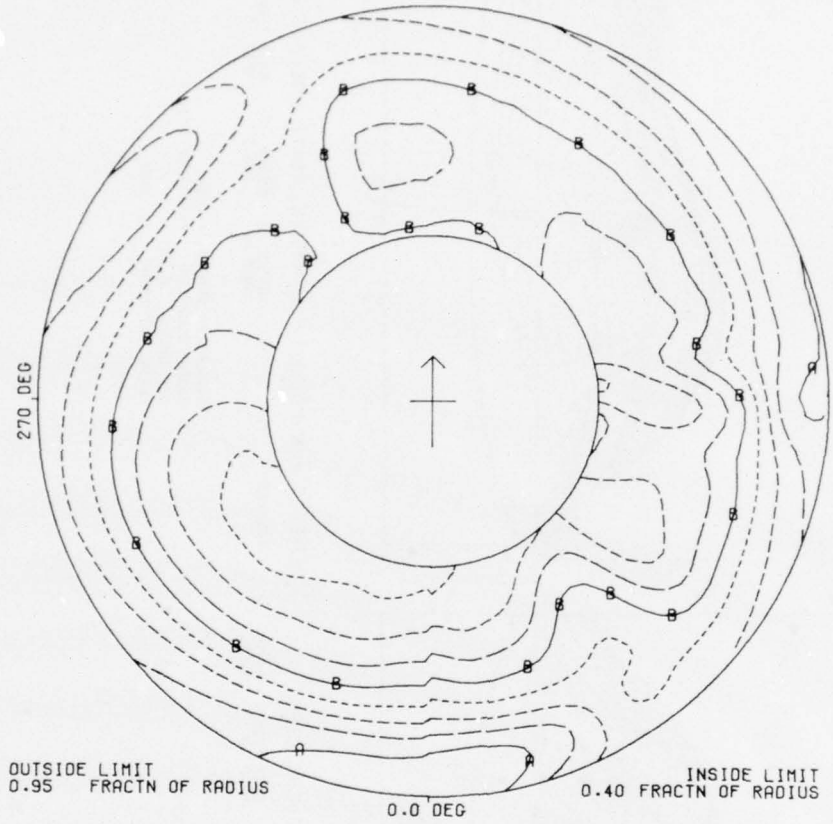

DERIVED PARAMETER - NORMAL FORCE COEFFICIENT

COUNTER 717

GROSS WT 8100. SHIP MODEL AH-1G
LONG CG 196.5 SHIP ID 20391

A ——— 0.1 CN
B ——— 0.5 CN

Figure 22A. C_N contour plot (right sideward flight at 30 knots, gross weight 8100 pounds, altitude 50 feet).

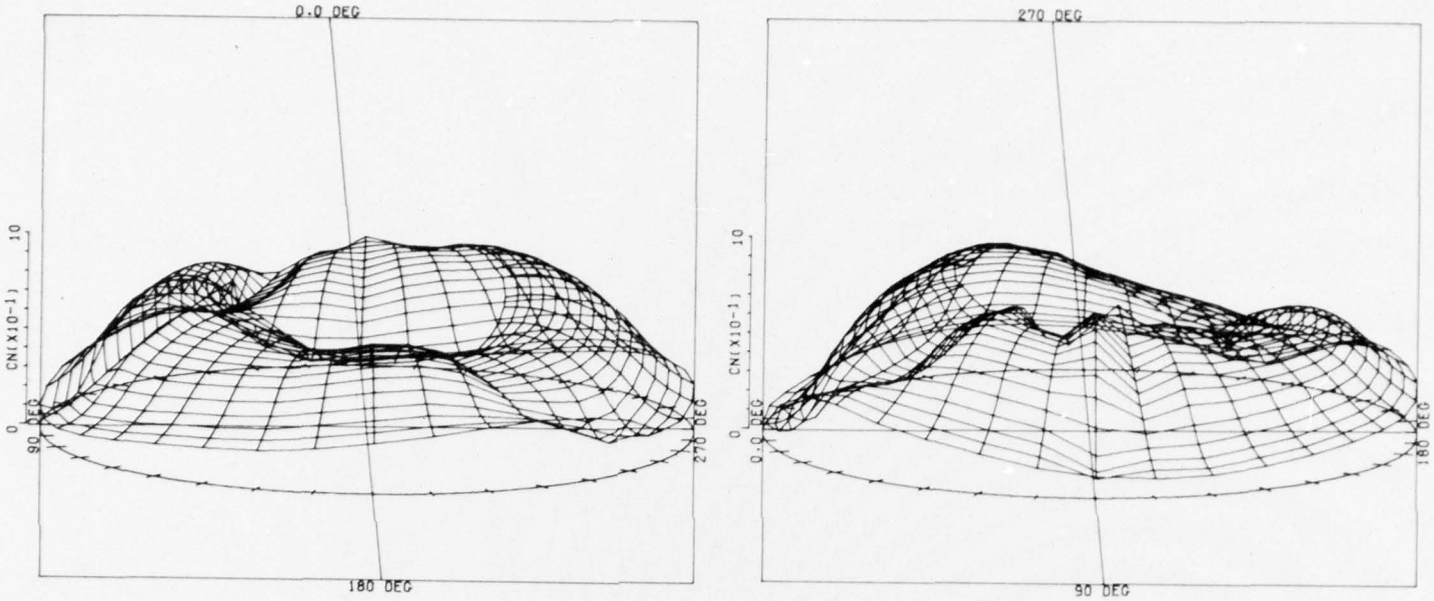

DERIVED PARAMETER - NORMAL FORCE COEFFICIENT

COUNTER 717 GROSS WT 8100 SHIP MODEL AH-1G
LONG CG 196.5 SHIP ID 20391

ANGULAR INCREMENT 10 DEG
RADIAL QUANTITY FRACTN OF RADIUS
MAX RADIUS 0.955
RADIAL INCREMENT 0.0370

DERIVED PARAMETER - NORMAL FORCE COEFFICIENT

COUNTER 717 GROSS WT 8100 SHIP MODEL AH-1G
LONG CG 196.5 SHIP ID 20391

ANGULAR INCREMENT 10 DEG
RADIAL QUANTITY FRACTN OF RADIUS
MAX RADIUS 0.955
RADIAL INCREMENT 0.0370

Figure 22B. C_N surface plots (right sideward flight at 30 knots, gross weight 8100 pounds, altitude 50 feet).

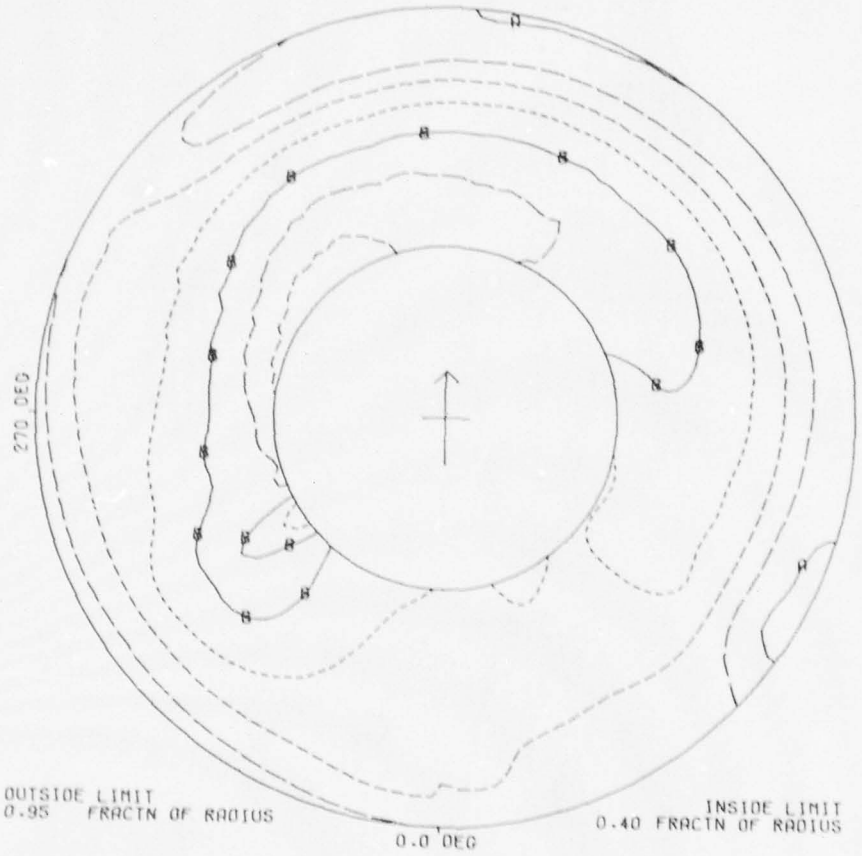

DERIVED PARAMETER - NORMAL FORCE COEFFICIENT

COUNTER 720

GROSS WT 8100. SHIP MODEL AH-1G
LONG CG 196.5 SHIP ID 20391

0.2 CN
0.6 CN

Figure 23A. C_N contour plot (left sideward flight at 30 knots, gross weight 8100 pounds, altitude 50 feet).

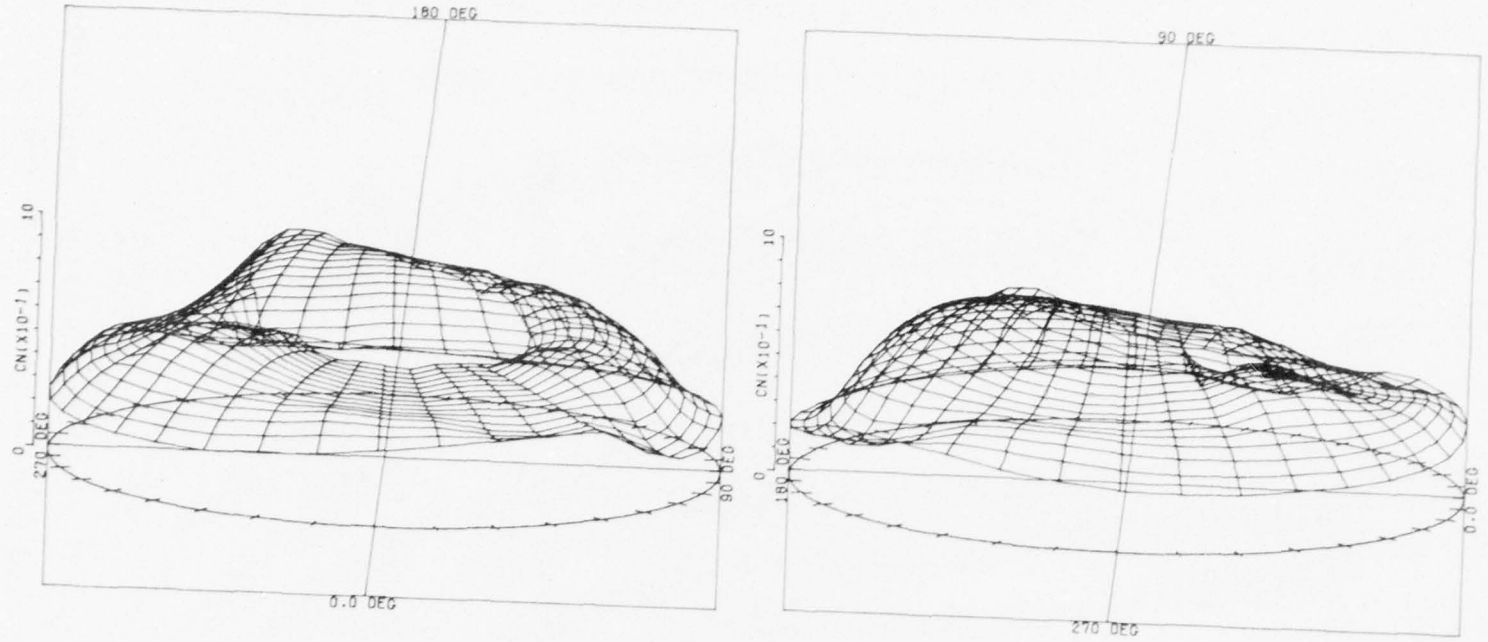

Figure 23B. C_N surface plots (left sideward flight at 30 knots, gross weight 8100 pounds, altitude 50 feet).

right sideward flight, the tail rotor thrust is in the same direction as the main rotor's propulsive force component; whereas in left sideward flight, the tail rotor thrusts in opposite direction to the main rotor's propulsive force. Thus, the main rotor must also overcome the tail rotor thrust in left sideward flight. Main rotor power is about 6 percent more than for right sideward flight, as seen in Table 3. Fuselage roll angle for left sideward flight is 6.9 degrees to the left, which is about twice the magnitude of that present to the right during right sideward flight.

COMPARISON BETWEEN MEASURED AND PREDICTED NORMAL FORCE COEFFICIENTS

For the steady state flight conditions, comparisons were made between measured C_N versus ψ distributions and calculated values of C_L. For comparative purposes, the two parameters are approximately equal. These comparisons were made for radial stations of $r/R = 0.40$, 0.75, 0.864, and 0.955.

Hover

In hover, BHT's lifting surface hover performance program (AR79DK) was used for calculating the C_L distributions. This analysis represents the state of the art in the prediction of hover performance. The main features of the analysis are:

- Lifting surface blade representation.
- Determination of blade section aerodynamic characteristics through circulation response tailoring.
- Prescribed wake model coupled to blade circulation as determined by an extensive experimental wake data base.
- Compressibility treated through similarity law geometry transformation and airfoil data.

Figures 24 through 26 show the 8100-pound gross weight hover records (number 723 and 736) at 100- and 50-foot altitudes, respectively, and the 9000-pound record (number 685) at a 50-foot altitude. Ideally, C_N would be constant with azimuth, as were the calculated values of C_L. However, because of the presence of light wind and fuselage influences, this situation is never fully realized. In spite of the unsteadiness associated with the measured data, the calculated results are in reasonable agreement.

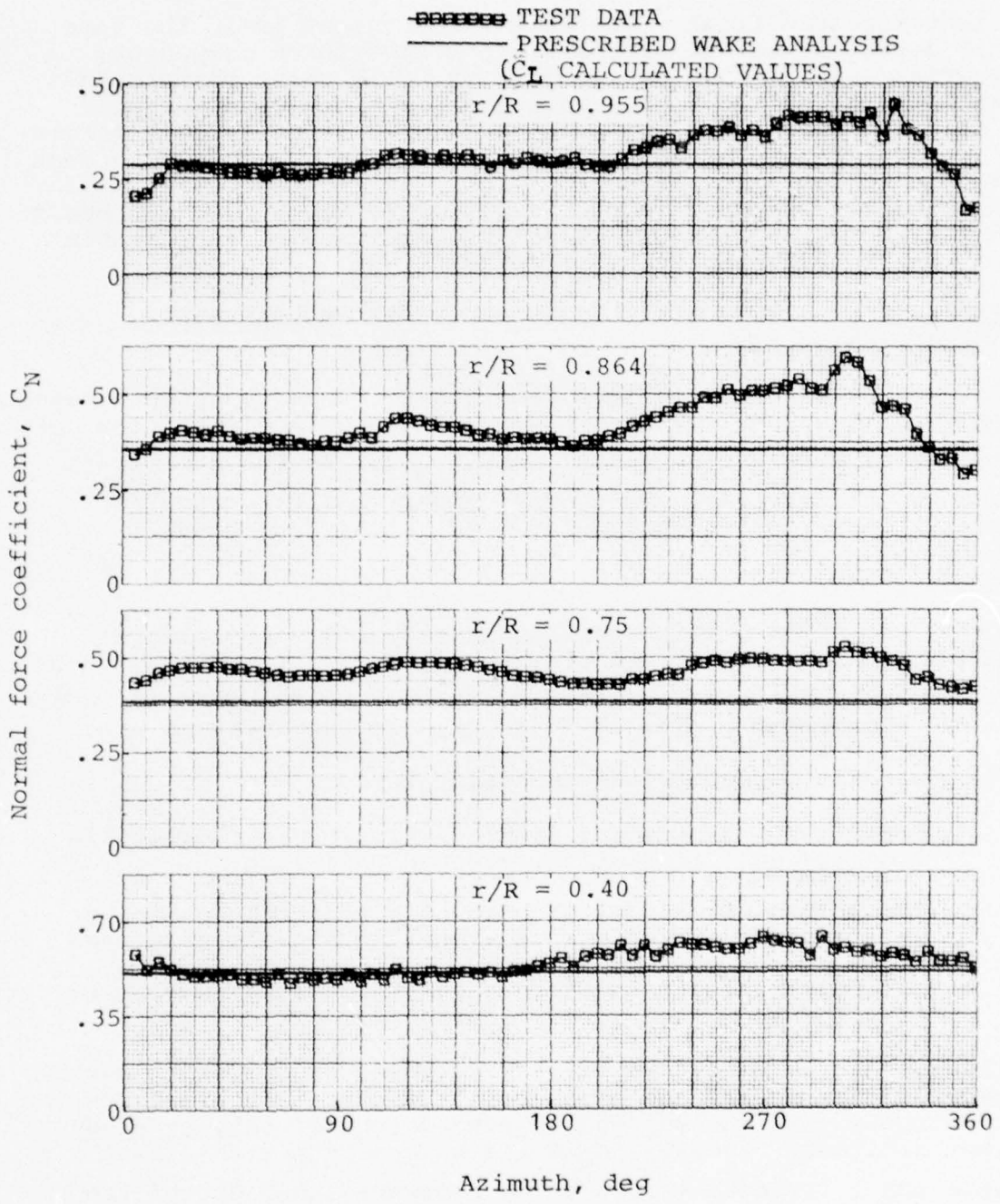

Figure 24. Comparison of measured and predicted normal force coefficients, record 723, 8100 pounds gross weight, OGE hover at 100 feet.

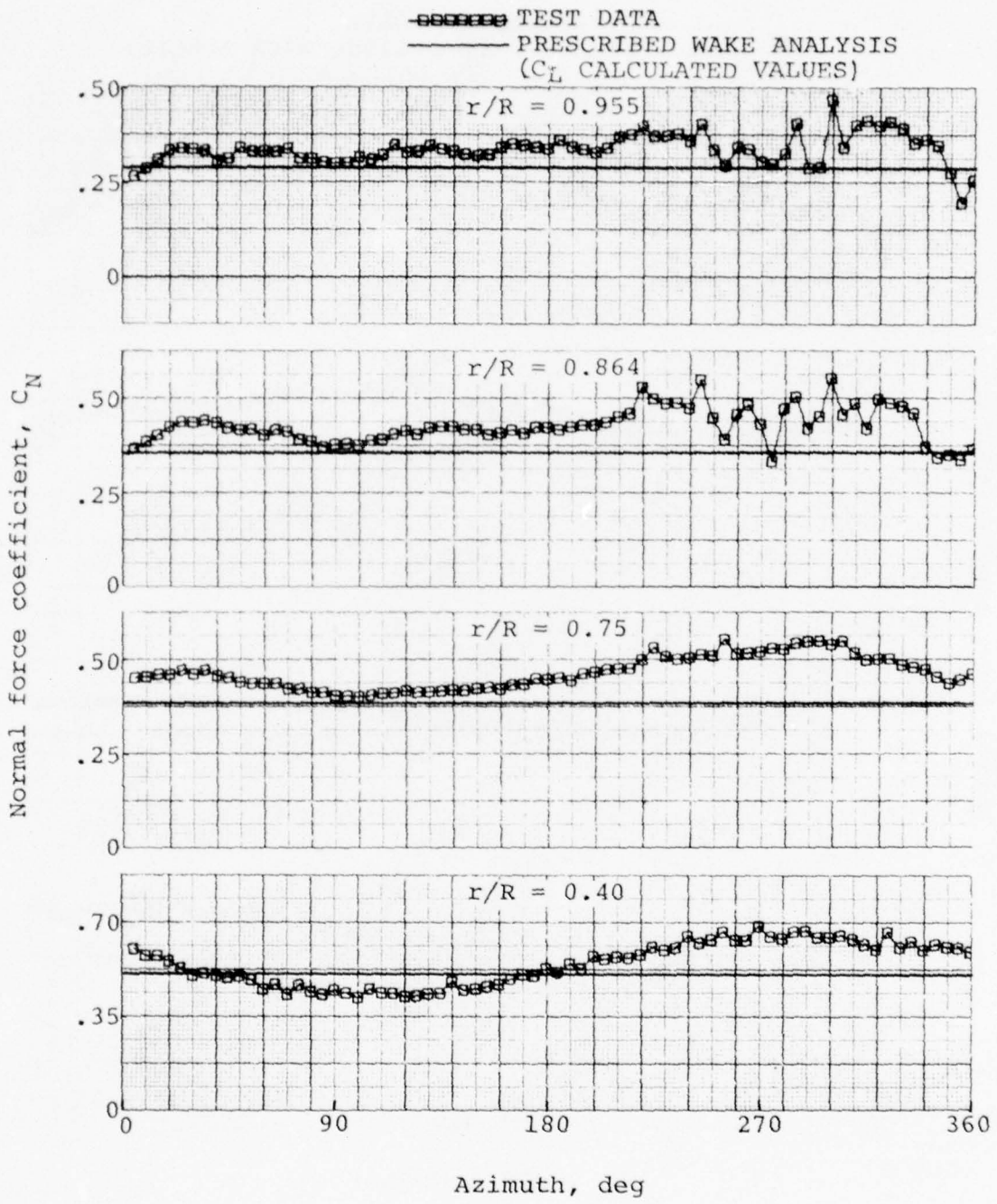

Figure 25. Comparison of measured and predicted normal force coefficients, record 736, 8100 pounds gross weight, 360-degree turn - record at 0 degrees at 50 feet.

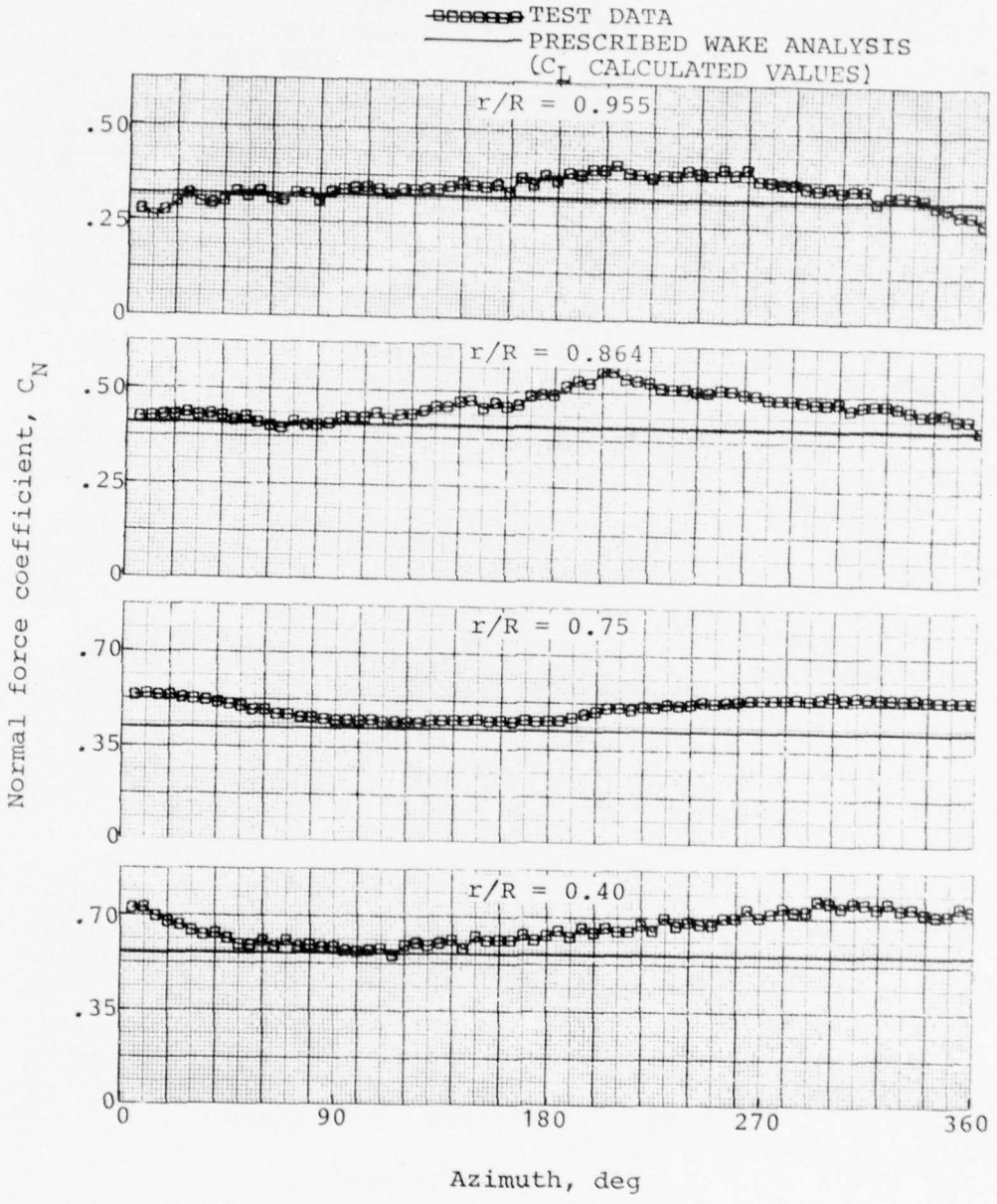

Figure 26. Comparison of measured and predicted normal force coefficients, record 685, 9000 pounds gross weight , OGE hover at 50 feet.

Forward Flight 10, 20, 30, 40, and 50 Knots

For the forward flight comparison of the measured C_N distributions with blade element/momentum analysis, the calculated C_L versus azimuth distributions were obtained using BHT's Rotor Aerodynamic Characteristics Program (ARAM42). This program assumes uniform inflow, and the flapping equation of motion is solved iteratively for the specified flight condition. A standard tip-loss factor is used based on the thrust coefficient and number of blades. For the clean 8100-pound gross weight condition, a fuselage drag area of 12 square feet was used, whereas for the 9000-pound "Hog Configuration," the fuselage drag area was 15 square feet.

For the forward flight speeds of 10, 20, 30, 40, and 50 knots, correlation between the measured and calculated C_N distributions (as shown in Figures 27 through 38) resulted in the following generalizations. In the vicinity of the blade tip, uniform inflow is insufficient in magnitude. Consequently, the calculated C_L versus azimuth is high compared to the C_N versus azimuth distribution. Inboard of $r/R = 0.75$ uniform inflow is excessive and the calculated C_L versus azimuth is low compared to the measured C_N versus azimuth distribution. These trends become less obvious as the forward flight speed diminishes. In addition, the measured C_N distributions, particularly those at $r/R = 0.864$ and 0.955, show large fluctuations in the region of $\psi = 90°$ and 270° azimuth due to blade/vortex interactions. Calculated results using uniform inflow neglect these fluctuations.

In an attempt to account for the tip vortex induced fluctuations in the forward flight inflow, a distorted wake analysis (ARAPMWK) was used to calculate the resultant C_L distributions. Comparisons were made only for 40- to 50-knot, 8100-pound cases (records 727 and 728). Lower speed comparisons were not possible because of the numerical problems associated with the free-wake analysis. Figures 33 and 35 show the calculated distorted wake C_L distributions relative to the test data. In both cases the calculated C_L fluctuations due to the vortex interaction occur where expected, but are much greater in magnitude than those measured. A visual representation of the wake relative to the rotor as calculated by ARAPMWK for the 50-knot case is shown in Figure 39.

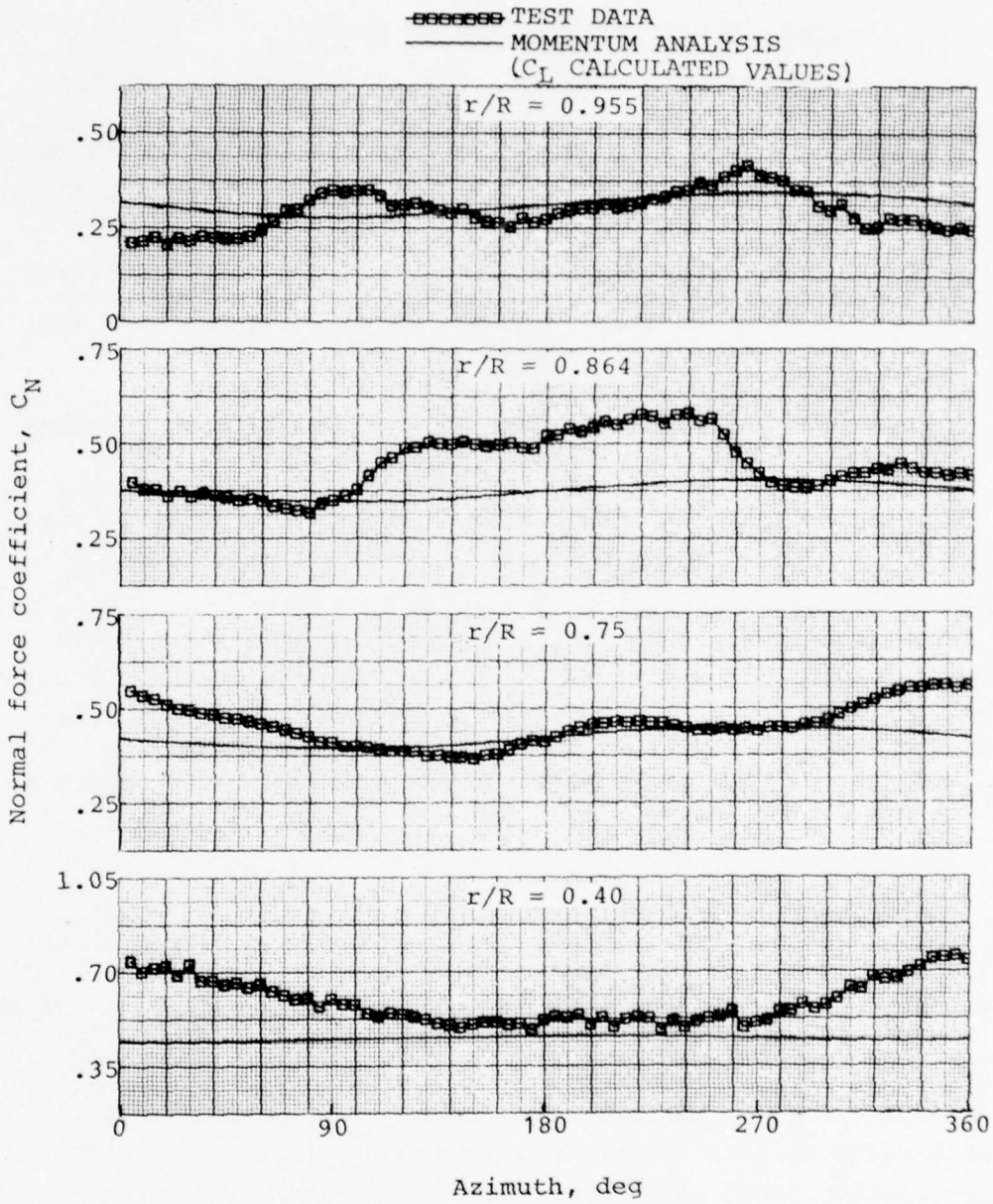

Figure 27. Comparison of measured and predicted normal force coefficients, record 724, 8100 pounds gross weight, forward flight at 10 knots.

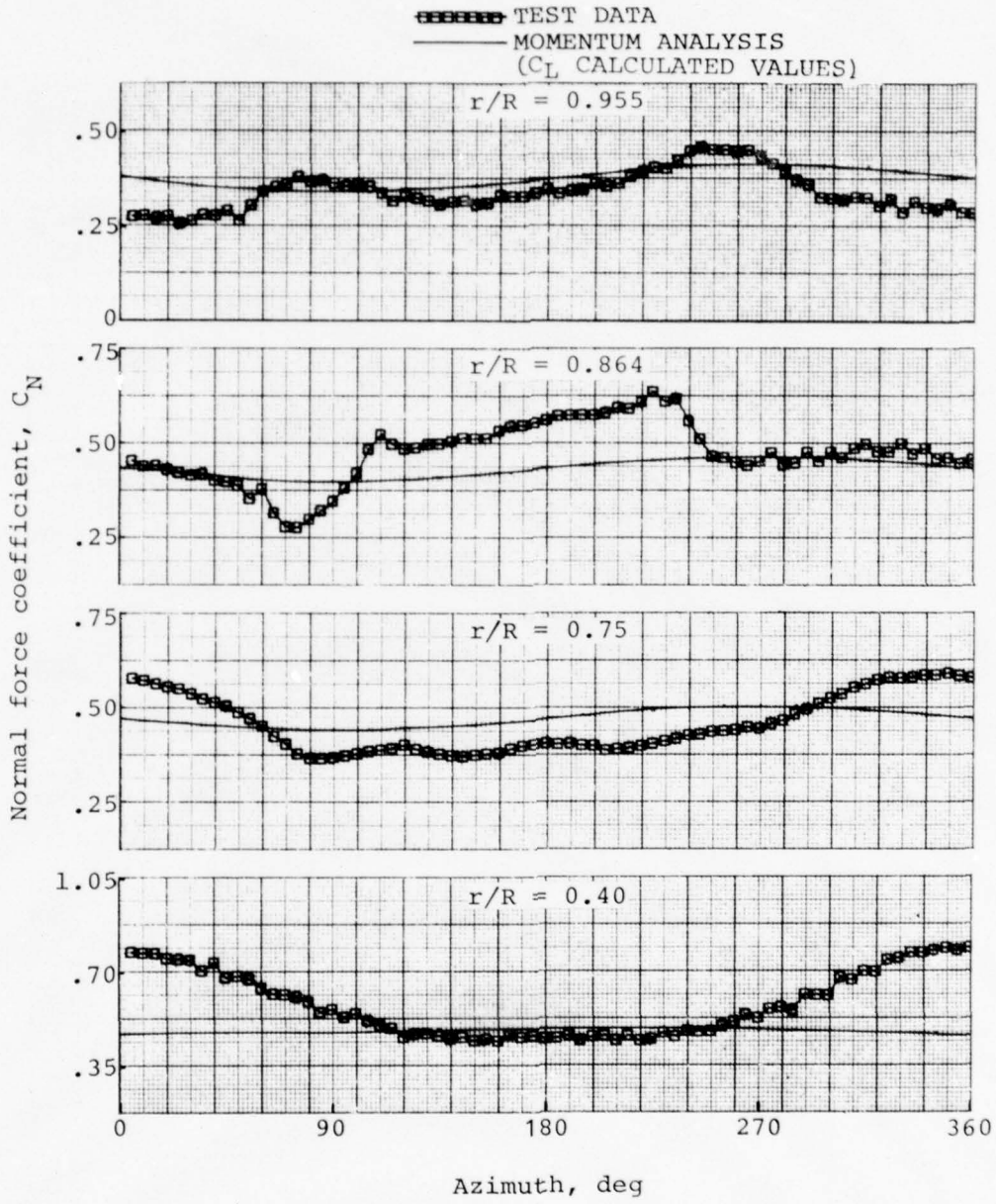

Figure 28. Comparison of measured and predicted normal force coefficients, record 686, 9000 pounds gross weight, forward flight at 10 knots.

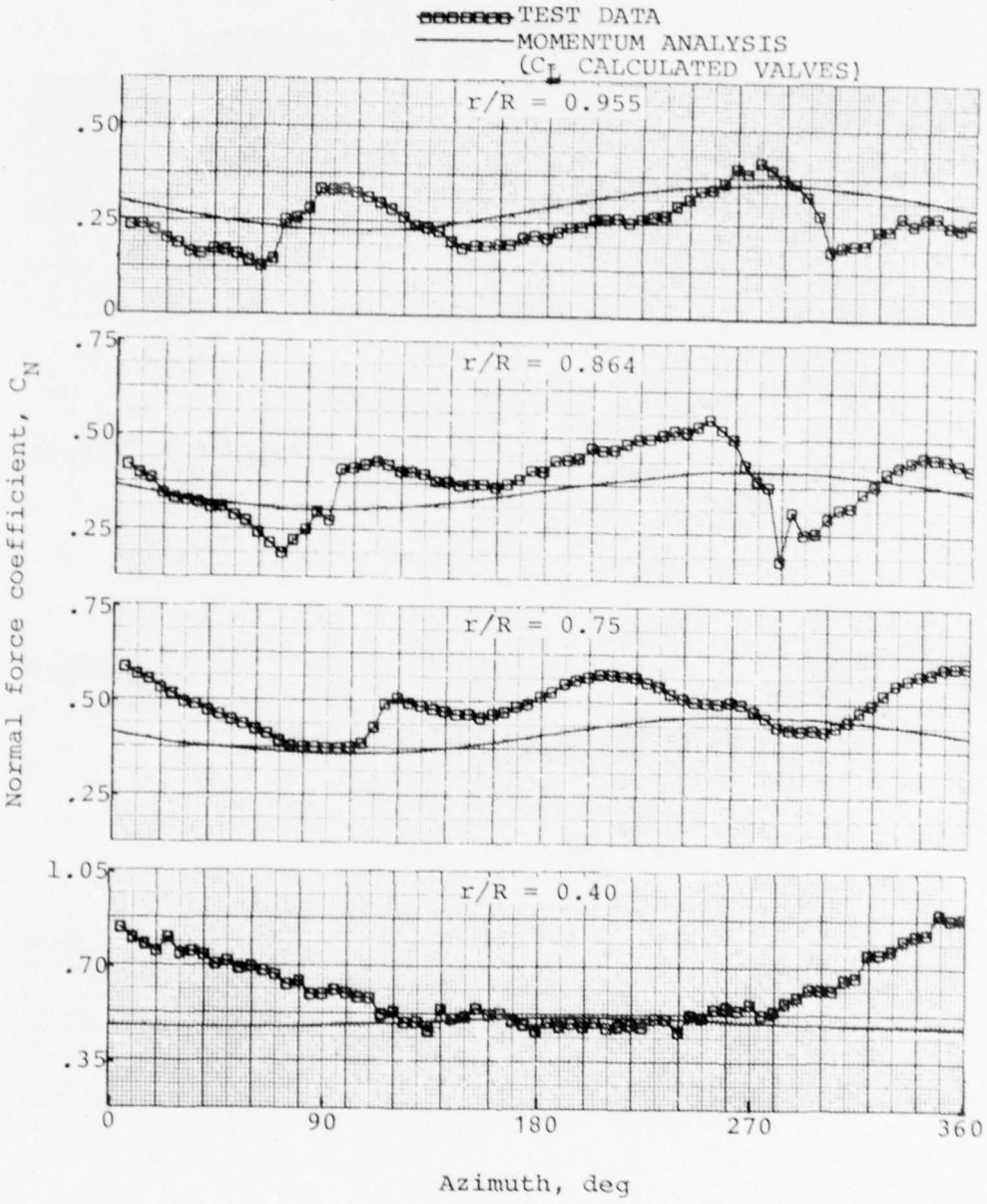

Figure 29. Comparison of measured and predicted normal force coefficients, record 725, 8100 pounds gross weight, forward flight at 20 knots.

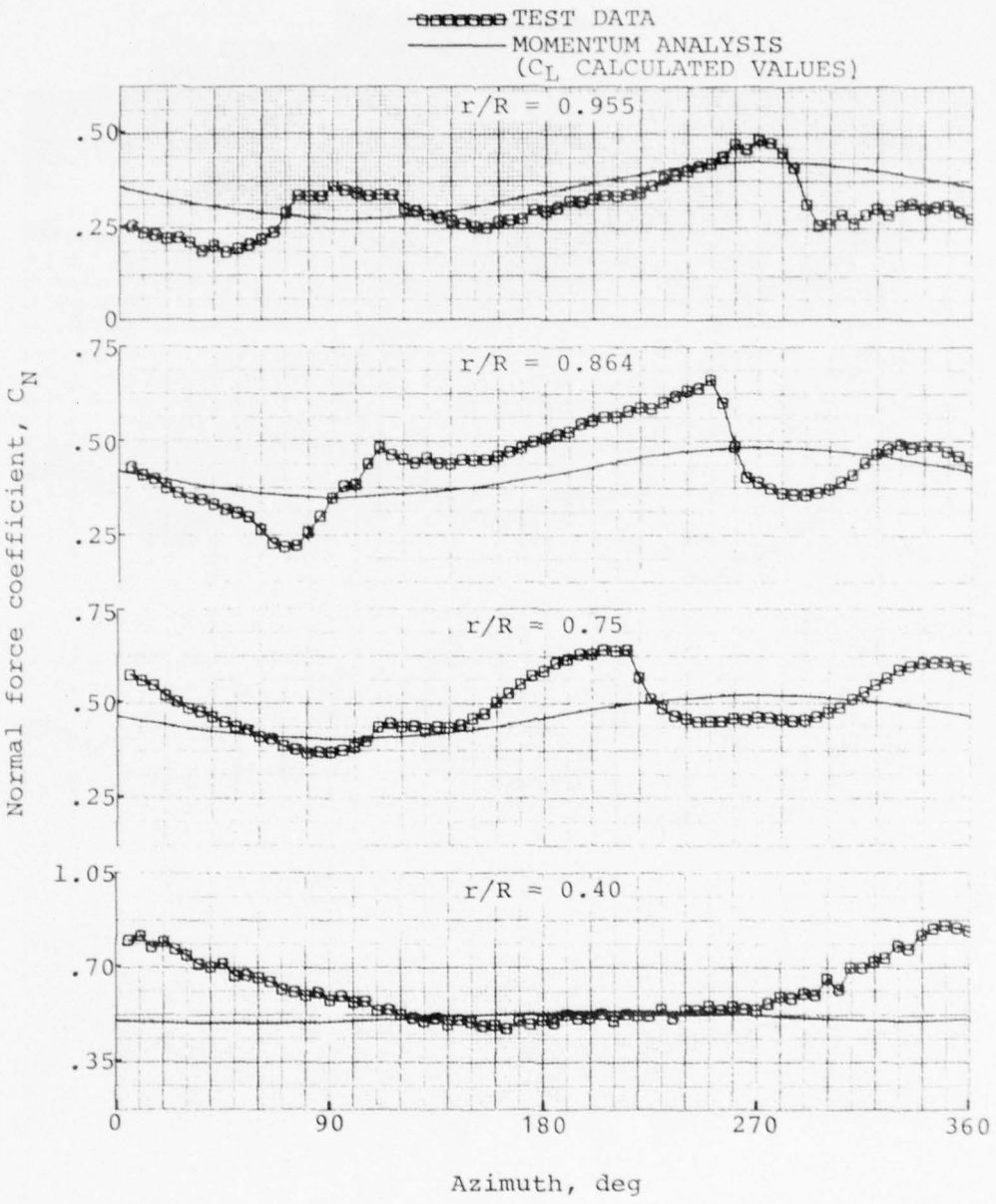

Figure 30. Comparison of measured and predicted normal force coefficients, record 687, 9000 pounds gross weight, forward flight at 20 knots.

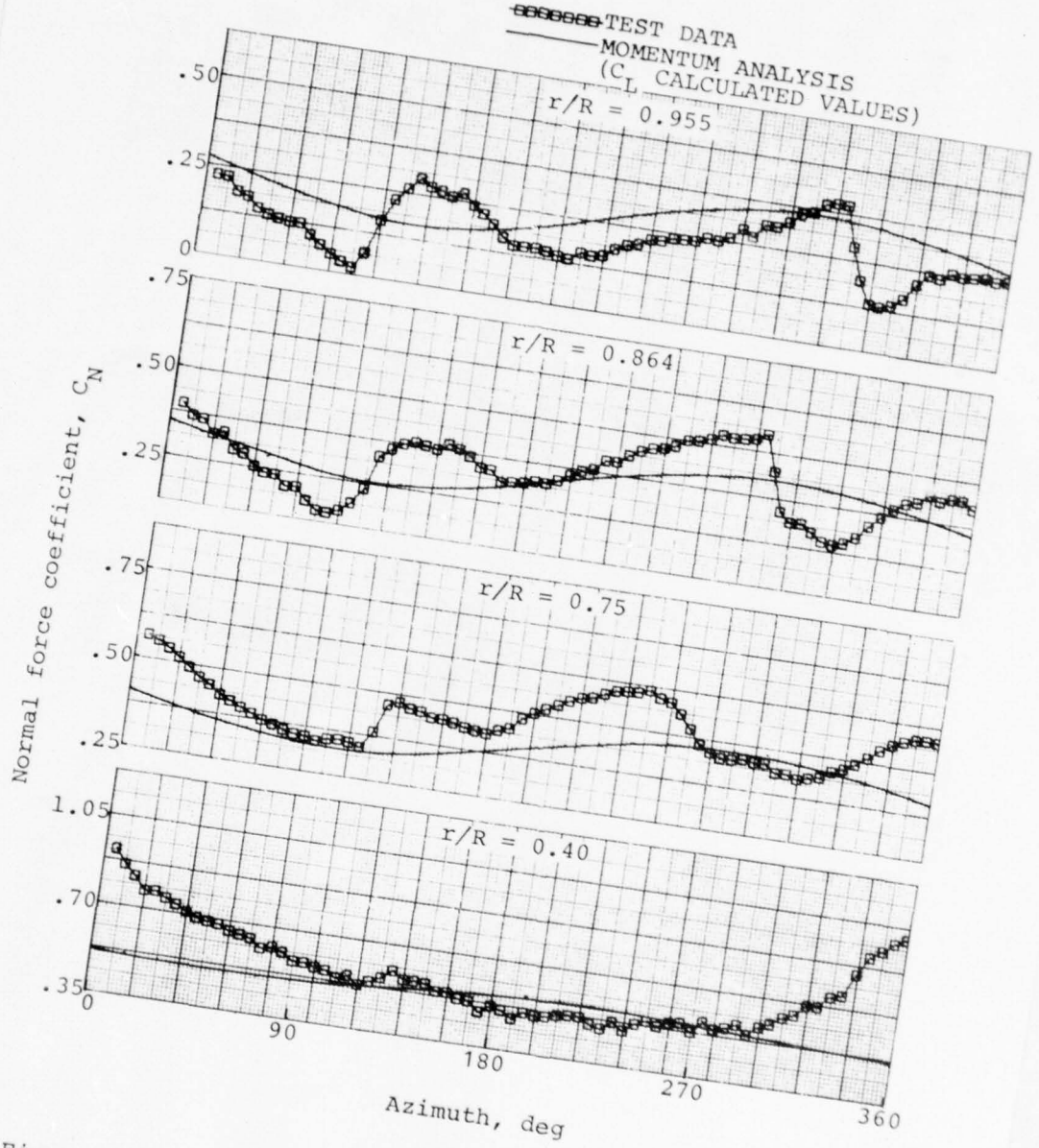

Figure 31. Comparison of measured and predicted normal force coefficients, record 726, 8100 pounds gross weight, forward flight at 30 knots.

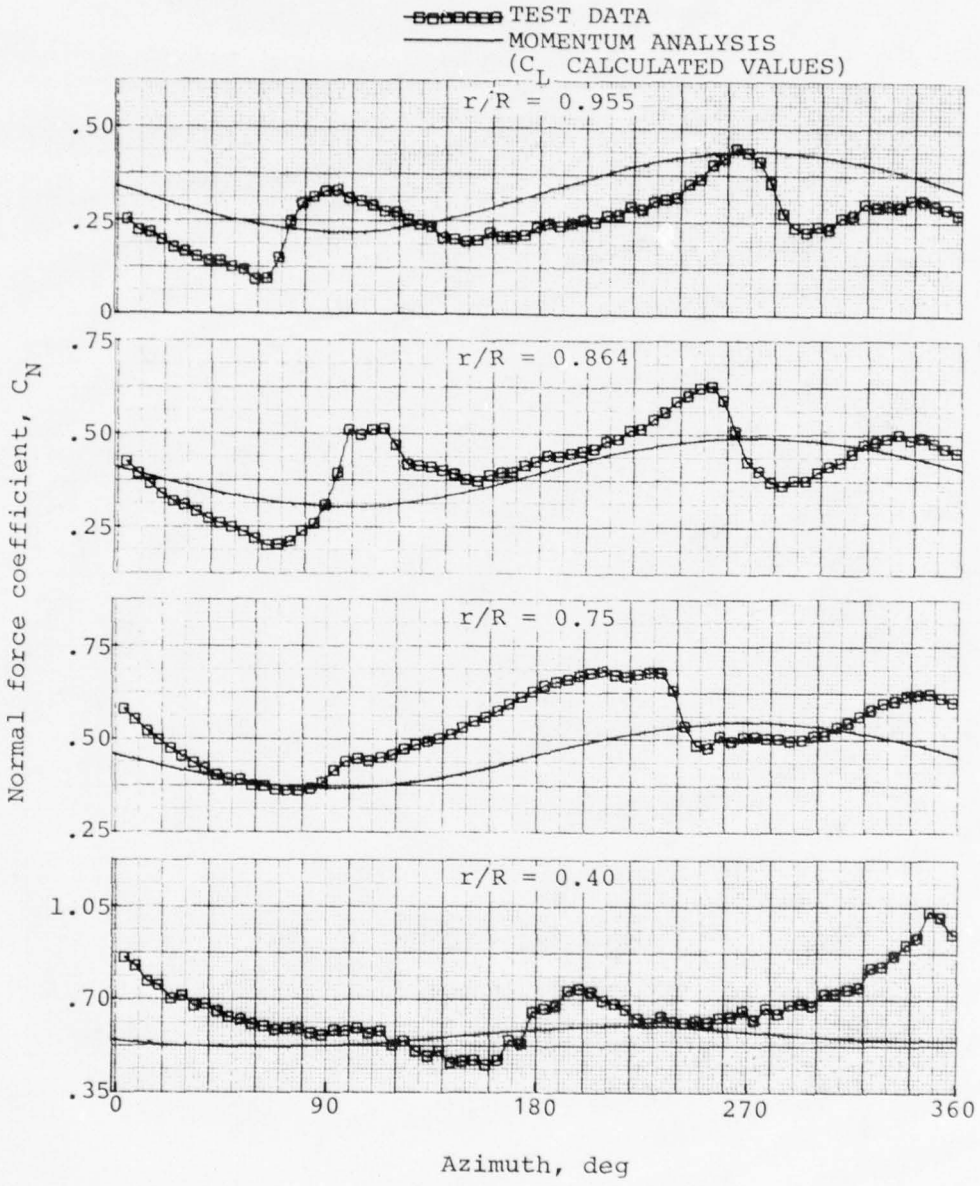

Figure 32. Comparison of measured and predicted normal force coefficients, record 688, 9000 pounds gross weight, forward flight at 30 knots.

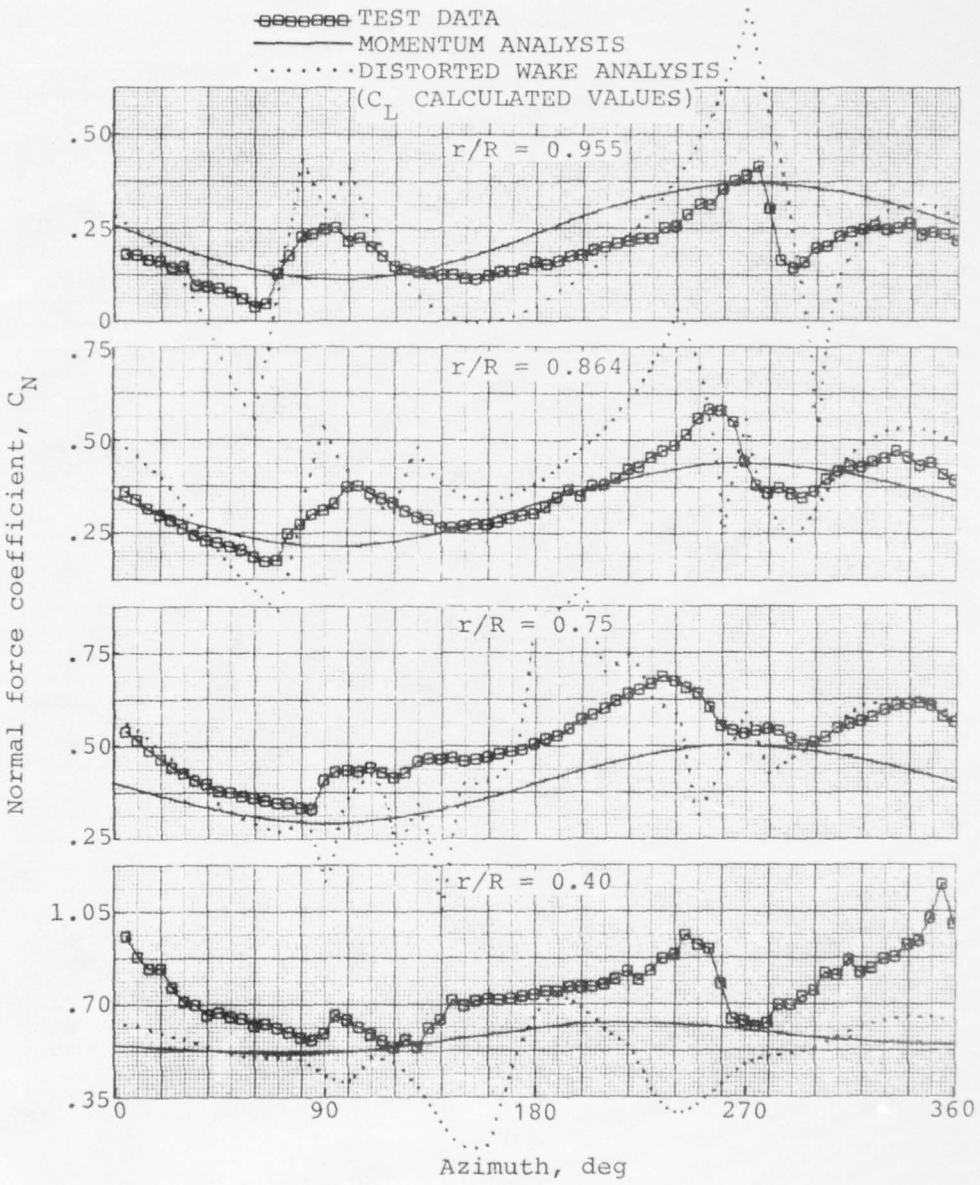

Figure 33. Comparison of measured and predicted normal force coefficients, record 727, 8100 pounds gross weight, forward flight at 40 knots.

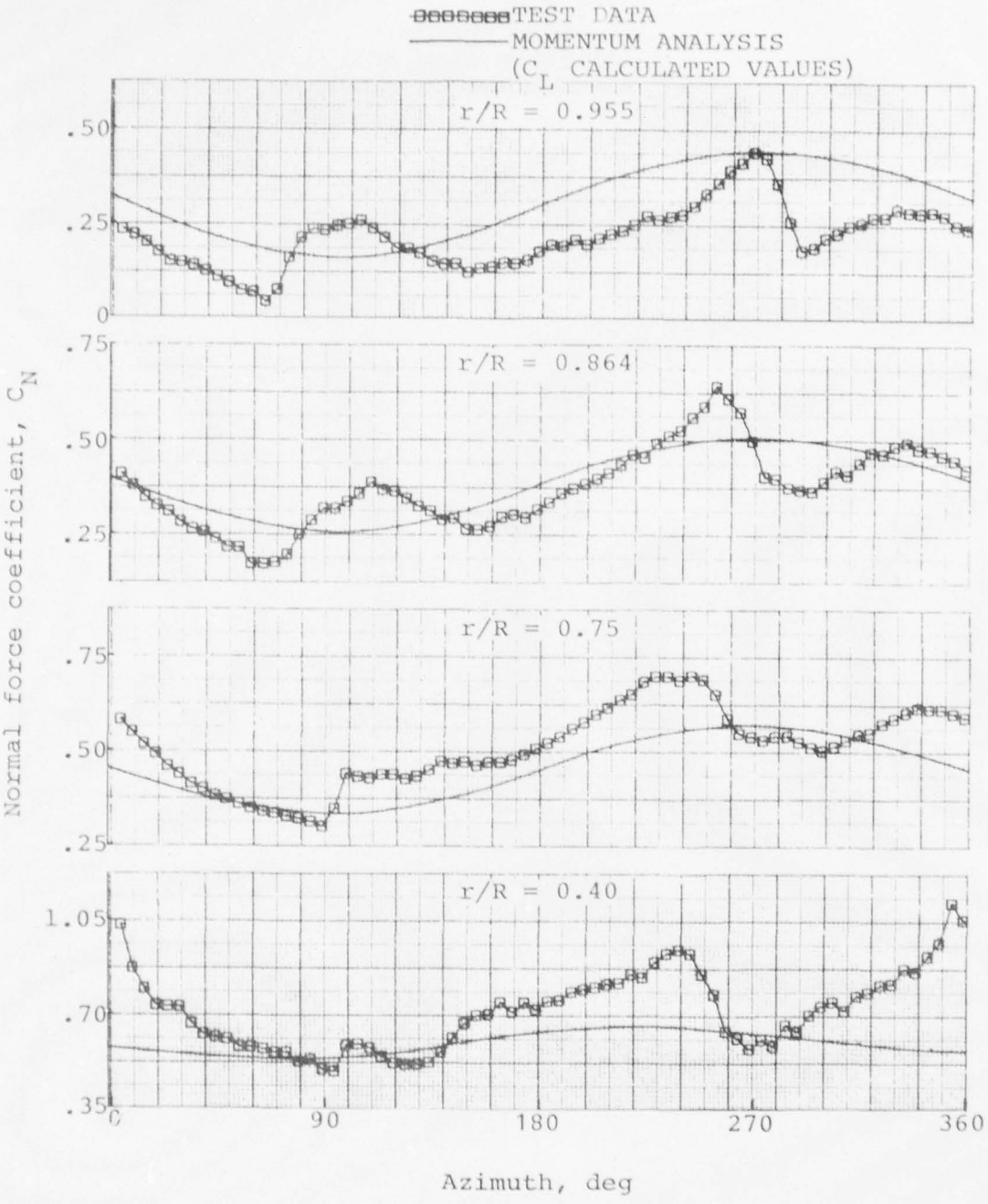

Figure 34. Comparison of measured and predicted normal force coefficients, record 689, 9000 pounds gross weight, forward flight at 40 knots.

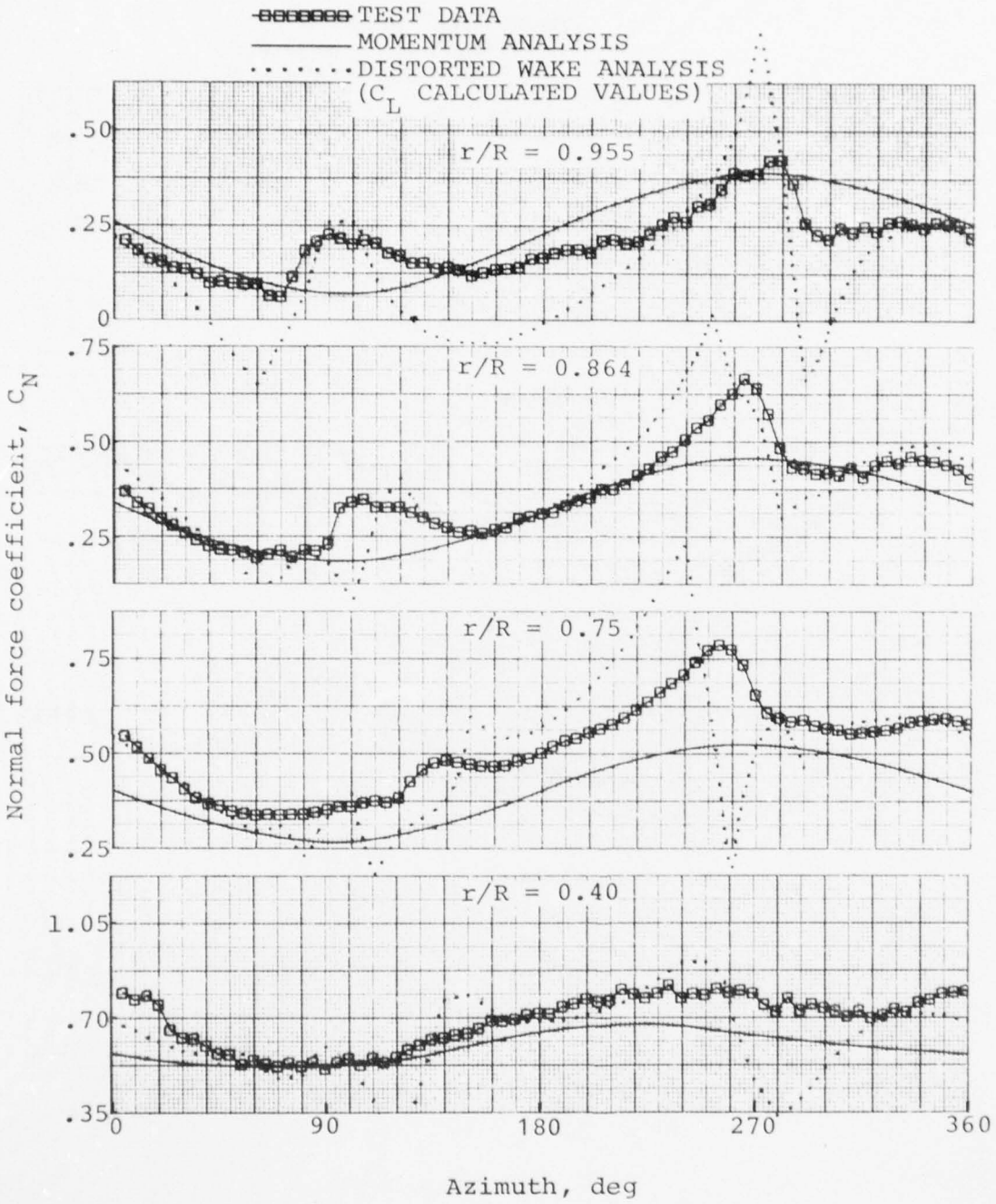

Figure 35. Comparison of measured and predicted normal force coefficients, record 728, 8100 pounds gross weight, forward flight at 50 knots.

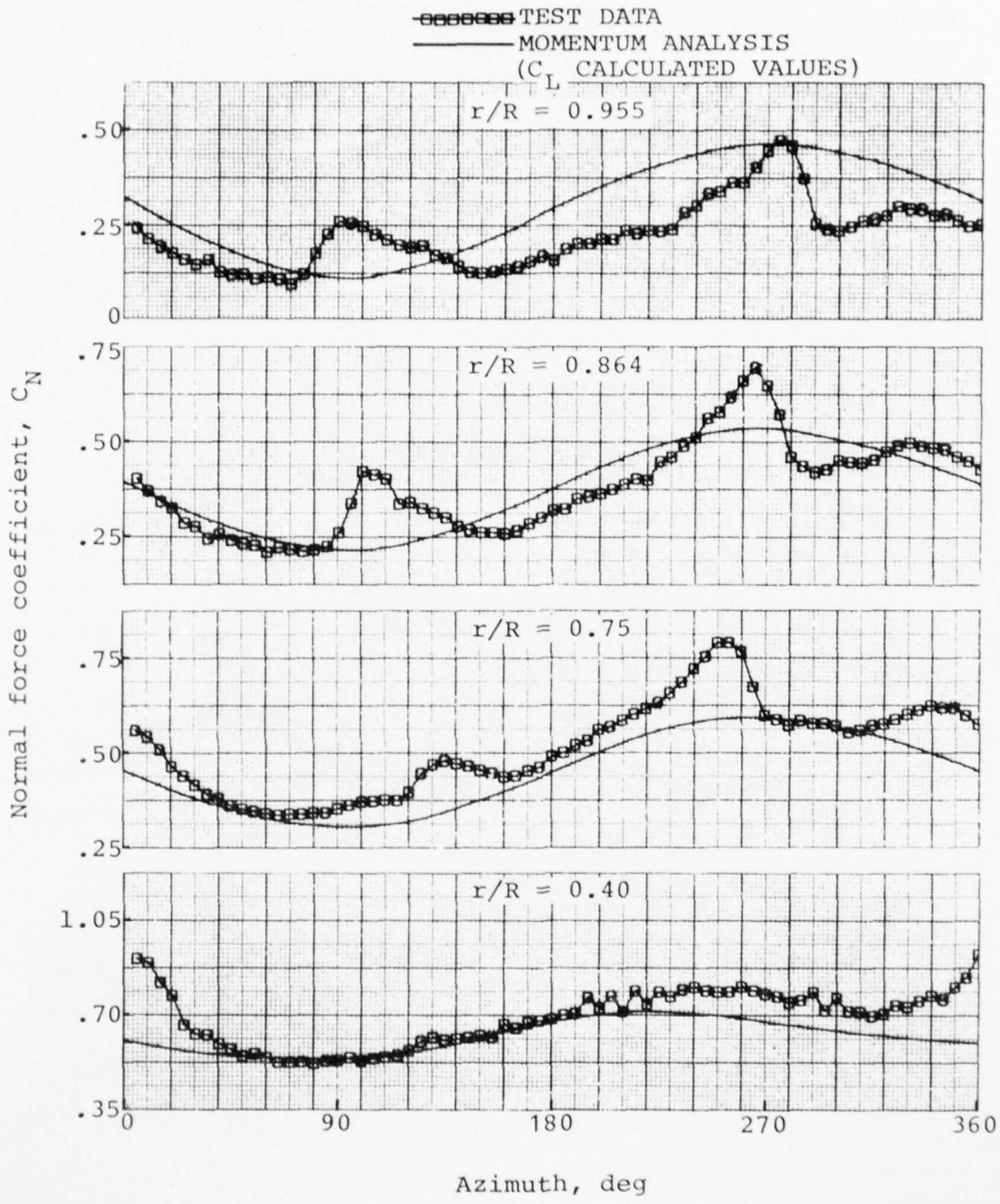

Figure 36. Comparison of measured and predicted normal force coefficients, record 690, 9000 pounds gross weight, forward flight at 50 knots.

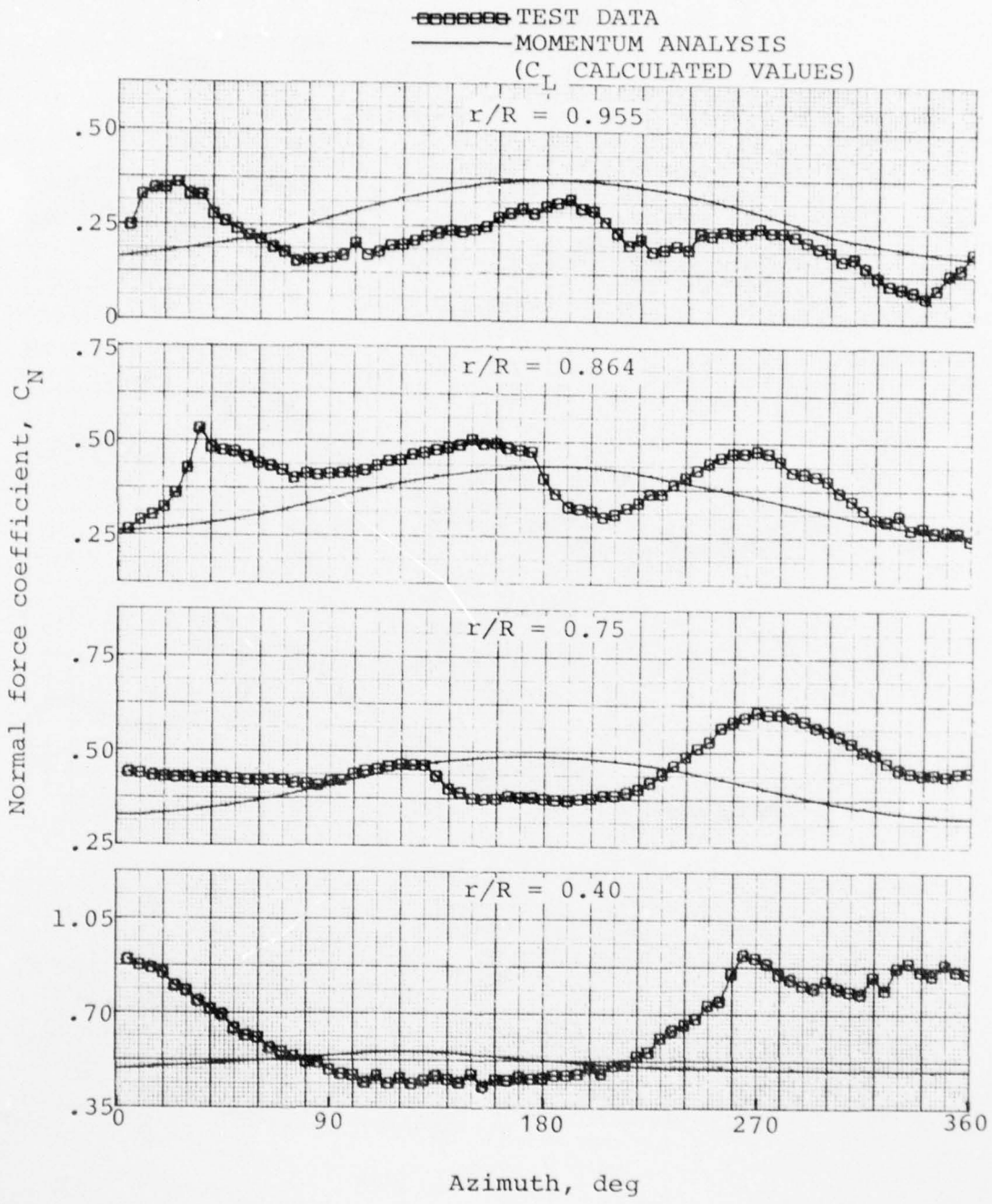

Figure 37. Comparison of measured and predicted normal force coefficients, record 717, 8100 pounds gross weight, right sideward flight at 30 knots.

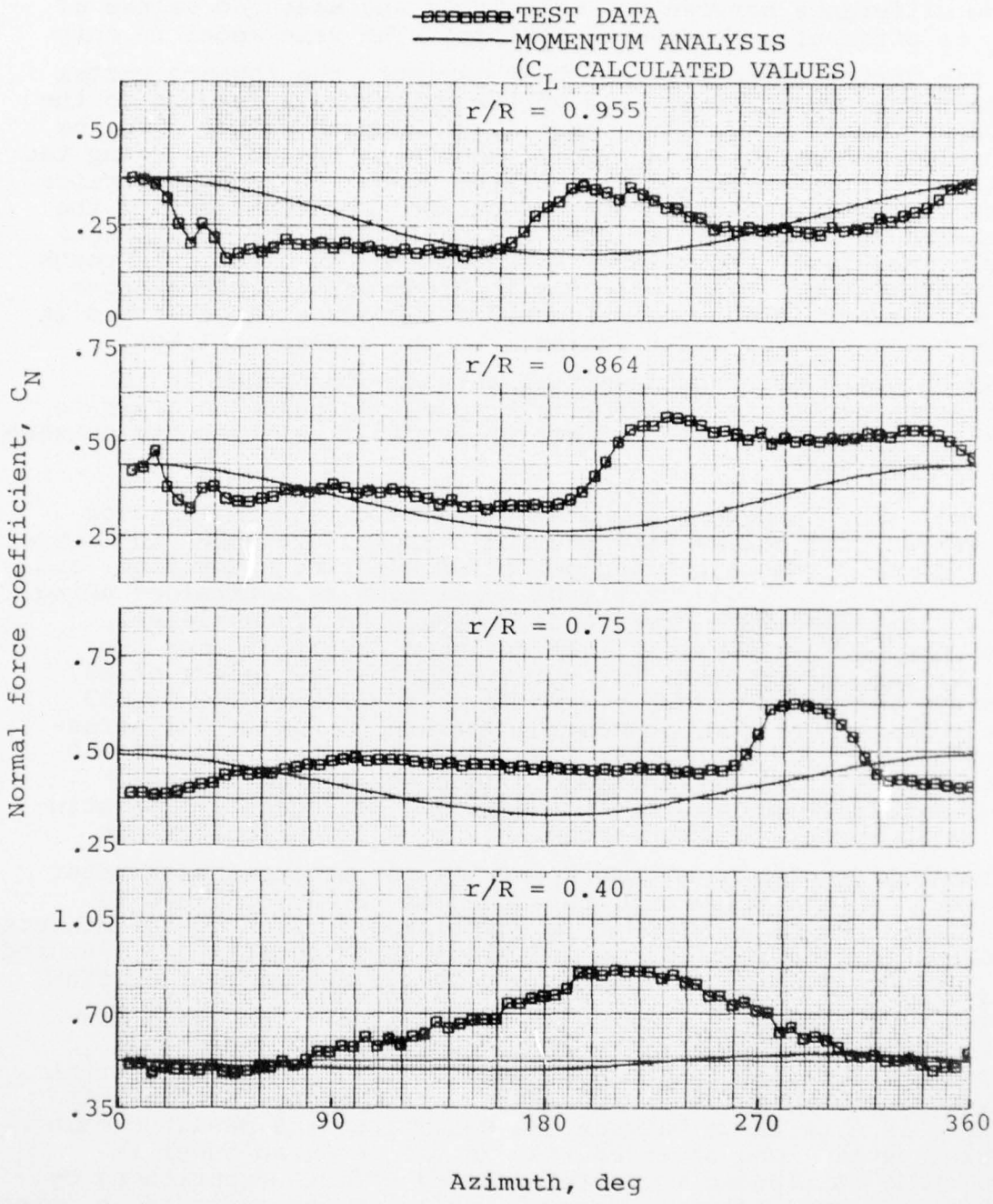

Figure 38. Comparison of measured and predicted normal force coefficients, record 720, 8100 pounds gross weight, left sideward flight at 30 knots.

The difference between the calculated and measured values of C_N is attributed to several factors. The wake model is only a tip vortex representation that neglects the inboard vortex sheet induced effects. The vortex strength is related to the overall blade circulation at a given azimuth rather than the local bound circulation. This results in the vortex being too strong on the advancing side of the disc. In addition, since the vortex strength is not an accurate approximation and the inboard sheet induced effects are neglected, the geometrical relationship of the wake with respect to the blade is a rough approximation. When dealing with blade/vortex interactions, small errors in this relationship can produce large errors in the calculated C_L distribution. In the low-speed flight region, more accurate numerical methods are needed in the free-wake analysis as the flight speed decreases in order to properly establish the correct geometrical relationship between blade and wake.

Comparisons between the measured and calculated main rotor power and collective pitch versus airspeed are shown in Figures 40 and 41. The calculated performance for both the 8100- and 9000-pound gross weight flight conditions as determined using the Prescribed Wake Hover Analysis and the blade-element, uniform inflow forward flight analysis (ARAM42). For the 8100-pound hover case, the measured main rotor power of 837 horsepower agrees closely with the calculated value of 833 horsepower. At 9000 pounds the measured power of 981 horsepower is noticeably higher than the calculated value of 930 horsepower. This flight record does not appear to be a completely stablized hover condition. Consequently, substantial asymmetry is associated with the C_N distribution and probably results in a discrepancy in the measured main rotor power. At the forward flight speed of 10, 20, 30, and 40 knots the calculated power is surprisingly close to the measured power, considering how the individually calculated and measured C_N versus azimuth distributions vary for several radial stations. The close agreement in power illustrates again how the blade element, uniform inflow analysis is capable of predicting net performance because of that theory's inherent averaging of details in the load distribution. At 50 knots there is a variance between the calculated and measured main rotor power. The observed rise in the measured power is possibly attributed to vortex-induced effects experienced by the retreating blade. Free-wake calculations indicate an interaction occurring as the blade approaches its own 1-1/4-revolution-old vortex at an azimuth of 220 degrees. The largely

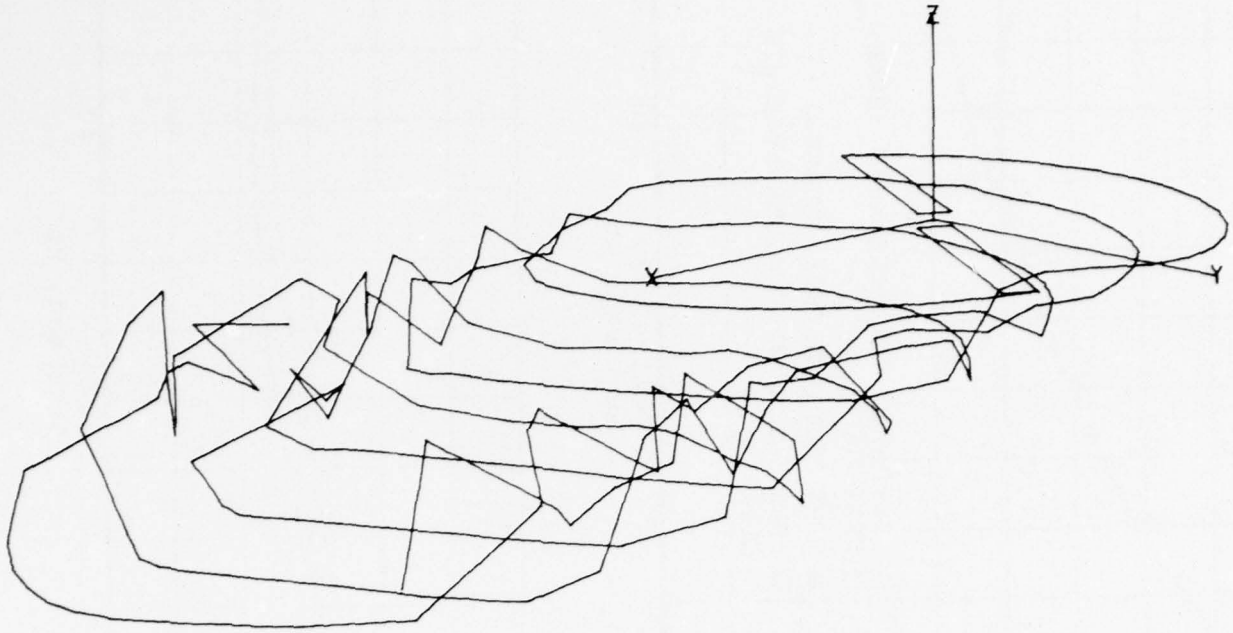

Figure 39. Calculated distorted wake at 50 knots.

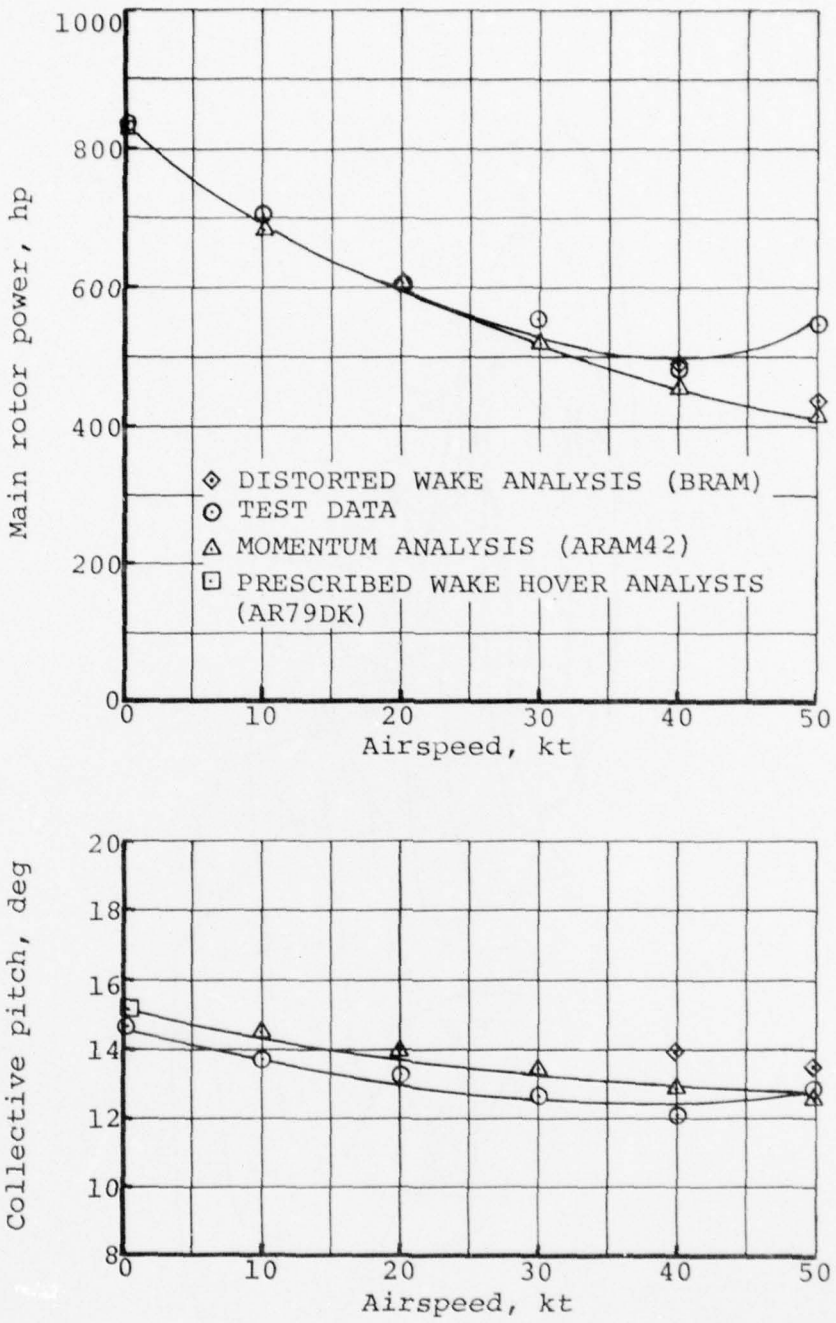

Figure 40. Comparison of measured and predicted main rotor power and collective pitch from 0 to 50 knots, 8100 pounds gross weight.

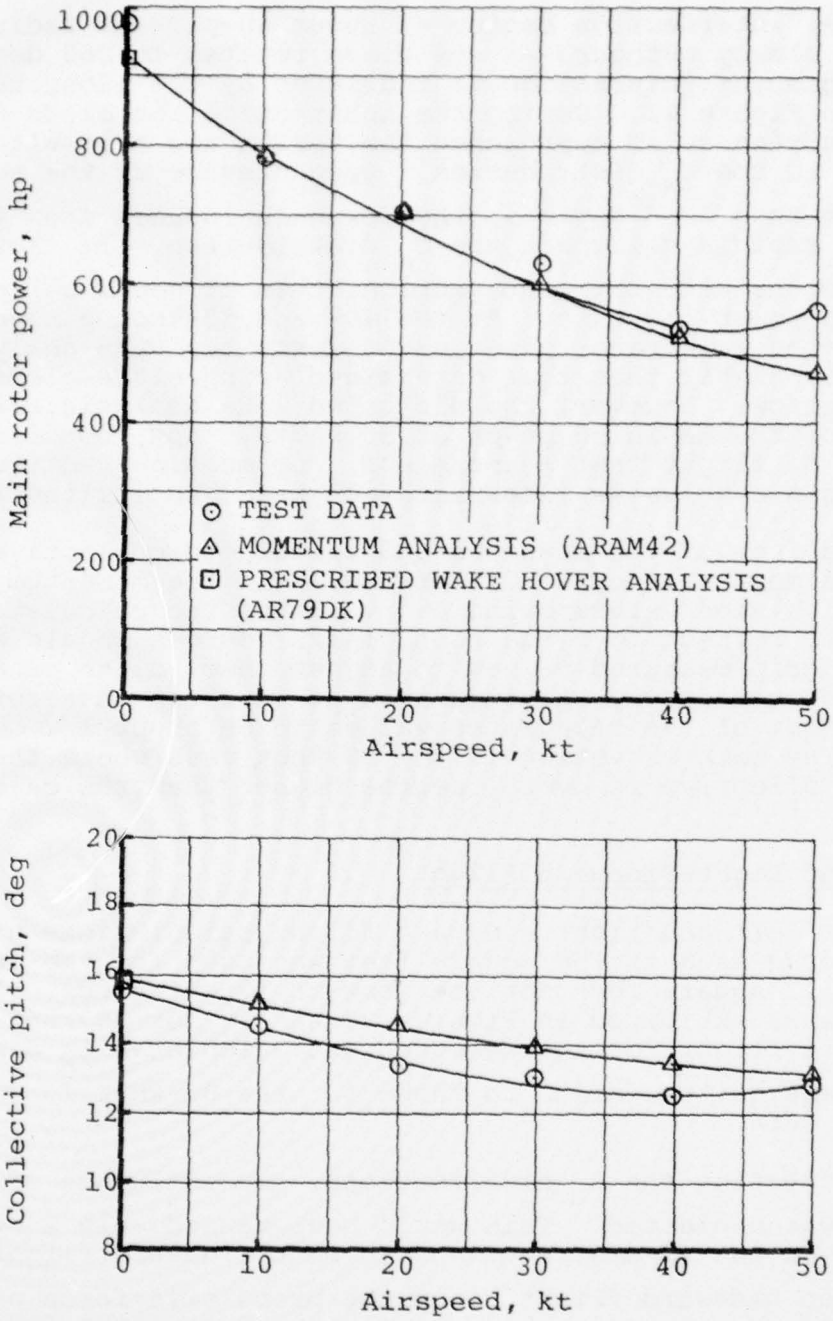

Figure 41. Comparison of measured and predicted main rotor power and collective pitch from 0 to 50 knots, 9000 pounds gross weight.

parallel intersection begins at about 40-percent radius and sweeps slowly outboard as the blade rotates to 260 degrees. The region of interaction is indicated by the elongated shaded area in Figure 42. During the interaction the blade experiences upwash as it approaches the vortex and a resultant increase in the C_N distribution. Upon passage of the vortex at an azimuth of 260 degrees, the downwash induced from the vortex rapidly collapses the C_N distribution. If flow separation occurs with this interaction, then it could be responsible for the power increase. At the 40- and 50-knot airspeeds, the calculated main rotor power using distorted wake analysis is slightly higher than that determined using blade-element, uniform inflow. However, the distorted wake analysis also falls short of the measured power at 50 knots. And, considering the nature of flight test measurement, one must be cautious of forming a conclusive interpretation based on limited test data.

A comparison of the measured and calculated collective pitch shows almost a 1-degree difference, with the momentum analysis calculated values being high. Since the calculated values are with respect to blade root, 1-1/2 degrees should be added to the grip-measured values to adjust them to the center of rotation reference. A comparison at this common reference shows most of the calculated values to be about 1/2-degree low. The main exception is the 50-knot case where the measured collective is over 1 degree higher than the calculated value.

Left and Right Sideward Flight

For the left and right sideward flight calculations a flat plate drag area of 150 square feet was used for the fuselage versus 12 square feet for the forward flight cases. In general, the trends exhibited in Figures 37 and 38 for 30-knot right sideward flight for the measured and calculated C_N distributions are quite similar to those for the 30-knot forward flight data.

In calculating the C_L distributions, the influence of the tail rotor was neglected. This would have caused only a small increase in the C_L distributions in left sideward flight relative to right sideward flight since the propulsive force of the main rotor would have to compensate for the opposing tail rotor thrust.

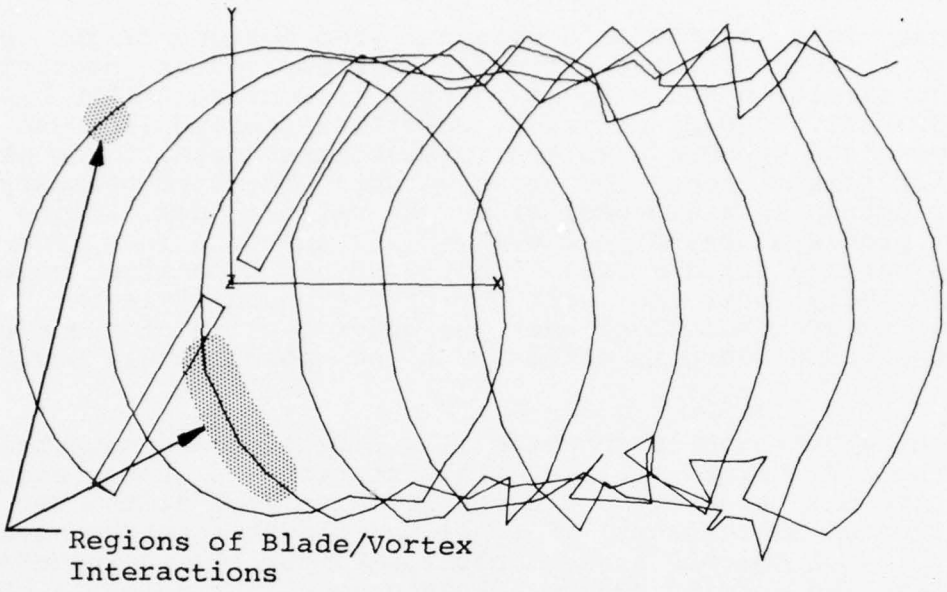

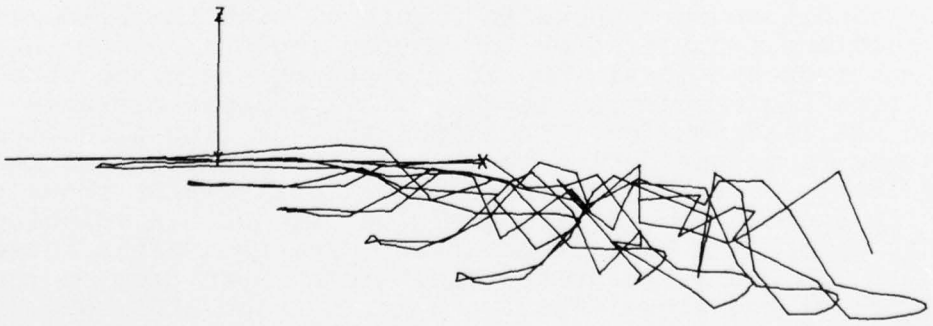

Figure 42. Distorted tip vortex geometry, 9000 pounds gross weight, forward flight at 50 knots.

Local Flow and Direction at 50 Knots

Boundary layer button data were analyzed for one flight condition to determine the influence of blade/vortex interactions on the direction and velocity of the flow close to the blade. The 50-knot, 9000-pound flight condition (record 690) was chosen since the blade/vortex interactions appear to be strongest for this airspeed and gross weight. The term boundary layer button is a misnomer since the vertical positioning of their probes at heights of 0.15, 0.25, and 0.35 inch from the blade surface for the 0.30, 0.60, 0.90 chord position gages, respectively, puts them well out of the boundary layer. The boundary layer thickness over the outer portion of the blade at 30-percent chord is estimated to be approximately 0.025 inch.

Figures 43 through 46 show the flow direction and magnitude for the $r/R = 0.864$ station. This station was chosen since it has only one inoperative BLB versus three each at the two adjoining radial stations. For all the flight records, about one-third of the BLB's were inoperative due to instrumentation problems and foreign debris. In Figure 43 the presence of two strong blade vortex interactions is indicated by the three lower surface BLBs. One of these interactions occurs on the advancing side at 130 degrees azimuth, while the other occurs on the retreating side at 300 degrees azimuth. Top and side views of the calculated distorted wake trajectory for this flight condition were shown in Figure 42 with the blade/vortex intersections identified by the shaded regions. Both intersections induce a local inboard flow along the blade with the deflection angle becoming larger with increased distance behind the leading edge. The upper surface flow direction measurements do not depict the vortex intersections as readily. The velocity data for the three lower surface BLBs shows a velocity excess over the front of the disc with a velocity deficit across the back of the disc. The two vortex intersections at 130 and 300 degrees result in a sharp drop in the magnitude of the flow. The two upper surface BLBs show similar trends. The magnitude of the velocity measured on the upper surface by the 0.6 and 0.9 chord BLBs is lower than that measured at the respective lower surface positions. This trend is opposite to that expected.

Further verification of the blade/vortex intersections is seen in the chordwise force coefficient and moment coefficient traces for this flight condition. These parameters are shown in Figures 47 and 48 for the four radial stations of 0.40, 0.75, 0.864, and 0.955.

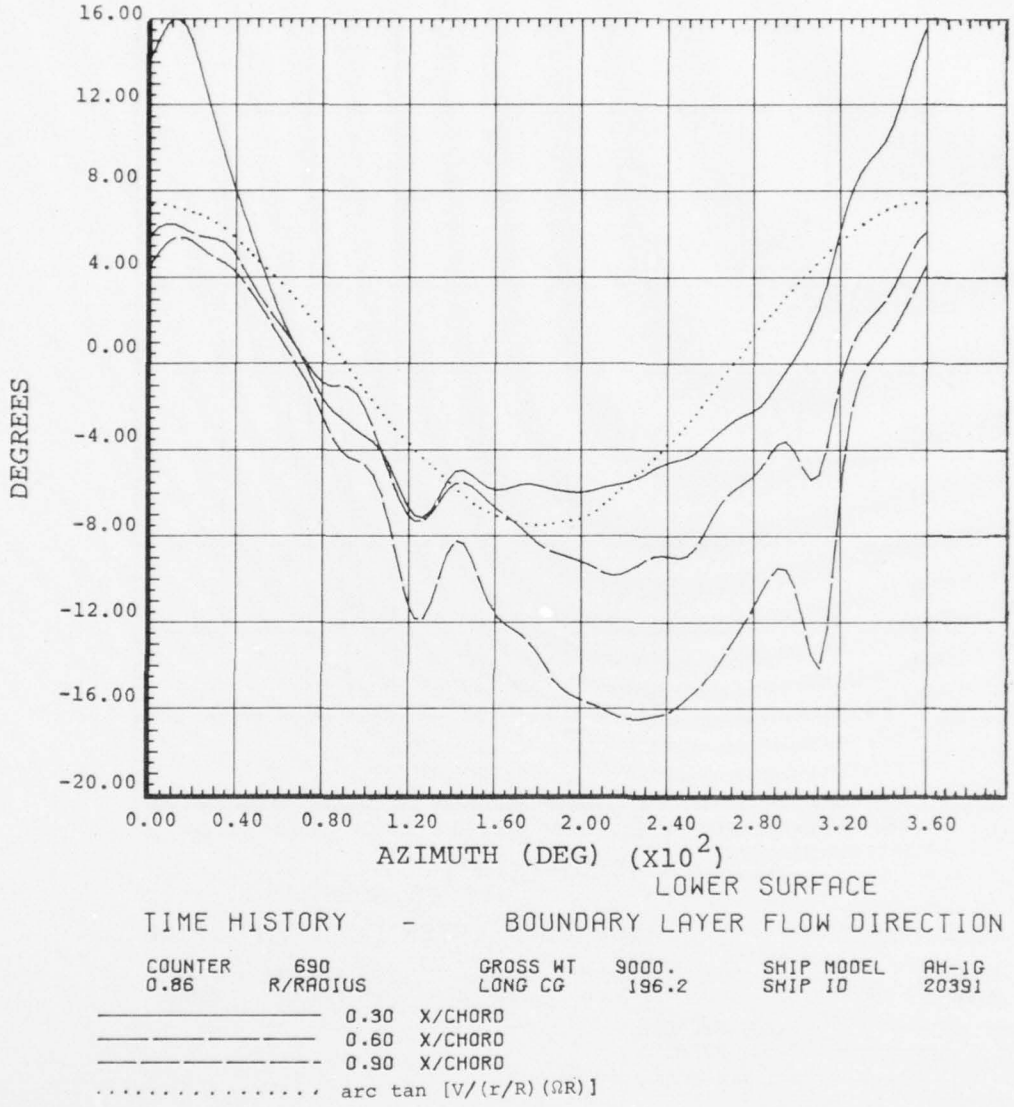

Figure 43. Lower surface flow direction measured at r/R=0.864, record 690, 9000 pounds gross weight, forward flight at 50 knots.

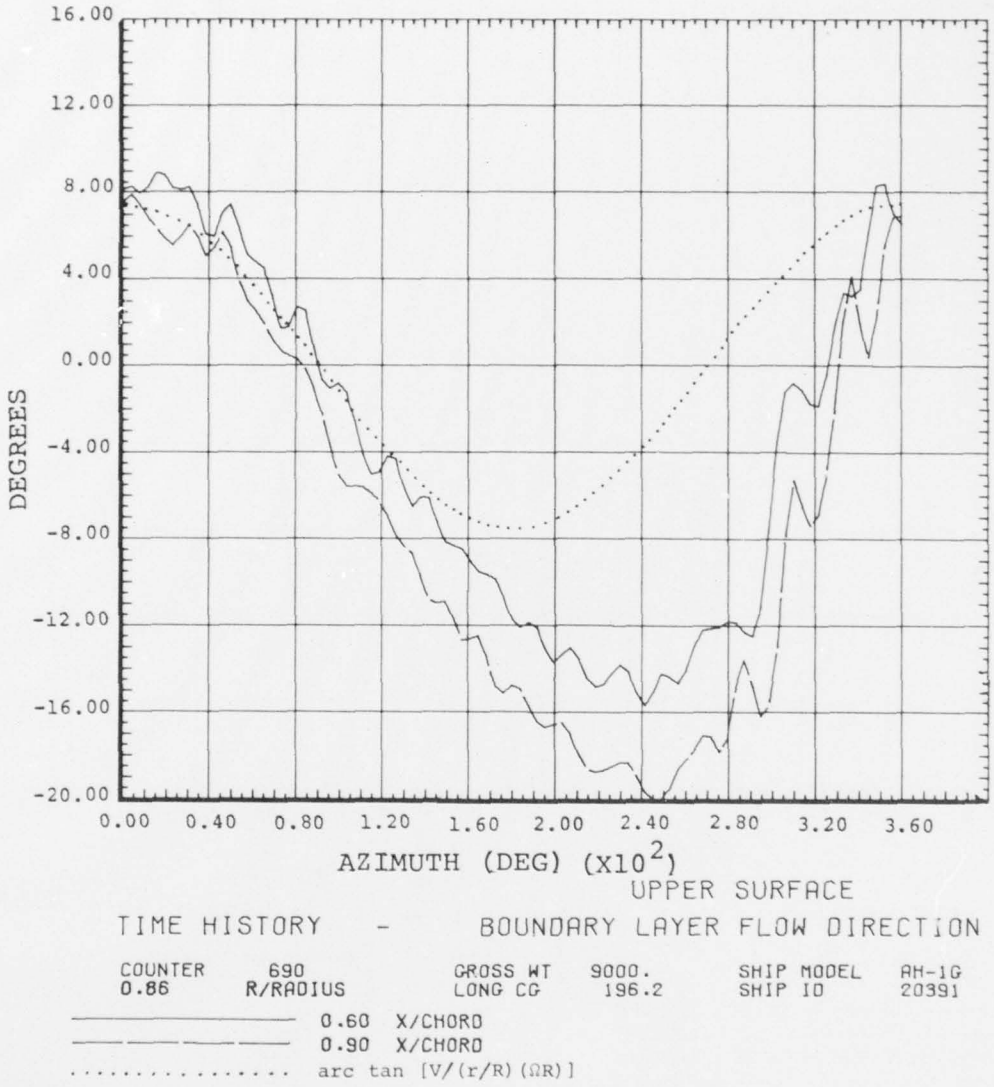

Figure 44. Upper surface flow direction measured at r/R=0.864, record 690, 9000 pounds gross weight, forward flight at 50 knots.

AD-A074 141 BELL HELICOPTER TEXTRON FORT WORTH TX F/G 1/3
ANALYSIS OF LOW-SPEED HELICOPTER FLIGHT TEST DATA.(U)
AUG 79 J L TANGLER DAAJ02-77-C-0022
UNCLASSIFIED BHT-699-099-103 USARTL-TR-79-19 NL

2 OF 2
AD A074141

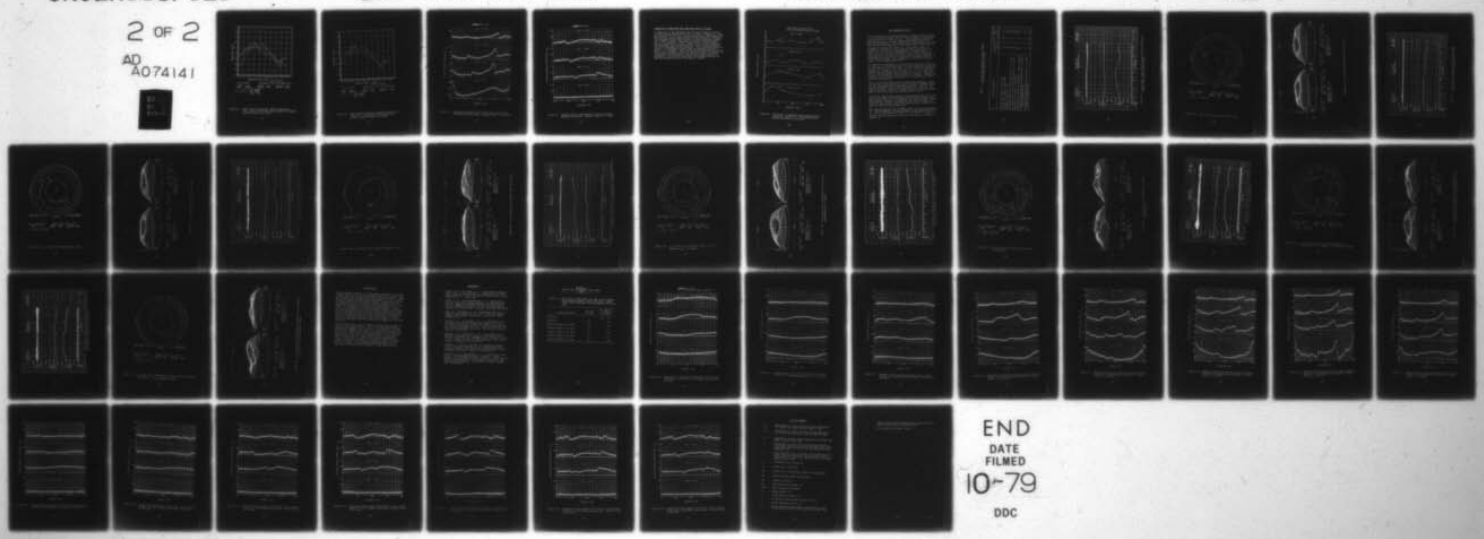

END
DATE FILMED
10-79
DDC

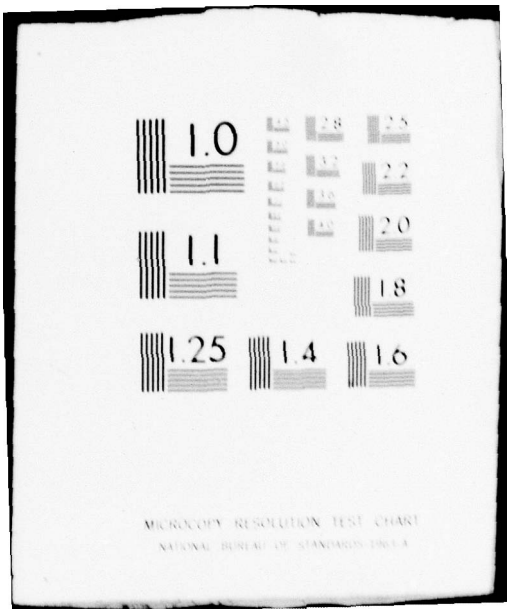
1.0
1.1
1.25
1.4
1.6
2.8
2.5
2.2
2.0
1.8
MICROCOPY RESOLUTION TEST CHART
NATIONAL BUREAU OF STANDARDS-1963-A

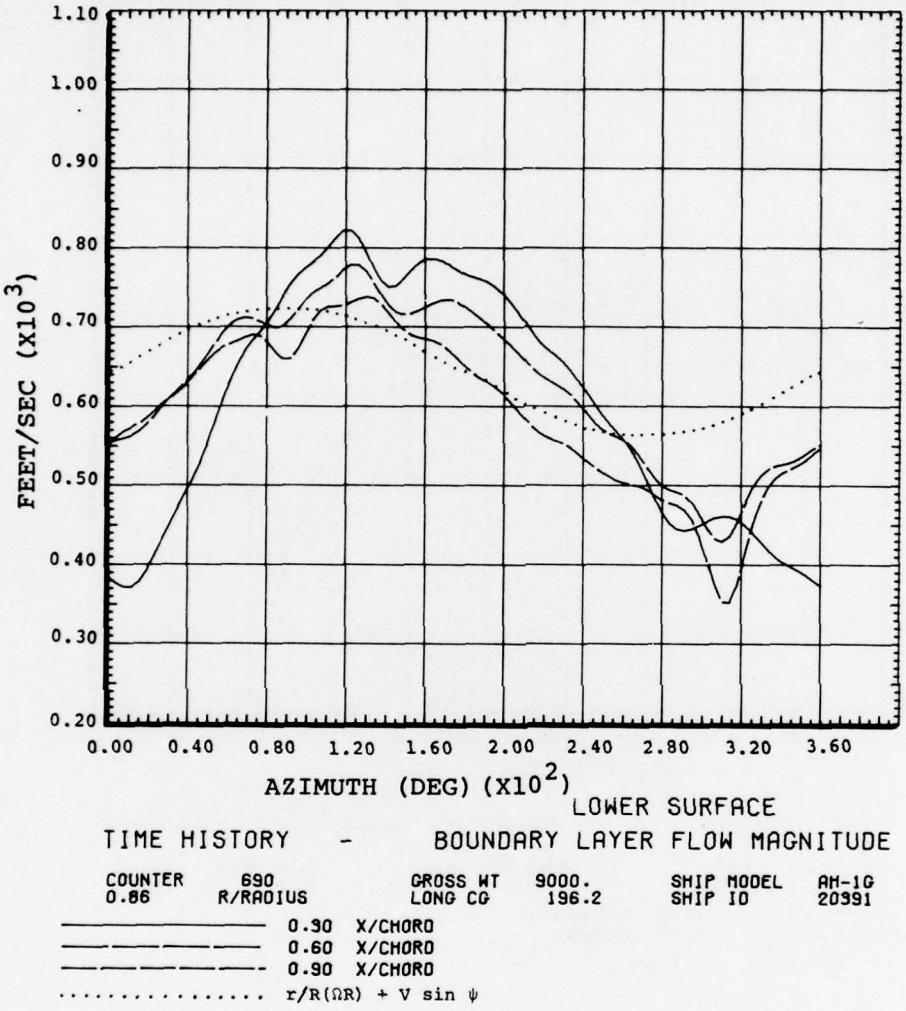

Figure 45. Lower surface resultant velocity measured at r/R = 0.864, record 690, 9000 pounds gross weight, forward flight at 50 knots.

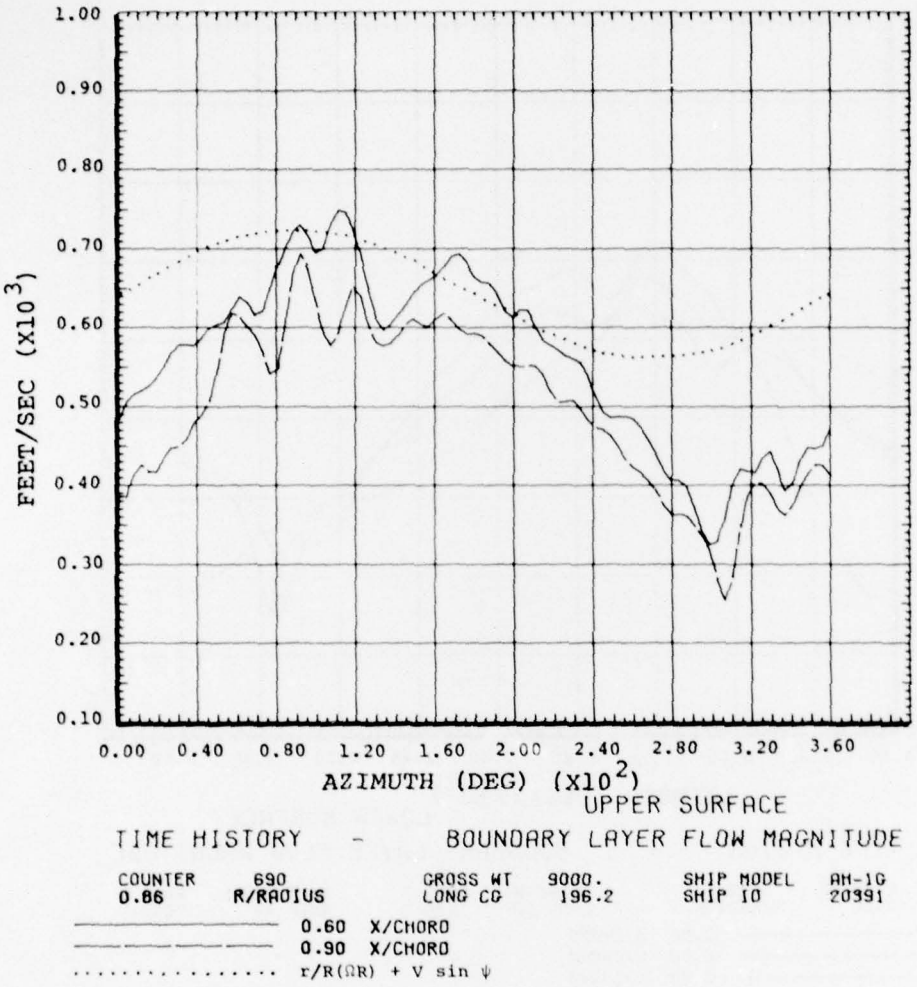

Figure 46. Upper surface resultant velocity measured at r/R=0.864, record 690, 9000 pounds gross weight, forward flight at 50 knots.

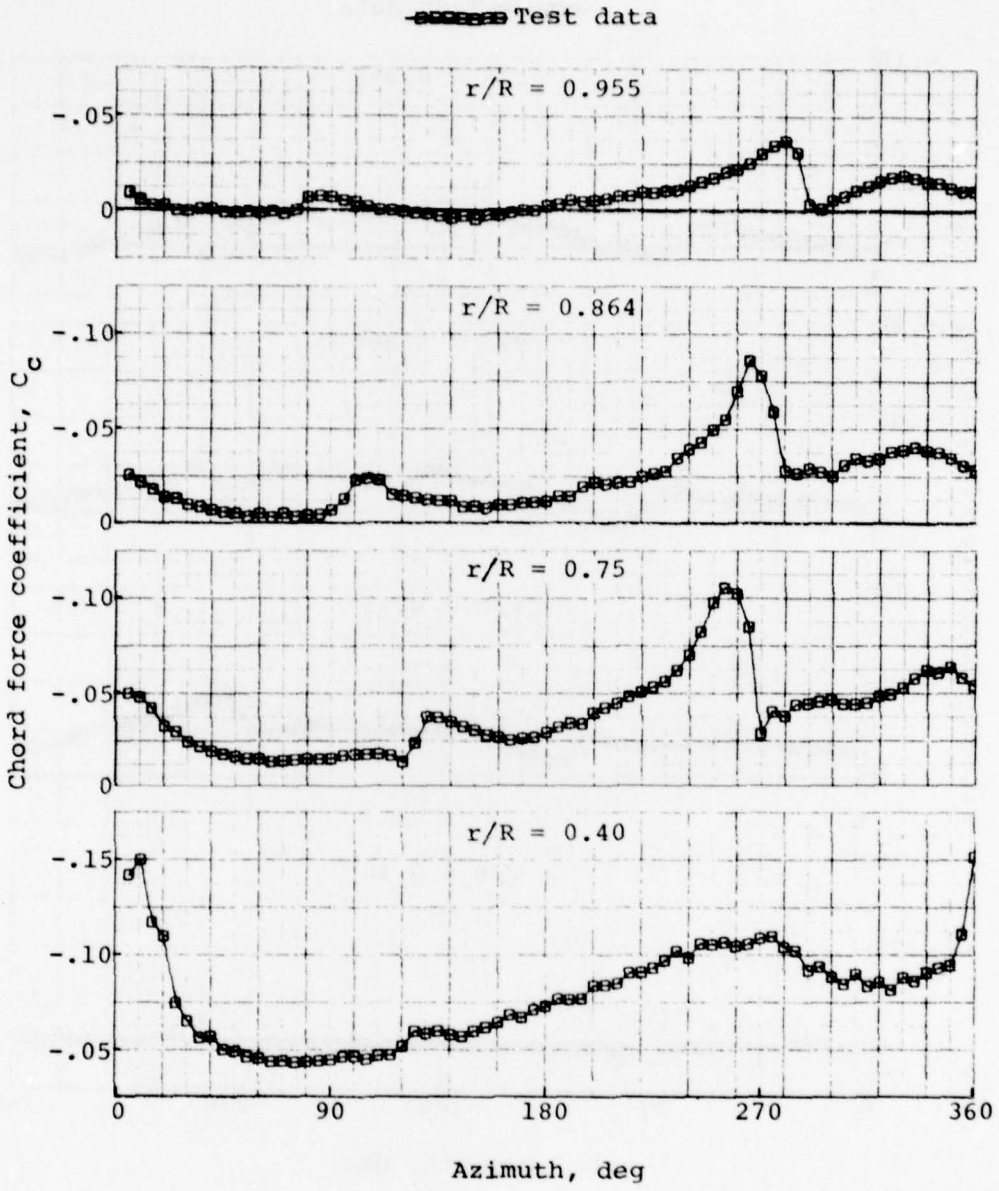

Figure 47. Measured chordwise force coefficient, record 690, 9000 pounds gross weight, forward flight at 50 knots.

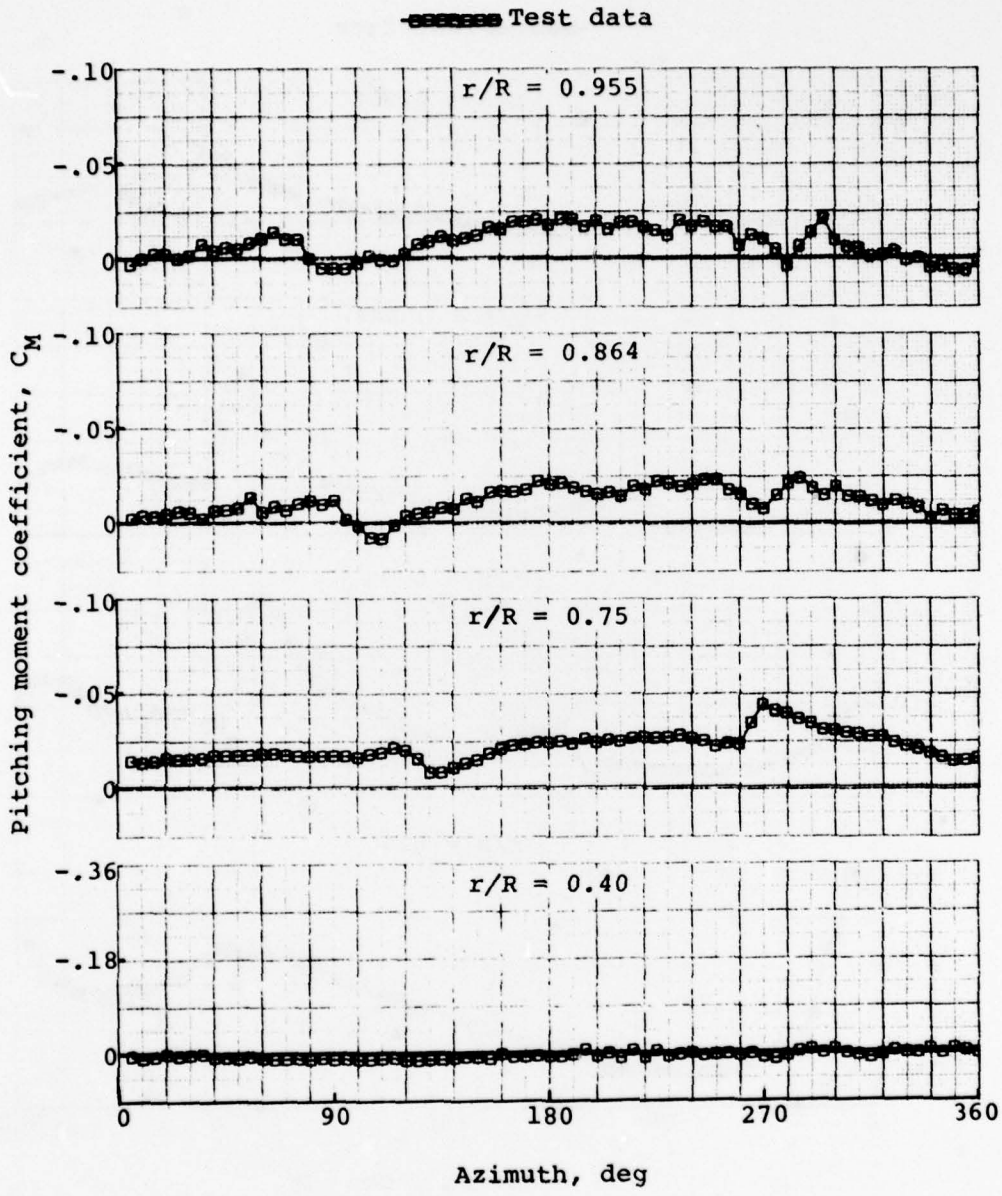

Figure 48. Measured moment coefficients, record 690, 9000 pounds gross weight, forward flight at 50 knots.

COMPARISON OF MEASURED AND PREDICTED ANGLE OF ATTACK

A comparison of the measured and calculated angle of attack for the 8100-pound OGE hover case is shown in Figure 49. Measured values for the four radial stations were determined from the hot-wire array stagnation point time histories. Knowing the stagnation point location and the associated Mach number for a radial station, the angle of attack is taken from a family of calculated curves. These curves were provided by the Government for the gloved AH-1G airfoil using the North Carolina State/NASA airfoil program. The calculated angle of attack is consistently higher than the measured values by about 1 to 2 degrees. The accuracy associated with the curves that relate stagnation point to angle of attack is unknown. A two-dimensional wind-tunnel test of the gloved airfoil is necessary to verify the calculated relationship between the measured stagnation point and angle of attack.

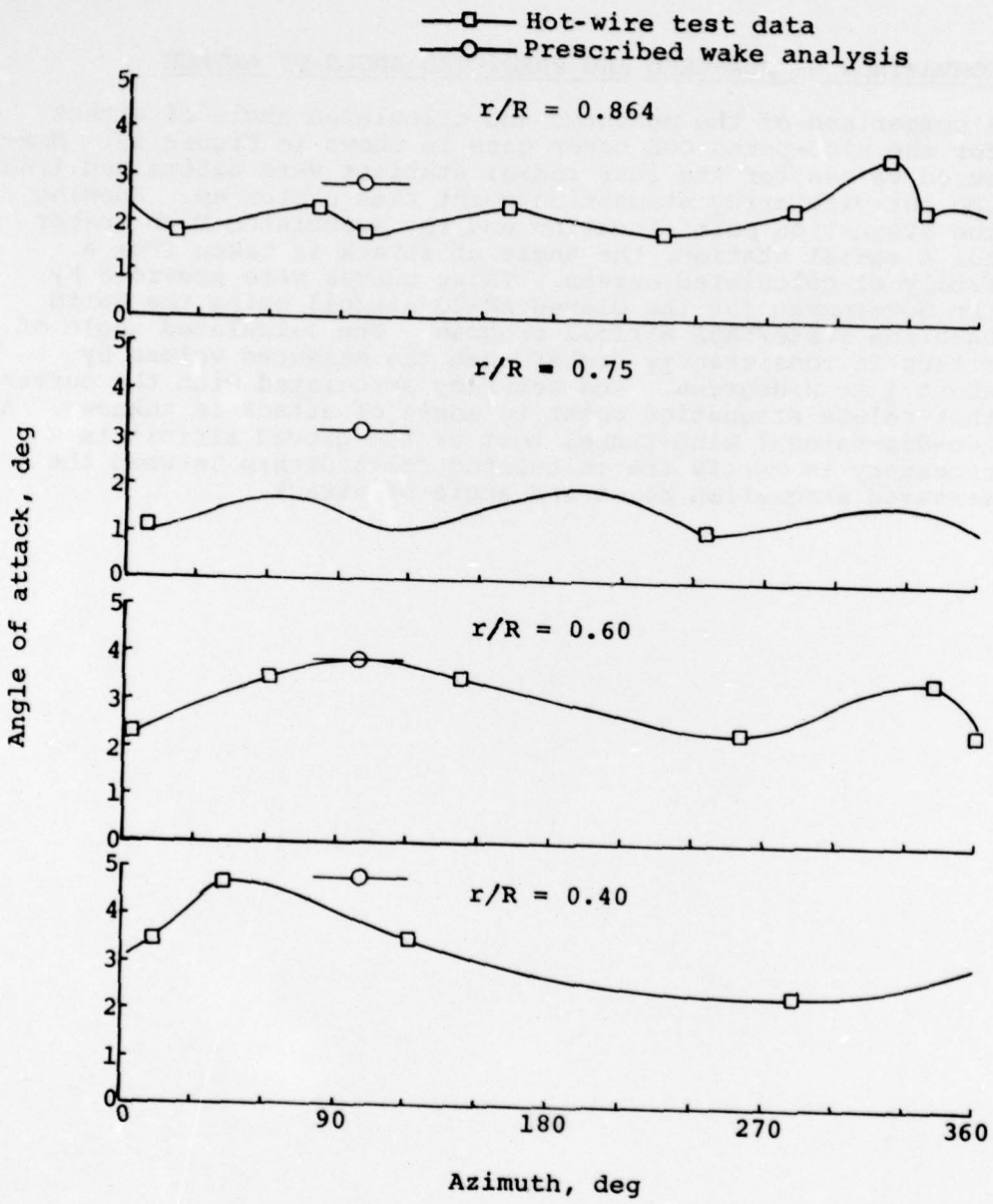

Figure 49. Comparison of measured and calculated angle of attack, record #723, 8100 pounds gross weight, OGE hover at 100 feet.

NOE MANEUVER FLIGHTS

Data was reduced for the NOE maneuver flights listed in Table 5. All of these flights are at a gross weight of 8100 pounds and altitudes of 50 and 100 feet. The maneuvers listed are considered typical of those encountered during NOE flight. The data presented in this section gives some insight into the distribution and magnitude of the peak values of C_N that can be expected during the maneuvers. These peak values are assumed to coincide with the maximum excursions of the aircraft's cg load factor as measured by an accelerometer. A time history of the cg load factor, cyclic and collective stick positions is shown for each flight record. Although an airspeed time history was also desired, the speed range in which these maneuvers were conducted was outside the usable range of the airspeed indicator.

For some of the maneuvers, no significant excursion from the 1g load factor was experienced, as seen in Figures 50 through 57 (records 722, 743, 742, 744). For the remaining maneuvers, Figures 58 through 67 (records 746, 729, 745, 718, and 721), maximum cg load factors in the range of 1.5 to 1.7 were measured. The triangular symbol along the time axis indicates the point at which the cg load factor is largest. Contour and surface plots of the C_N distribution are presented for this point in the maneuver.

The IGE to OGE and NOE flight to OGE pop-up maneuver contour and surface plots (Figures 51 and 53) closely resemble those for the 8100-pound hover condition (Figures 9 and 10). With respect to hover, only subtle differences are seen for the pop-up maneuvers, such as a slight increase in both the magnitude of the C_N distribution and collective pitch.

The contour and surface plots for the descent from OGE to IGE (Figure 55) show a less symmetrical distribution than hover. This results from the rotor passing into its own wake. Other side effects include an increase in the overall vibration level as seen in the load factor and an erratic control stick position time history (Figure 54).

The load factors for the 90 degree right turn and acceleration to 70 knots maneuver (Figure 56) show little deviation from 1g. The C_N distribution (Figure 57) is shown at a point 10.5 seconds into the maneuver where the load factor is approximately 1.1.

TABLE 5. FLIGHT CONDITIONS AND RECORD NUMBERS FOR THE NOE MANEUVER FLIGHTS

Flight Conditions	Altitude (feet)	GW = 8100 LB C.G. (Mid) Flt/Record
Pop-up IGE Hover to OGE Hover	50	37D 722
Pop-up NOE Flight to OGE Hover	50	743
Descent from OGE to IGE	50	742
90-Degree Right Turn and Acceleration to 70 KIAS	50	744
90-Degree Left Turn and Acceleration to 70 KIAS	50	746
Decelerate 50 Knots to OGE Hover	100	729
Decelerate 50 Knots to OGE Hover - Level Attitude	100	745
Directional Reversal and Acceleration to 30 KIAS Left Sideward Flight	50	718
Directional Reversal and Acceleration to 30 KIAS Right Sideward Flight	50	721

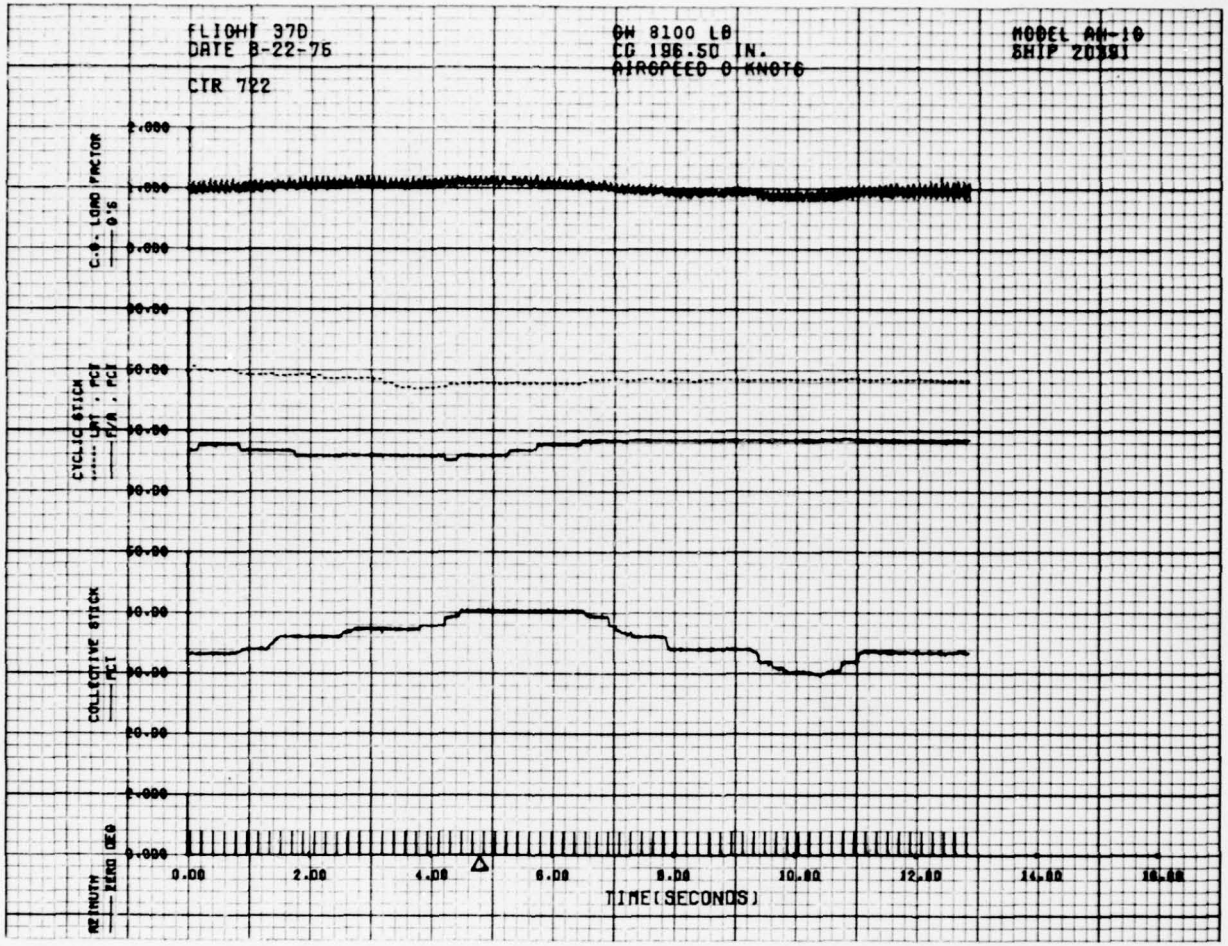

Figure 50. Load factor, cyclic and collective stick positions versus time (pop-up IGE to OGE).

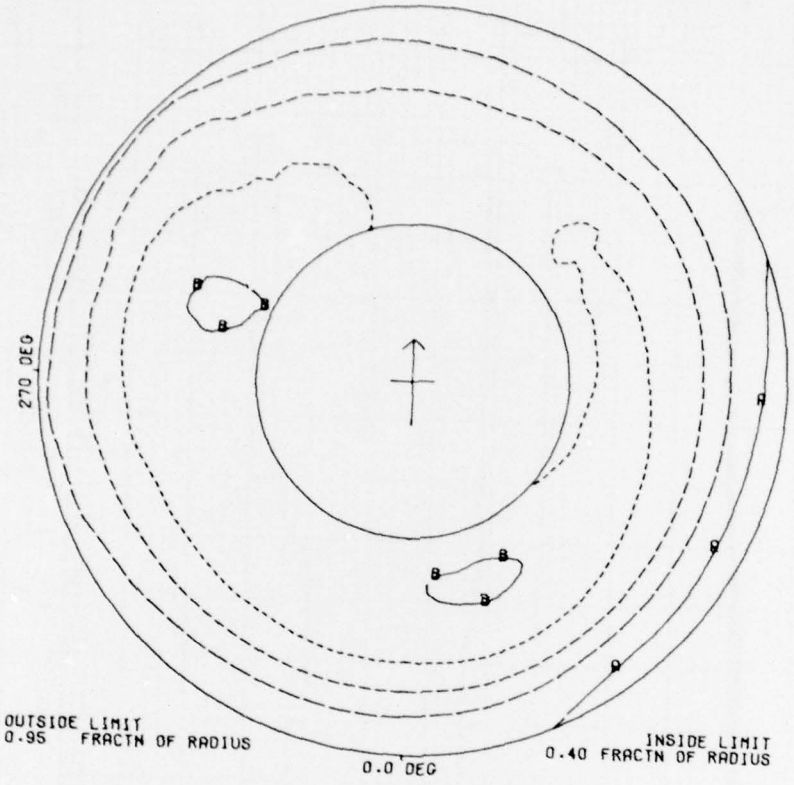

DERIVED PARAMETER - NORMAL FORCE COEFFICIENT

COUNTER 722

GROSS WT 8100. SHIP MODEL AH-1G
LONG CG 196.5 SHIP ID 20391

A 0.3 CN
B 0.7 CN

Figure 51A. C_N contour plot (pop-up IGE to OGE).

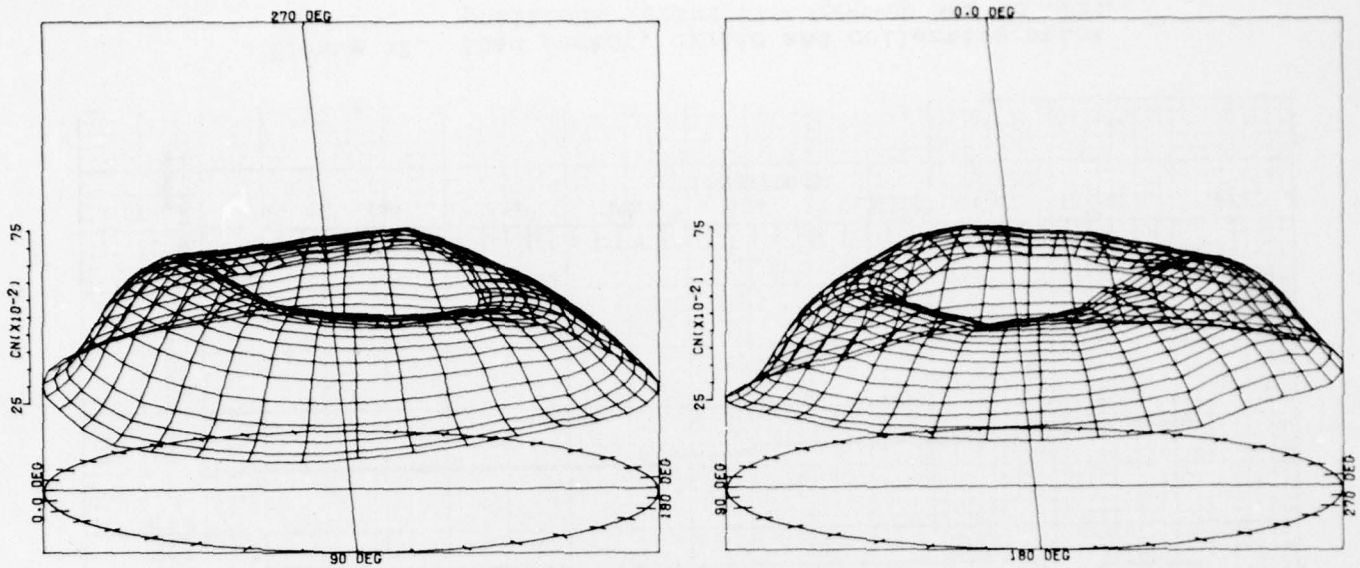

DERIVED PARAMETER - NORMAL FORCE COEFFICIENT

COUNTER 722 GROSS WT 8100 SHIP MODEL AH-1G
LONG CG 196.5 SHIP ID 20391

ANGULAR INCREMENT 10 DEG
RADIAL QUANTITY FRACTN OF RADIUS
MAX RADIUS 0.955
RADIAL INCREMENT 0.0370

DERIVED PARAMETER - NORMAL FORCE COEFFICIENT

COUNTER 722 GROSS WT 8100 SHIP MODEL AH-1G
LONG CG 196.5 SHIP ID 20391

ANGULAR INCREMENT 10 DEG
RADIAL QUANTITY FRACTN OF RADIUS
MAX RADIUS 0.955
RADIAL INCREMENT 0.0370

Figure 51B. C_N surface plots (pop-up IGE to OGE).

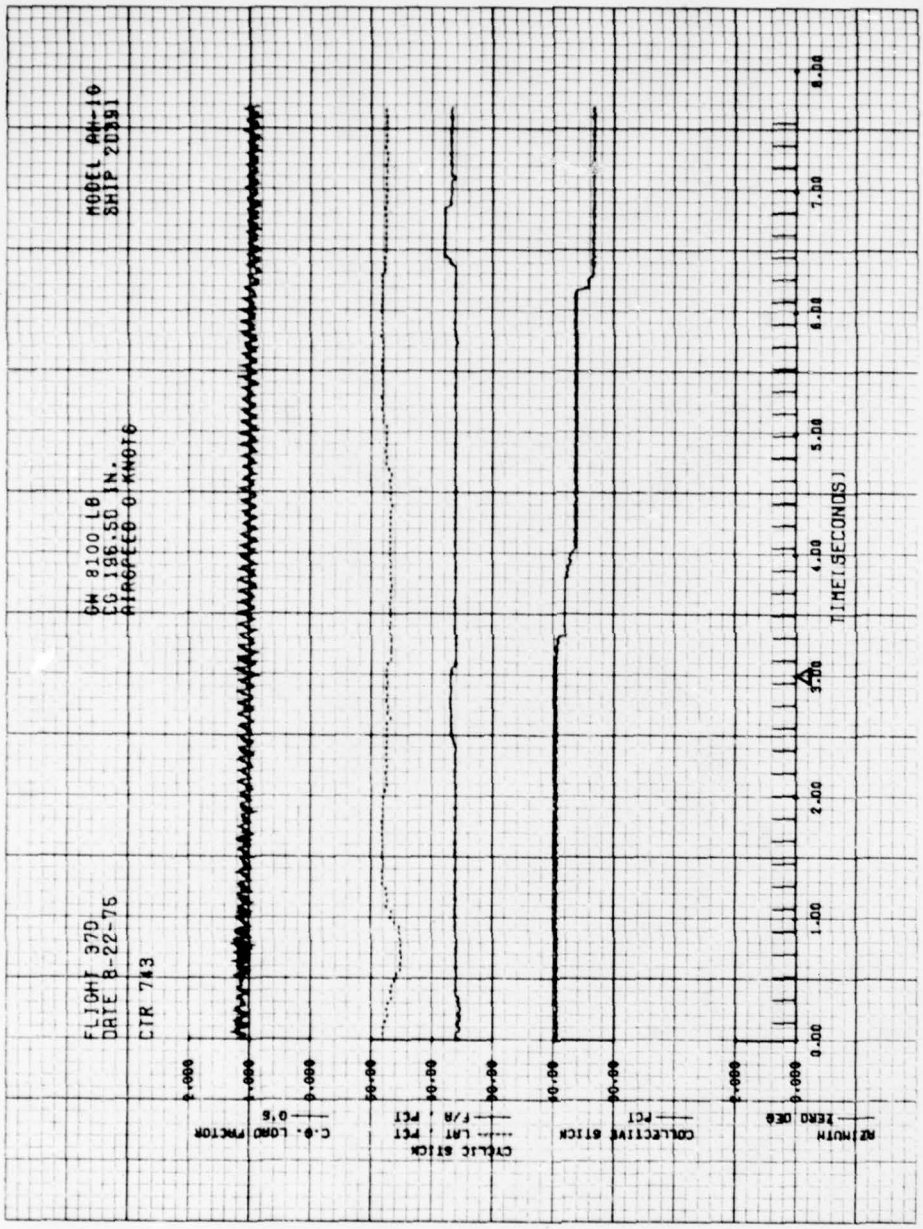

Figure 52. Load factor, cyclic and collective stick positions versus time (pop-up NOE to OGE).

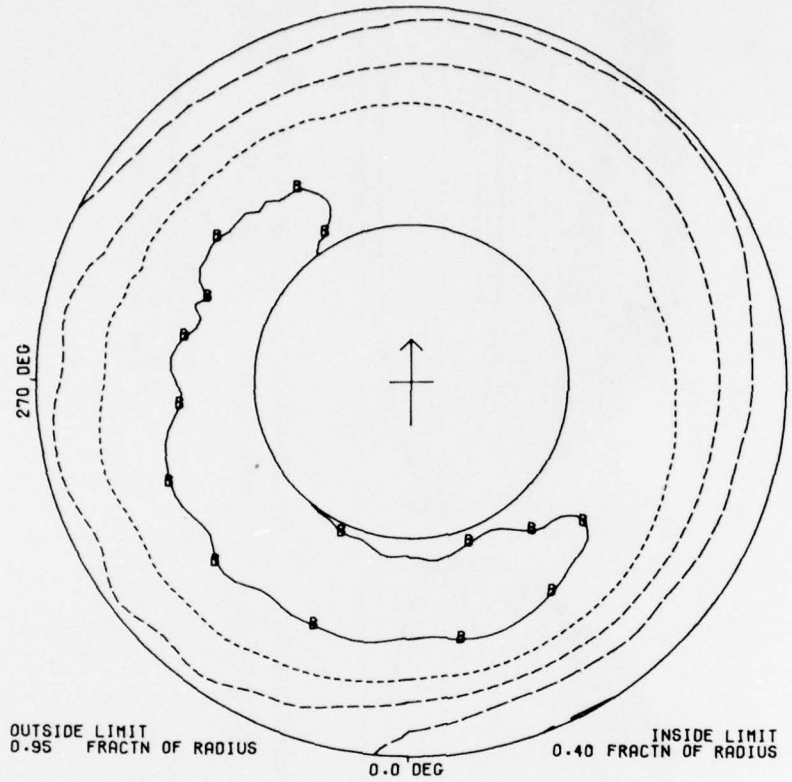

DERIVED PARAMETER - NORMAL FORCE COEFFICIENT

COUNTER 743

GROSS WT 8100. SHIP MODEL AH-1G
LONG CG 196.5 SHIP ID 20391

A 0.2 CN
B 0.6 CN

Figure 53A. C_N contour plot (pop-up NOE to OGE).

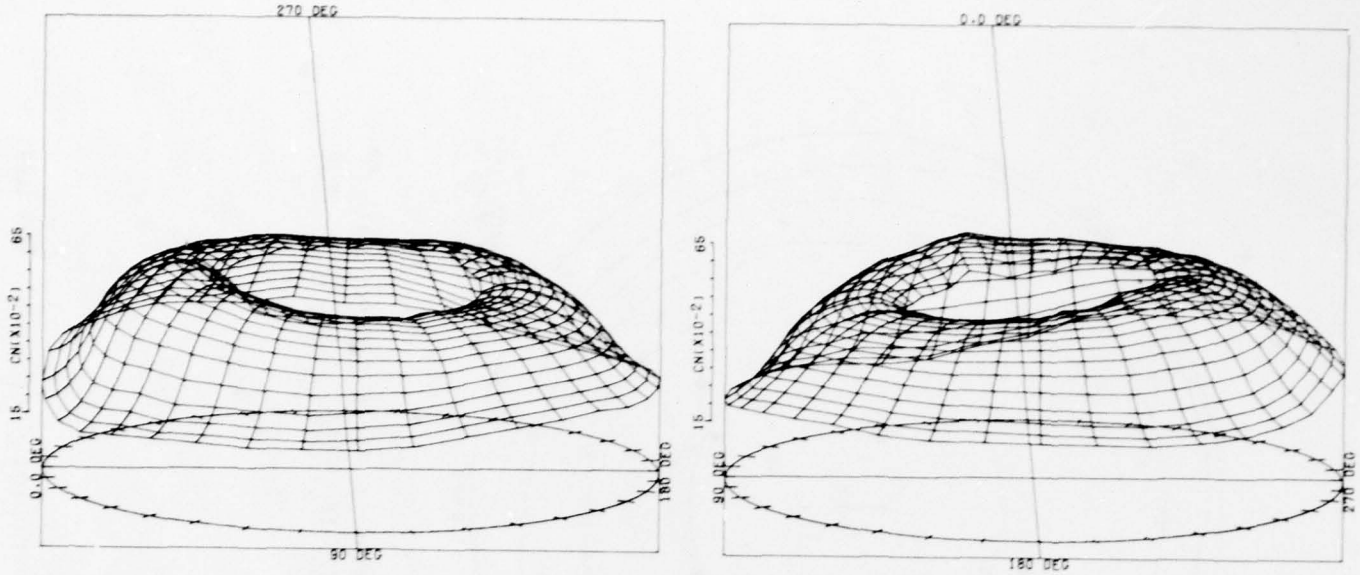

Figure 53B. C_N surface plots (pop-up NOE to OGE).

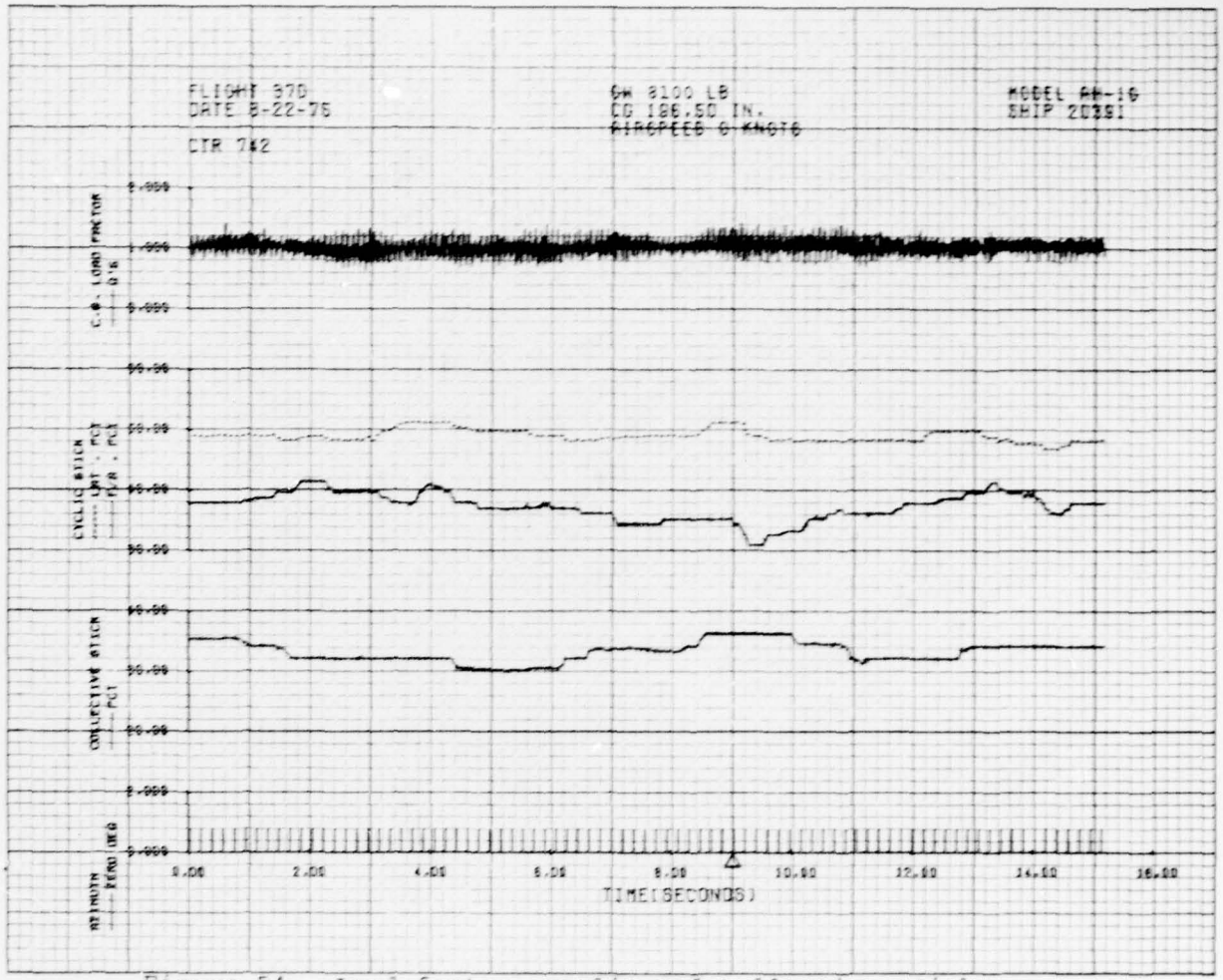

Figure 54. Load factor, cyclic and collective stick position versus time (descent from OGE to IGE).

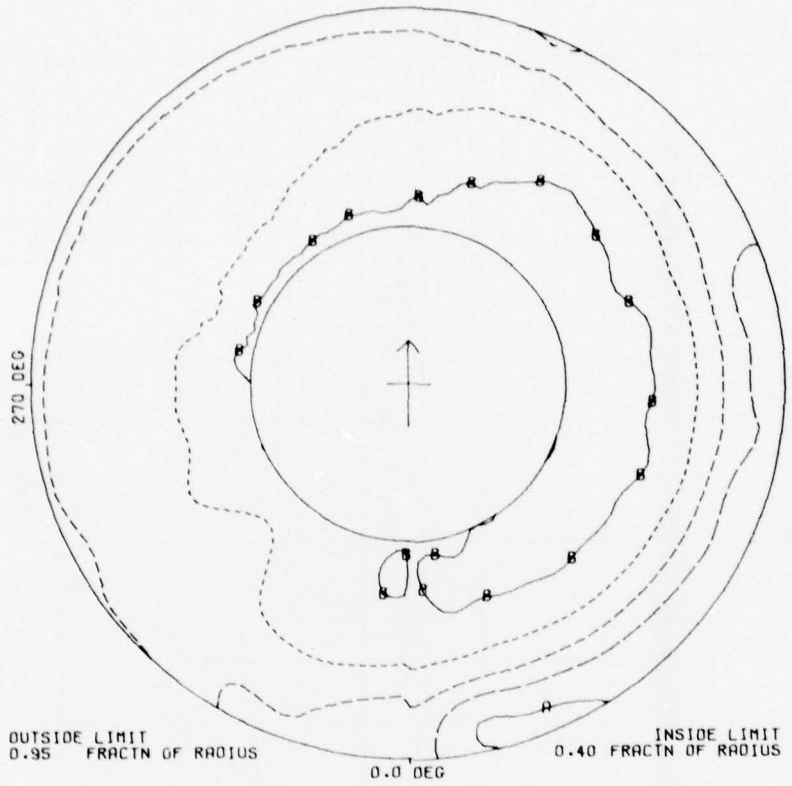

DERIVED PARAMETER - NORMAL FORCE COEFFICIENT

COUNTER 742

GROSS WT 8100 SHIP MODEL AH-1G
LONG CG 196.5 SHIP ID 20391

A 0.2 CN
B 0.6 CN

Figure 55A. C_N contour plot (descent from OGE to IGE).

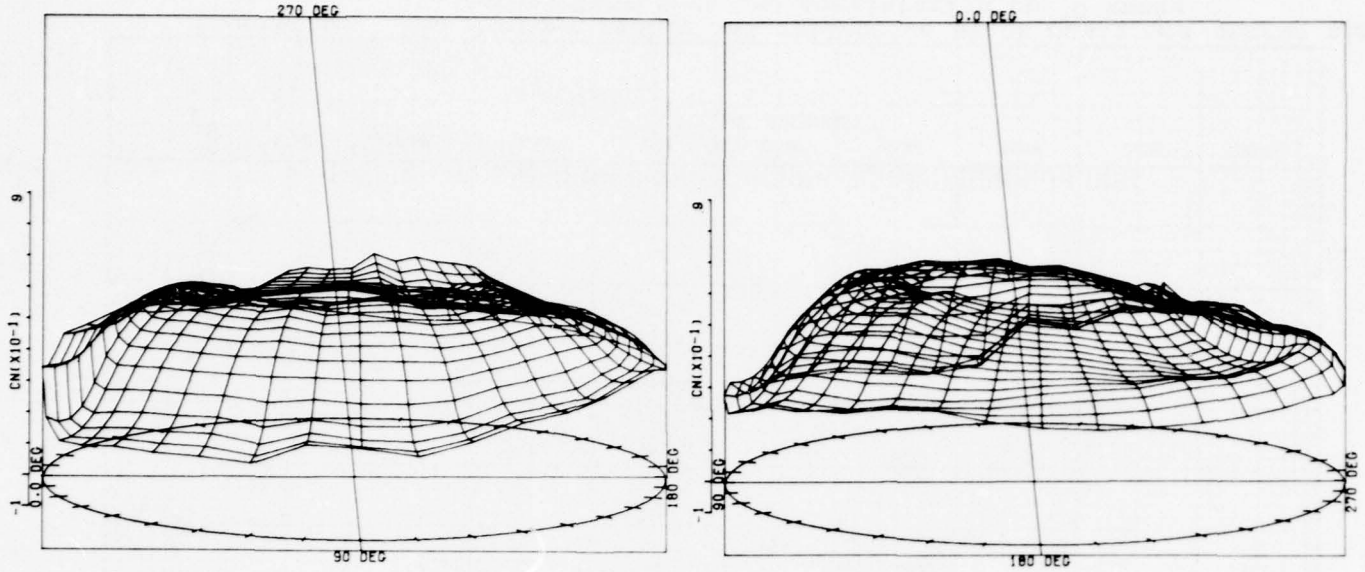

DERIVED PARAMETER - NORMAL FORCE COEFFICIENT

COUNTER 742 GROSS WT 8100 SHIP MODEL AH-1G
LONG CG 196.5 SHIP ID 20391

ANGULAR INCREMENT 10 DEG
RADIAL QUANTITY FRACTN OF RADIUS
MAX RADIUS 0.955
RADIAL INCREMENT 0.0370

DERIVED PARAMETER - NORMAL FORCE COEFFICIENT

COUNTER 742 GROSS WT 8100 SHIP MODEL AH-1G
LONG CG 196.5 SHIP ID 20391

ANGULAR INCREMENT 10 DEG
RADIAL QUANTITY FRACTN OF RADIUS
MAX RADIUS 0.955
RADIAL INCREMENT 0.0370

Figure 55B. C_N surface plots (descent from OGE to IGE).

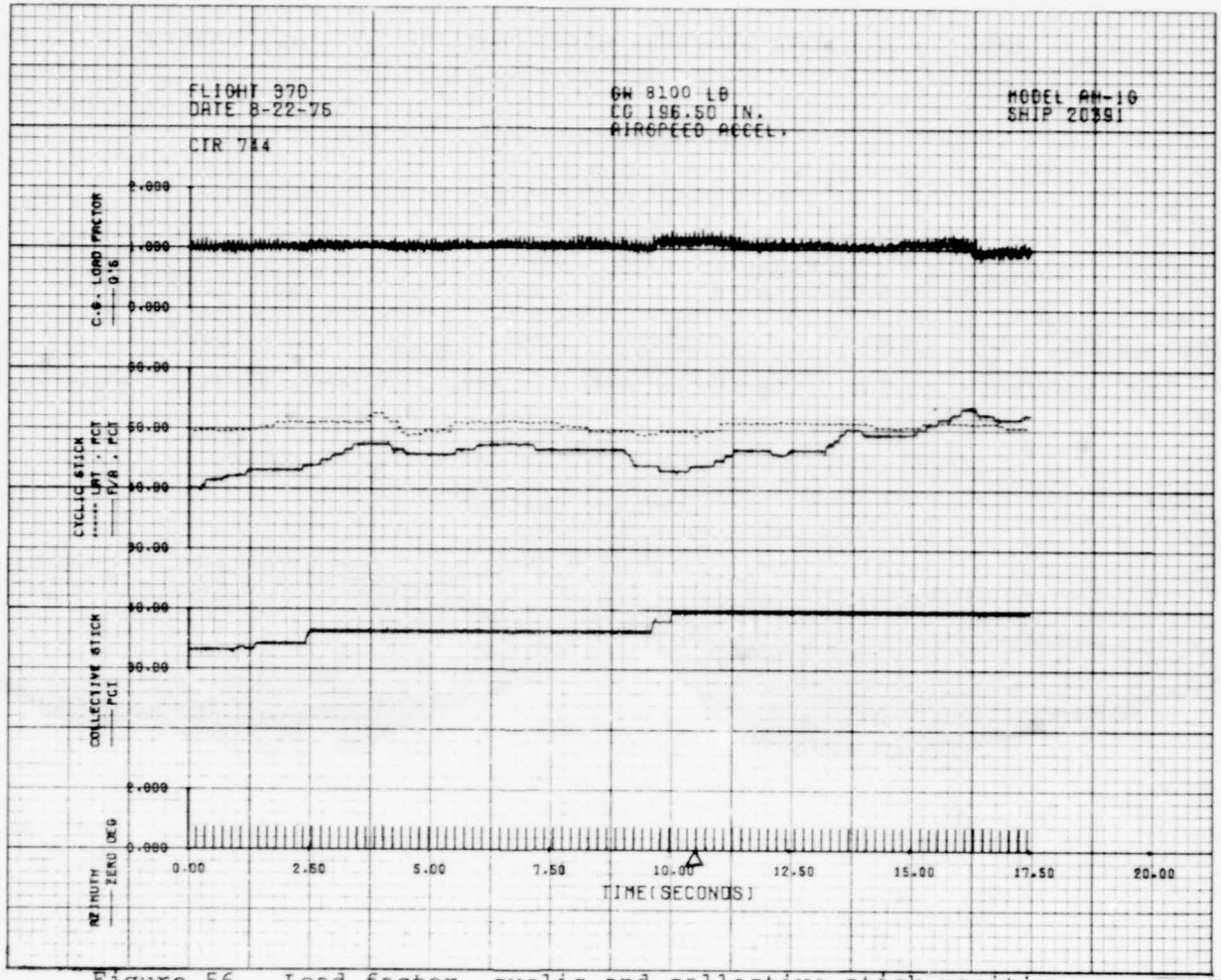

Figure 56. Load factor, cyclic and collective stick positions versus time (90-degree right turn and acceleration to 70 knots).

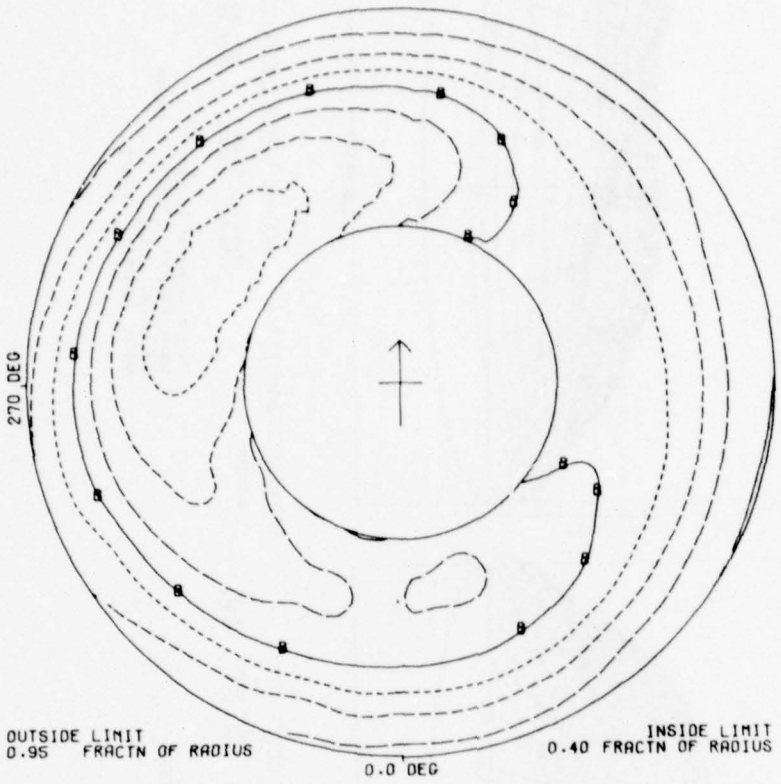

DERIVED PARAMETER - NORMAL FORCE COEFFICIENT

COUNTER 744

GROSS WT 8100. SHIP MODEL AH-1G
LONG CG 196.5 SHIP ID 20391

A —— 0.2 CN
B —— 0.6 CN

Figure 57A. C_N contour plot (90-degree right turn and acceleration to 70 knots).

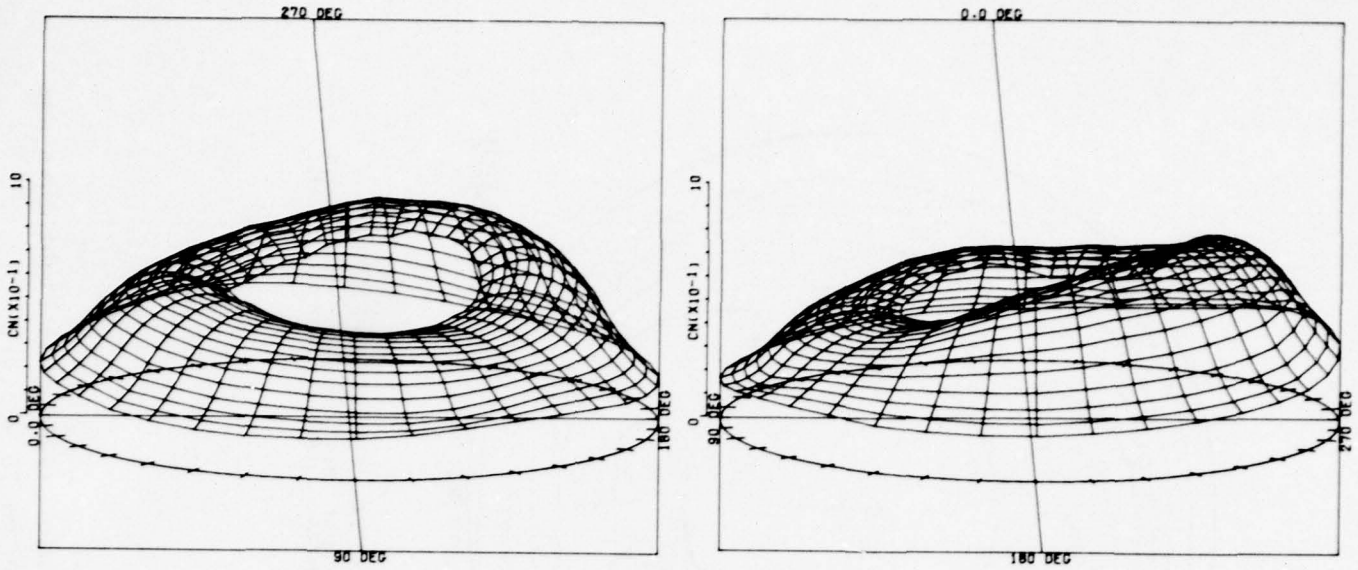

DERIVED PARAMETER - NORMAL FORCE COEFFICIENT

COUNTER 744 GROSS WT 8100 SHIP MODEL AH-1G
LONG CG 196.5 SHIP ID 20391

ANGULAR INCREMENT 10 DEG
RADIAL QUANTITY FRACTN OF RADIUS
MAX RADIUS 0.955
RADIAL INCREMENT 0.0370

DERIVED PARAMETER - NORMAL FORCE COEFFICIENT

COUNTER 744 GROSS WT 8100 SHIP MODEL AH-1G
LONG CG 196.5 SHIP ID 20391

ANGULAR INCREMENT 10 DEG
RADIAL QUANTITY FRACTN OF RADIUS
MAX RADIUS 0.955
RADIAL INCREMENT 0.0370

Figure 57B. C_N surface plots (90-degree right turn and acceleration to 70 knots).

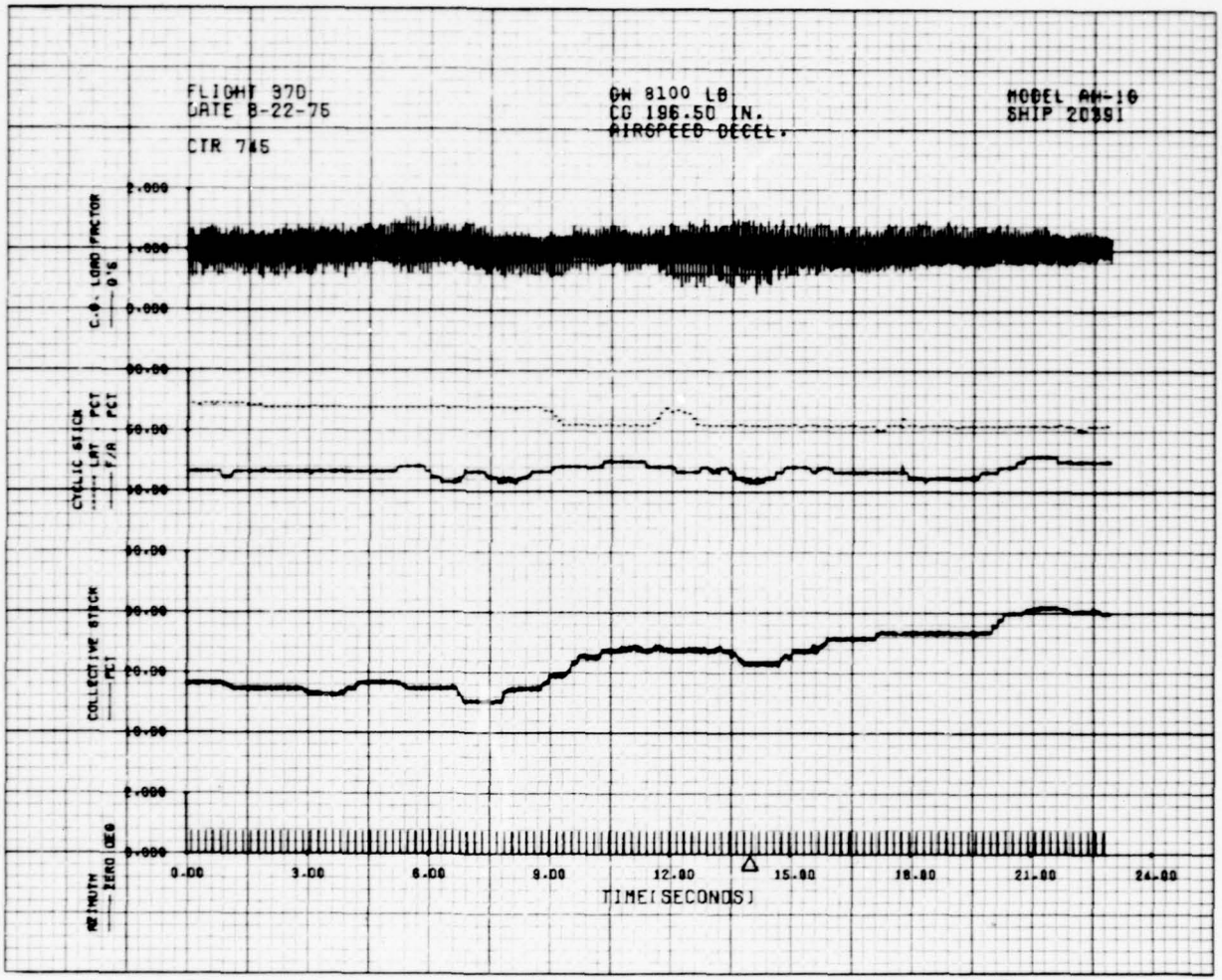

Figure 62. Load factor, cyclic and collective stick positions versus time (decelerate 50 knots to OGE hover).

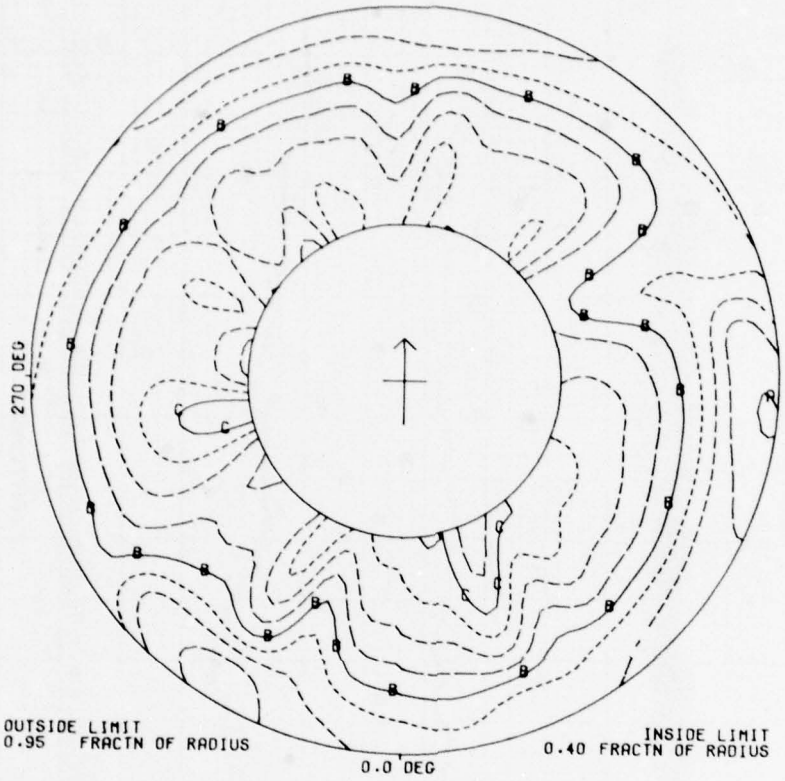

DERIVED PARAMETER - NORMAL FORCE COEFFICIENT

COUNTER 745

GROSS WT 8100. SHIP MODEL AH-1G
LONG CG 196.5 SHIP ID 20391

A 0.0 CN
B 0.4 CN
C 0.8 CN

Figure 63A. C_N contour plots (decelerate 50 knots to OGE hover).

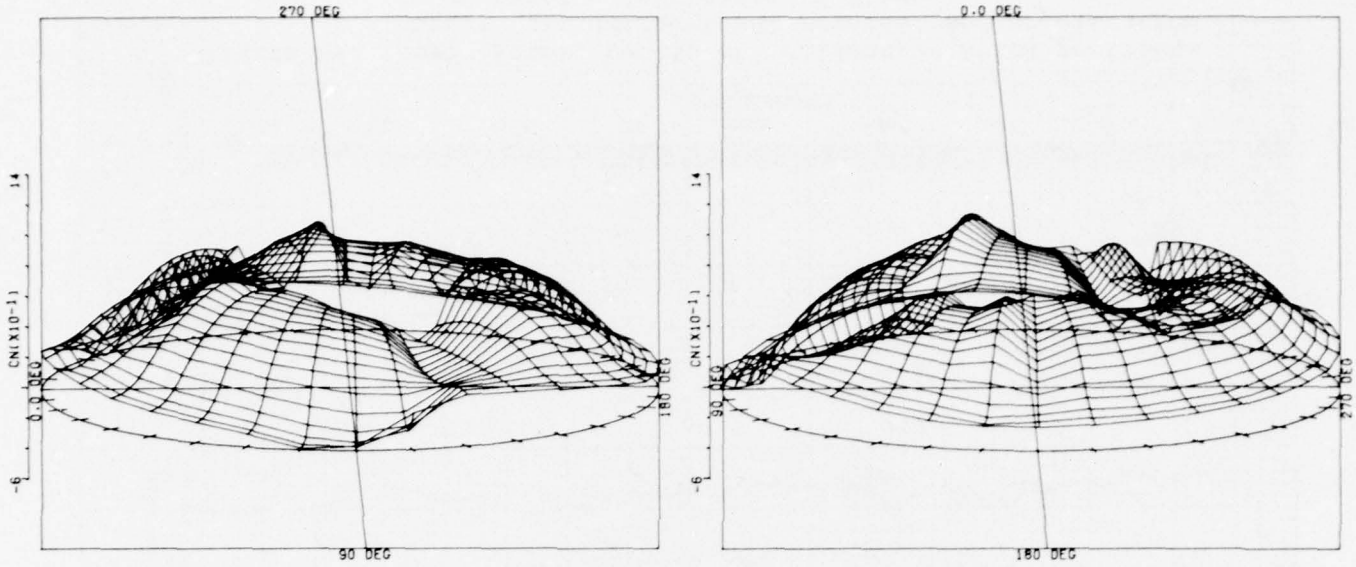

DERIVED PARAMETER - NORMAL FORCE COEFFICIENT

COUNTER 745 GROSS WT 8100 SHIP MODEL AH-1G
LONG CG 196.5 SHIP ID 20391

ANGULAR INCREMENT 10 DEG
RADIAL QUANTITY FRACTN OF RADIUS
MAX RADIUS 0.955
RADIAL INCREMENT 0.0370

DERIVED PARAMETER - NORMAL FORCE COEFFICIENT

COUNTER 745 GROSS WT 8100 SHIP MODEL AH-1G
LONG CG 196.5 SHIP ID 20391

ANGULAR INCREMENT 10 DEG
RADIAL QUANTITY FRACTN OF RADIUS
MAX RADIUS 0.955
RADIAL INCREMENT 0.0370

Figure 63B. C_N surface plots (decelerate 50 knots to OGE hover).

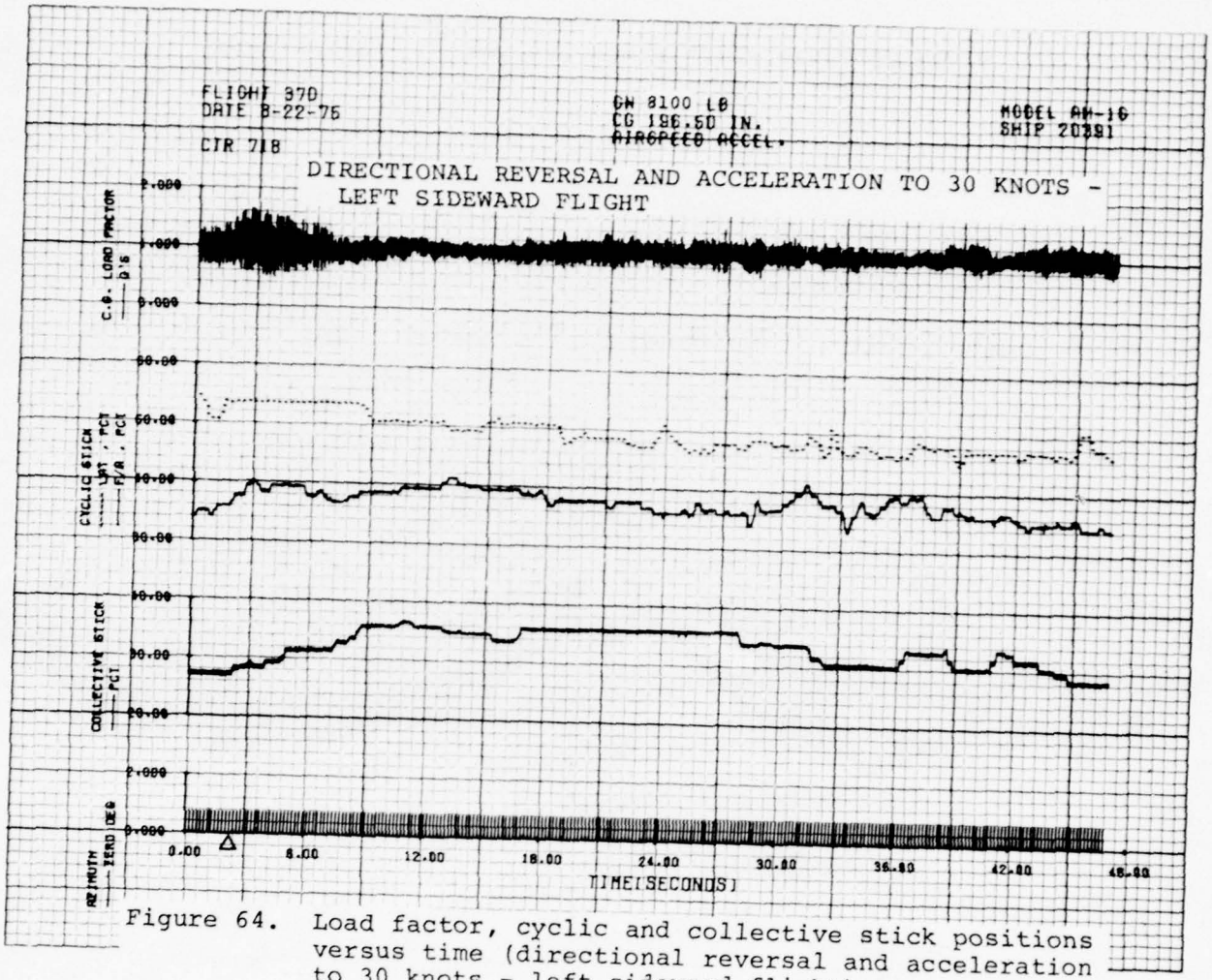

Figure 64. Load factor, cyclic and collective stick positions versus time (directional reversal and acceleration to 30 knots - left sideward flight).

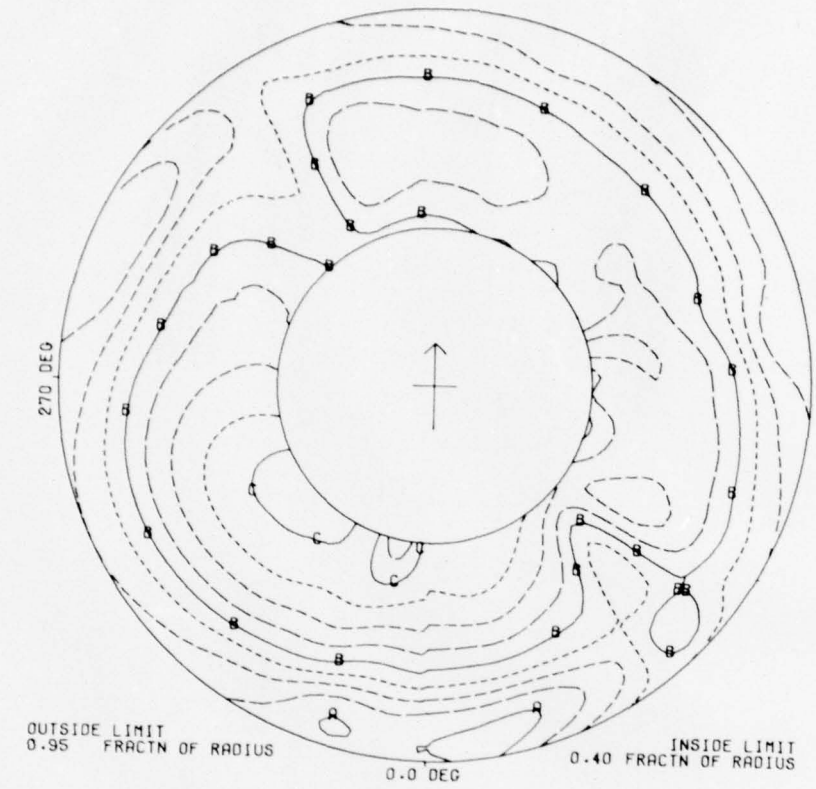

DERIVED PARAMETER - NORMAL FORCE COEFFICIENT

COUNTER 718

GROSS WT 8100. SHIP MODEL AH-1G
LONG CG 196.5 SHIP ID 20391

A 0.1 CN
B 0.5 CN
C 0.9 CN

Figure 65A. C_N contour plot (directional reversal and acceleration to 30 knots - left sideward flight)

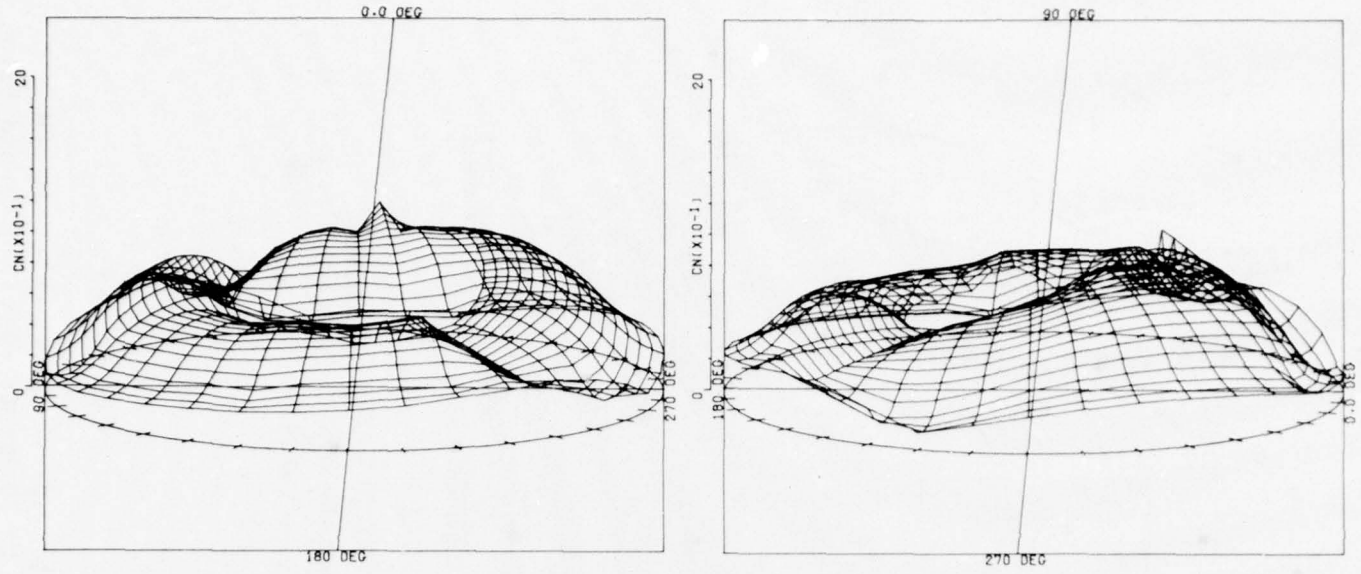

DERIVED PARAMETER - NORMAL FORCE COEFFICIENT

COUNTER 718 GROSS WT 8100 SHIP MODEL AH-1G
LONG CG 196.5 SHIP ID 20391

ANGULAR INCREMENT 10 DEG
RADIAL QUANTITY FRACTN OF RADIUS
MAX RADIUS 0.955
RADIAL INCREMENT 0.0370

DERIVED PARAMETER - NORMAL FORCE COEFFICIENT

COUNTER 718 GROSS WT 8100 SHIP MODEL AH-1G
LONG CG 196.5 SHIP ID 20391

ANGULAR INCREMENT 10 DEG
RADIAL QUANTITY FRACTN OF RADIUS
MAX RADIUS 0.955
RADIAL INCREMENT 0.0370

Figure 65B. C_N surface plots (directional reversal and acceleration to 30 knots - left sideward flight).

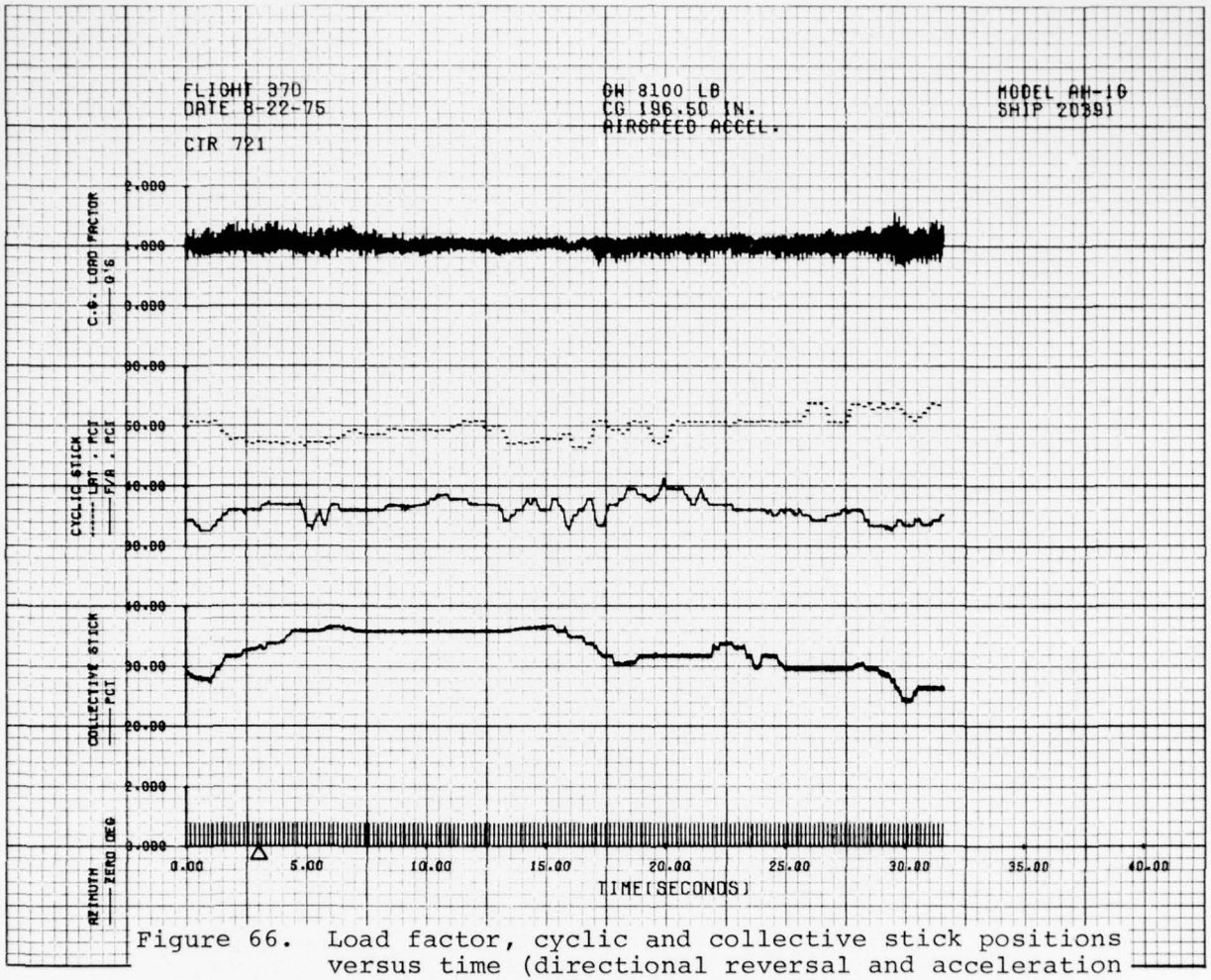

Figure 66. Load factor, cyclic and collective stick positions versus time (directional reversal and acceleration to 30 knots - right sideward flight).

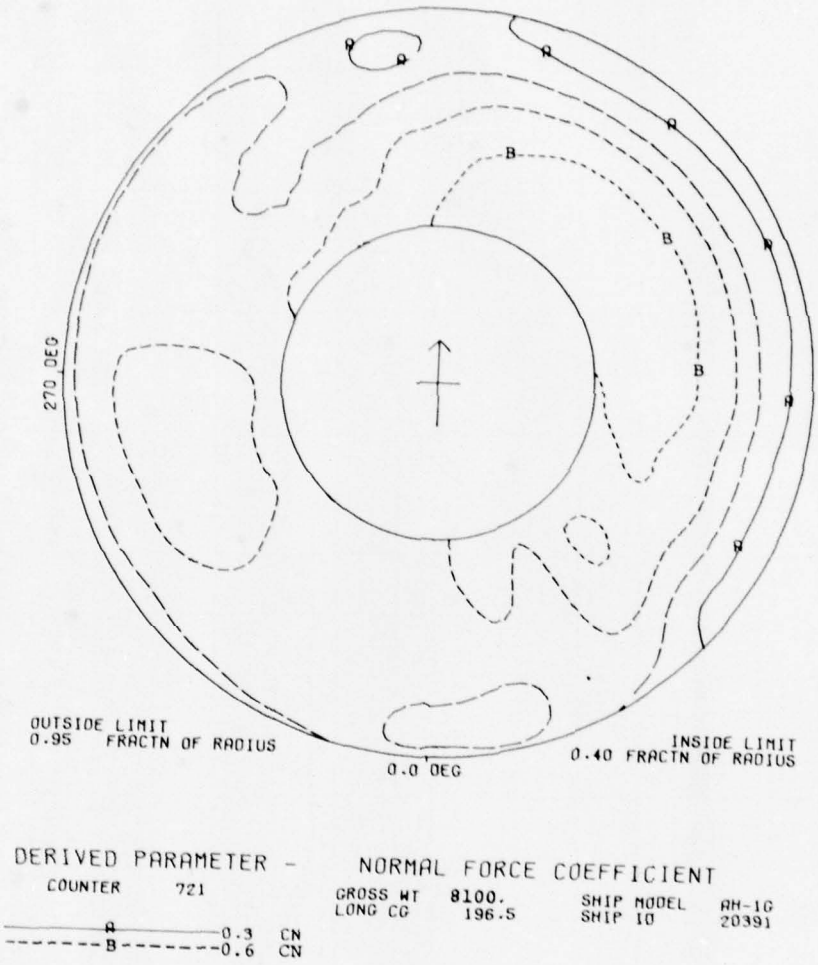

Figure 67A. C_N contour plot (directional reversal and acceleration to 30 knots - right sideward flight).

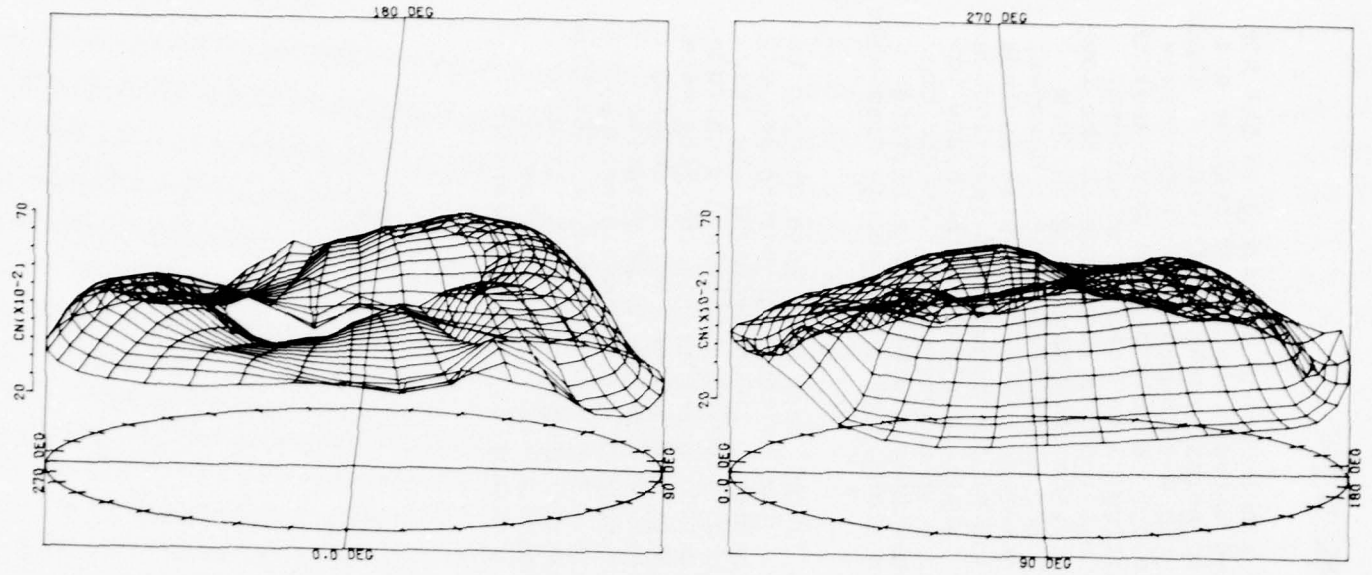

Figure 67B. C_N surface plots (directional reversal and acceleration to 30 knots - right sideward flight).

CONCLUSIONS

The aerodynamic behavior of a helicopter operating in the NOE flight region was illustrated through the use of contour and surface plots of the measured normal force coefficient. These plots should help stimulate the development of a more representative predictive methodology capable of providing analytical duplication of the resulting blade load distributions. Reasonable estimates of the net rotor performance in the low-speed flight region can usually be obtained using uniform inflow in conjunction with blade element analysis. However, the accurate prediction of detailed blade loads must include both an accurate determination of the nonuniform wake-induced inflow distribution and the proper reaction of the blade to discrete vortex interactions. These objectives dictate the use of an analytical approach that incorporates a lifting surface blade representation along with a compatible free-wake structure.

Certain deficiencies of the flight test data were brought to light in this investigation. Due to the high percentage of inoperative boundary layer buttons, it is difficult to draw conclusions regarding the local flow direction and magnitude. For all the flights investigated, one-third of the BLBs were inoperative. These BLBs positioned closest to the leading edge accounted for the largest percentage of inoperative gages. With respect to the angle-of-attack measurements, further studies are necessary. Presently, angle of attack is related to the hot-wire measured stagnation point through analytical means. A two-dimensional wind-tunnel test is necessary to determine the accuracy of this relationship.

REFERENCES

1. Tanner, W. H., and Yaggy, P. F., "Experimental Boundary Layer Study of Hovering Rotors," presented at the 22nd Annual National Forum of the American Helicopter Society, Washington, D. C., May 1966.

2. Tanner, W. H., and Van Wyckhouse, J. F., "Wind Tunnel Tests of Full-Scale Rotors Operating at High Advancing Tip Mach Numbers and Advance Ratios," Bell Helicopter Textron, USAAVLABS TR 68-44, US Army Aviation Materiel Laboratories, Fort Eustis, Virginia, July 1968, AD 674188.

3. Burpo, F., and Tanner, W. H., "Two-Dimensional Tests of Advanced Instrumentation for Rotors," Bell Helicopter Company Report Number 606-099-001, Fort Worth, Texas, December 1968.

4. Shockey, G. A., and Bowden, T. H., "A Wind-Tunnel Investigation of the Aerodynamic Environment of a Full-Scale Helicopter Rotor in Forward Flight," Bell Helicopter Textron, USAAVLABS TR 70-35, Eustis Directorate, US Army Air Mobility R&D Laboratory, Fort Eustis, Virginia, July 1970, AD 875744.

5. Shockey, G. A., and Bowden, T. H., "Evaluation of an Advanced Instrumentation System for Helicopter Rotors," Bell Helicopter Textron, USAAMRDL TR 71-72, Eustis Directorate, US Army Air Mobility R&D Laboratory, Fort Eustis, Virginia, February 1972, AD 740773.

6. Goodman, J., "Buildup and Test of a Rotating Frequency Division Multiplex System for Data Transmission from Rotating Systems," Bell Helicopter Company Report Number 0072R-001, Fort Worth, Texas, 5 January 1972.

7. Philbrick, R. B., and Eubanks, A. L., "Operational Loads Survey - Data Management System," Volume I - User's Manual, Bell Helicopter Textron, USARTL TR 78-52A, Applied Technology Laboratory, US Army Research and Technology Laboratories (AVRADCOM), Fort Eustis, Virginia, January 1979, AD A065129.

APPENDIX A
ROTOR FORCE AND MOMENT COEFFICIENT DATA

TABLE A-1. NOE STEADY FLIGHT CONDITIONS AND RECORD NUMBERS FOR PRESENTED NORMAL FORCE COEFFICIENT, CHORD FORCE COEFFICIENT AND PITCHING MOMENT COEFFICIENT DATA

Flight Conditions	Attitude (feet)	GW = 8100 LB CG (Mid) Flt/Record	
IGE Hover	-	37D	722
OGE Hover	100		723
Forward Flight At 10 KIAS	50		724
Forward Flight at 20 KIAS	50		725
Forward Flight at 30 KIAS	50		726
Forward Flight at 40 KIAS	50		727
Forward Flight at 50 KIAS	50		728

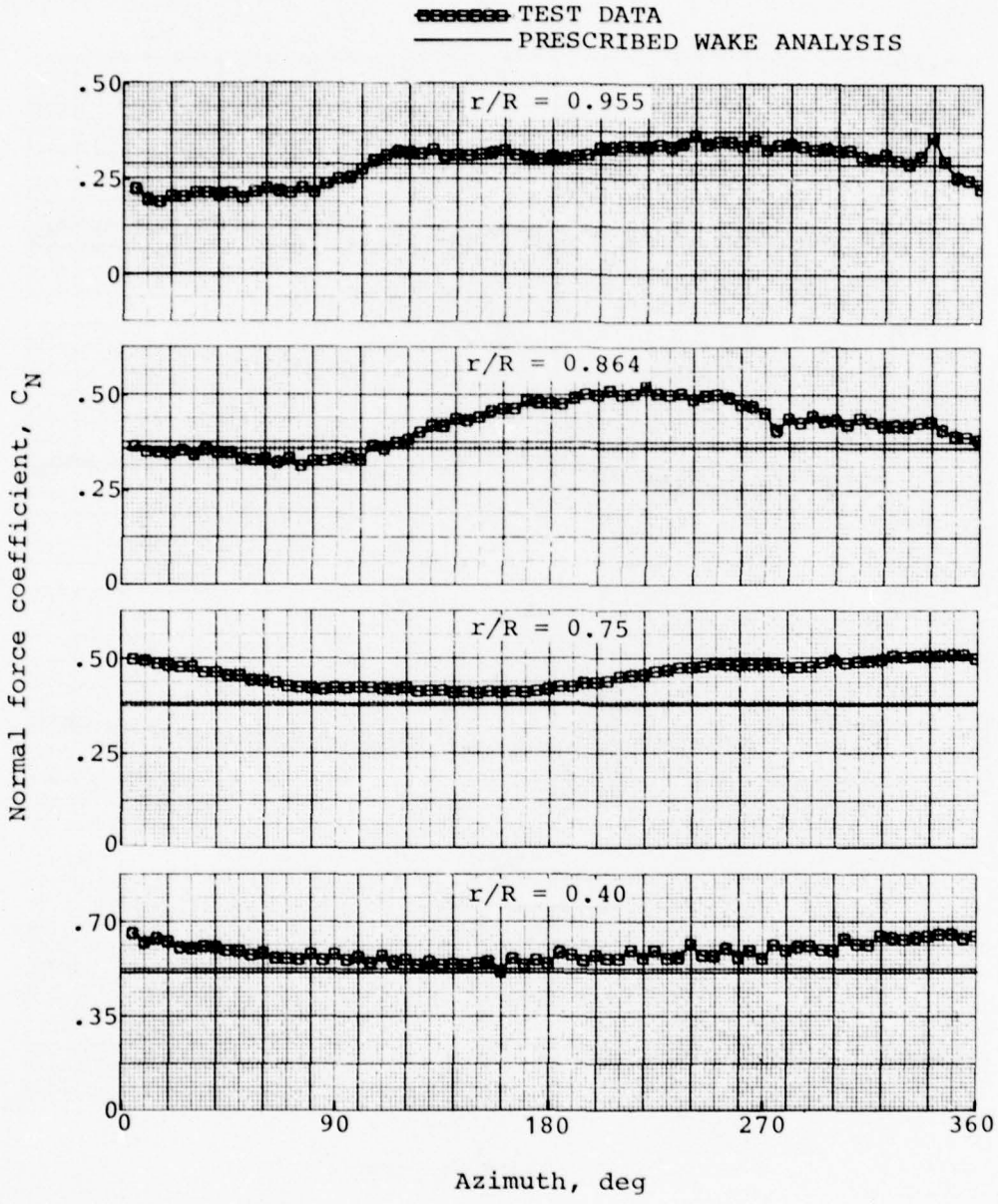

Figure A-1. Comparison of measured and predicted normal force coefficient, record 722, 8100 pounds gross weight, IGE hover.

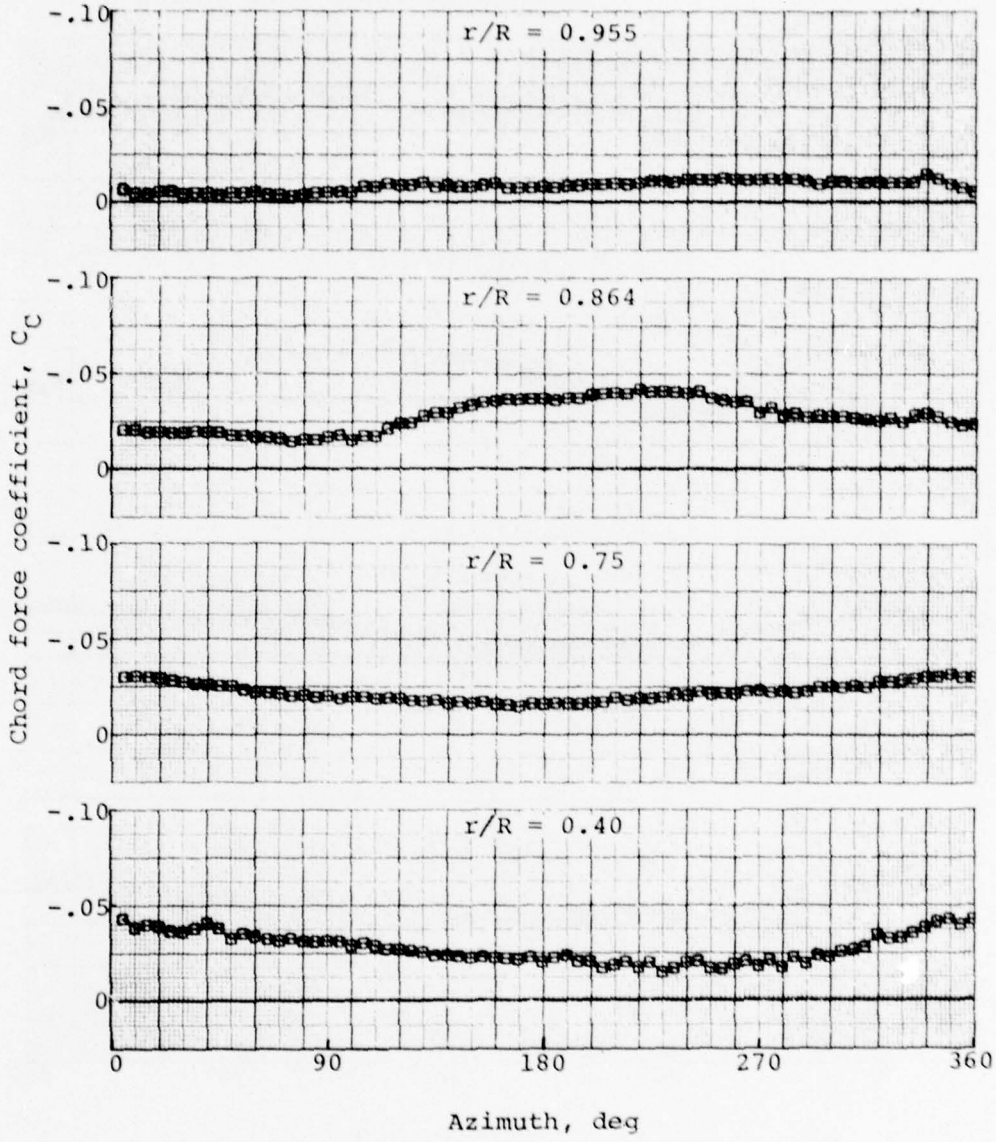

Figure A-2. Measured chord force coefficient versus azimuth, record 722, 8100 pounds gross weight, IGE hover.

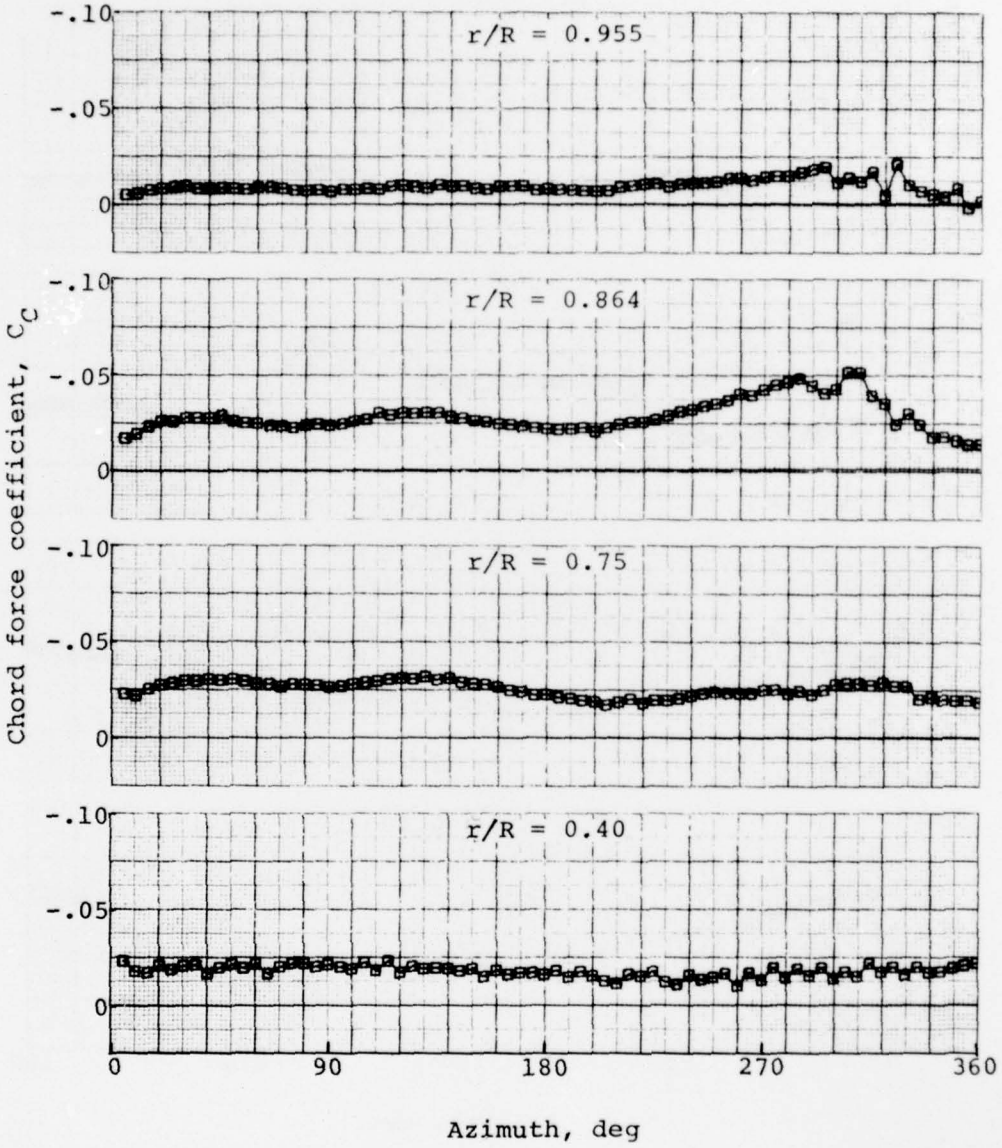

Figure A-3. Measured chord force coefficient versus azimuth. record 723, 8100 pounds gross weight, OGE hover at 100 feet.

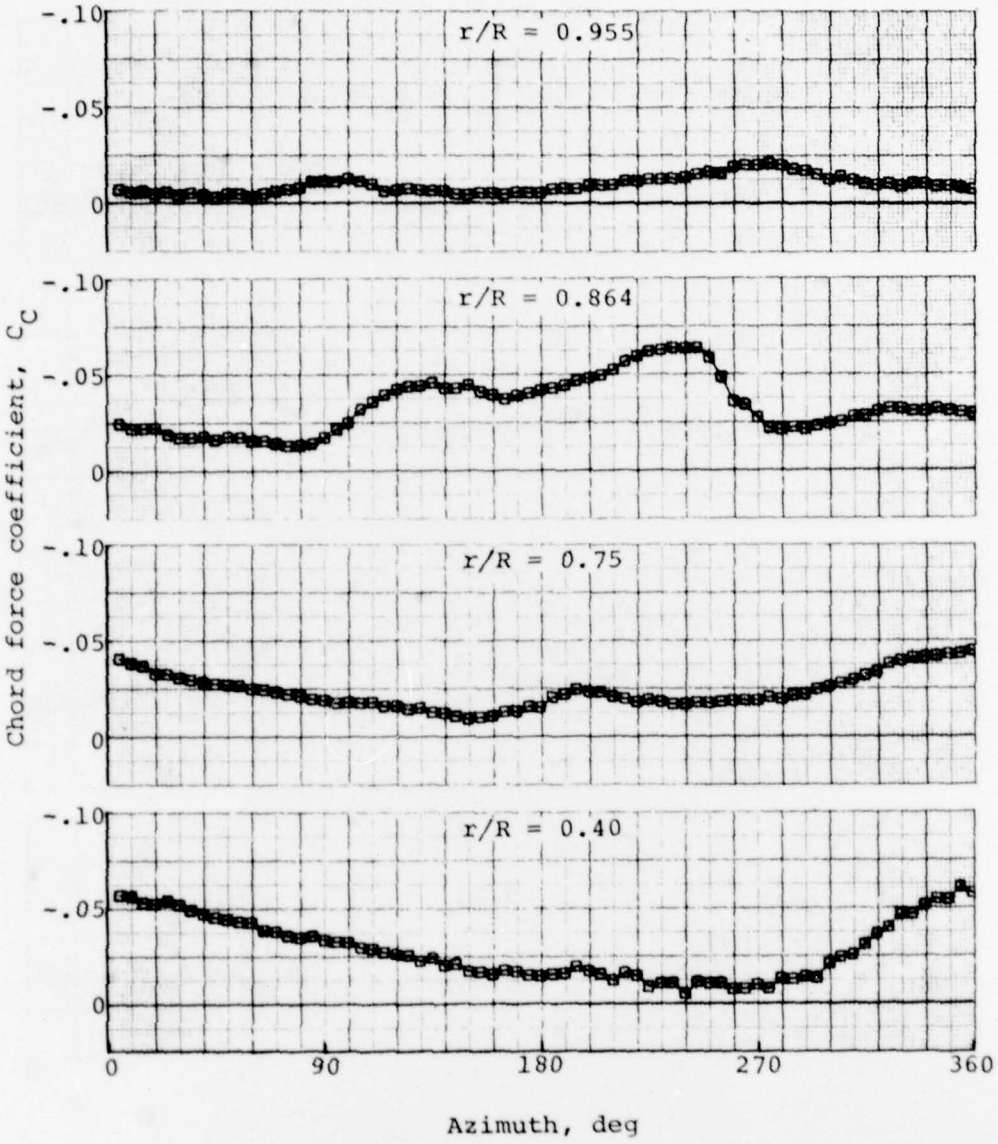

Figure A-4. Measured chord force coefficient versus azimuth, record 724, 8100 pounds gross weight, forward flight at 10 knots.

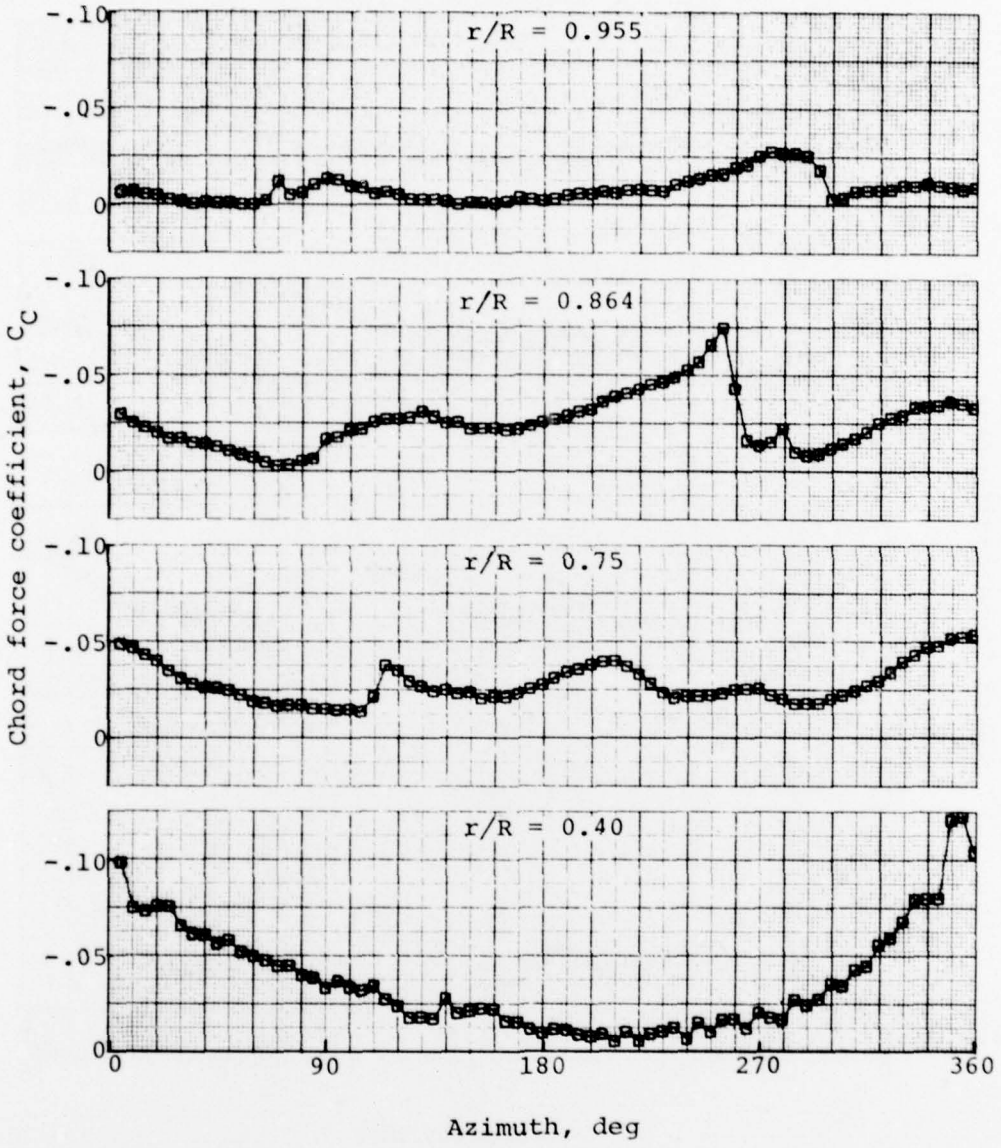

Figure A-5. Measured chord force coefficient versus azimuth, record 725, 8100 pounds gross weight, forward flight at 20 knots.

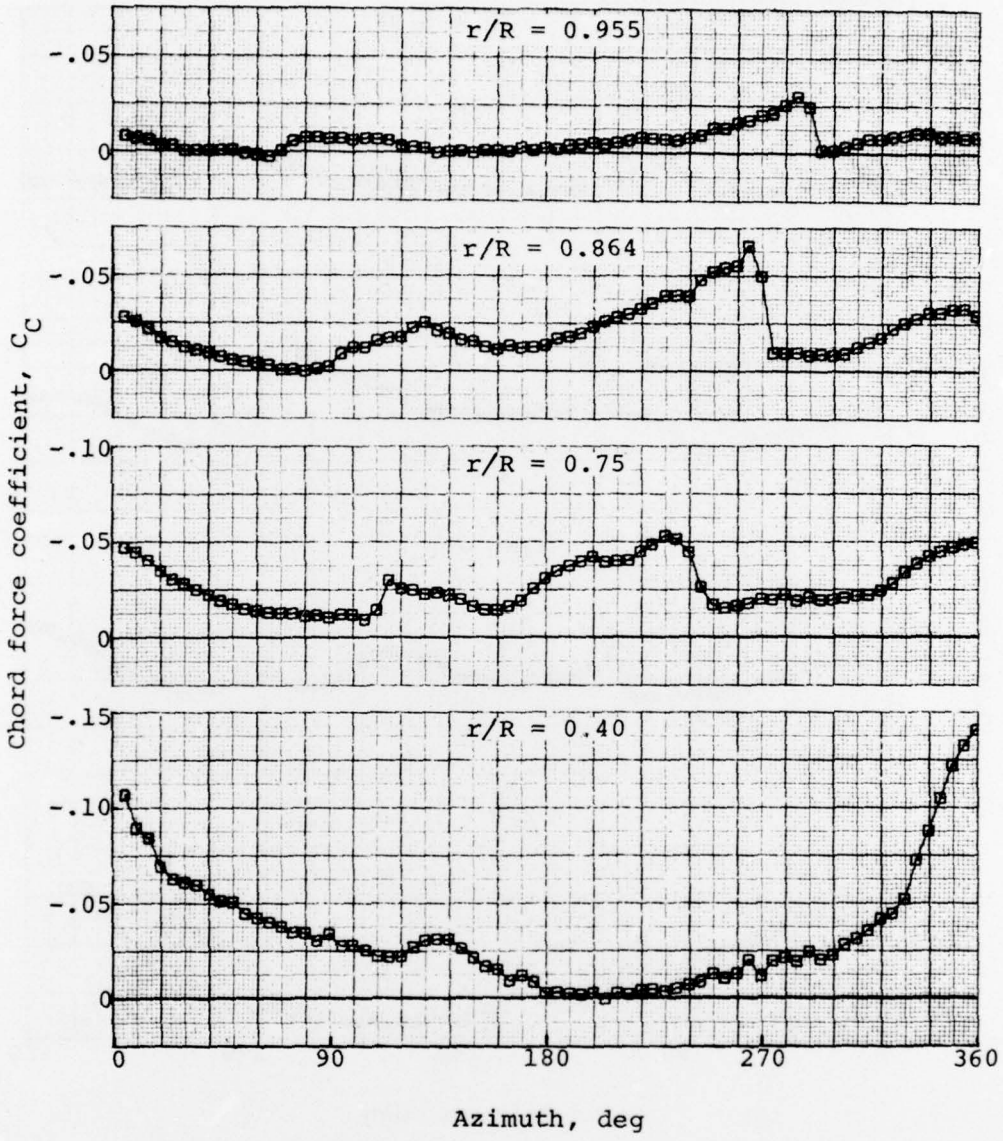

Figure A-6. Measured chord force coefficient versus azimuth, record 726, 8100 pounds gross weight, forward flight at 30 knots.

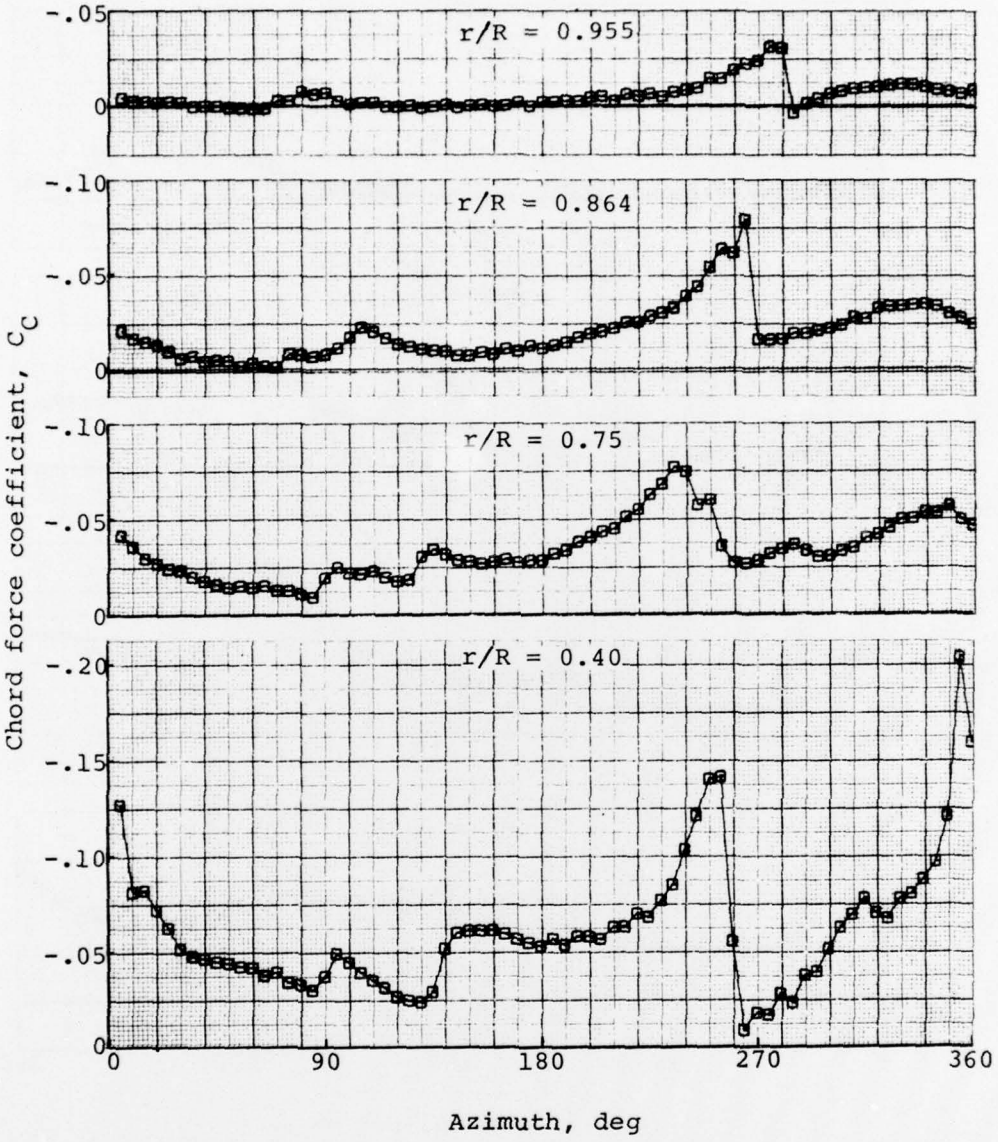

Figure A-7. Measured chord force coefficient versus azimuth, record 727, 8100 pounds gross weight, forward flight at 40 knots.

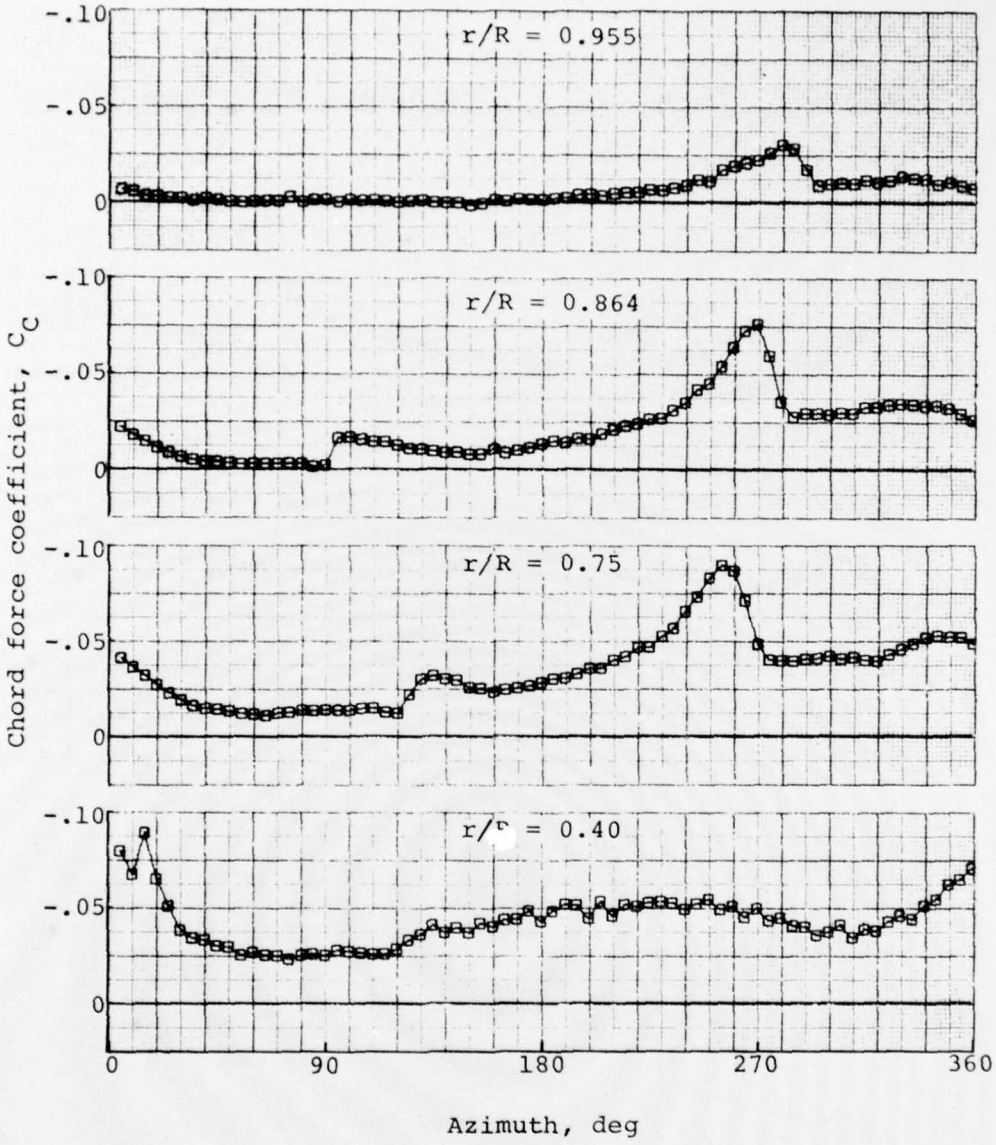

Figure A-8. Measured chord force coefficient versus azimuth, record 728, 8100 pounds gross weight, forward flight at 50 knots.

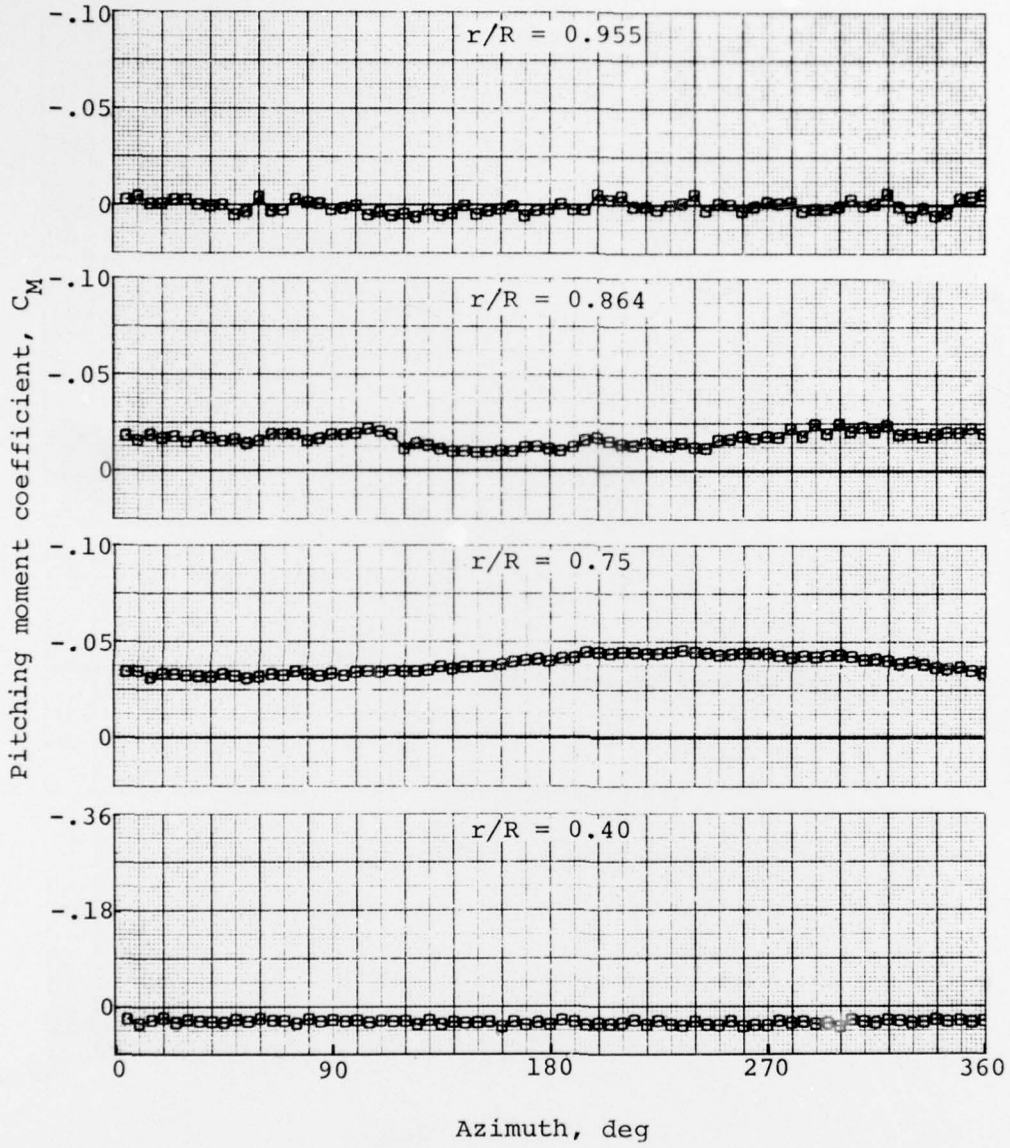

Figure A-9. Measured pitching moment coefficient versus azimuth, record 722, 8100 pounds gross weight, IGE hover.

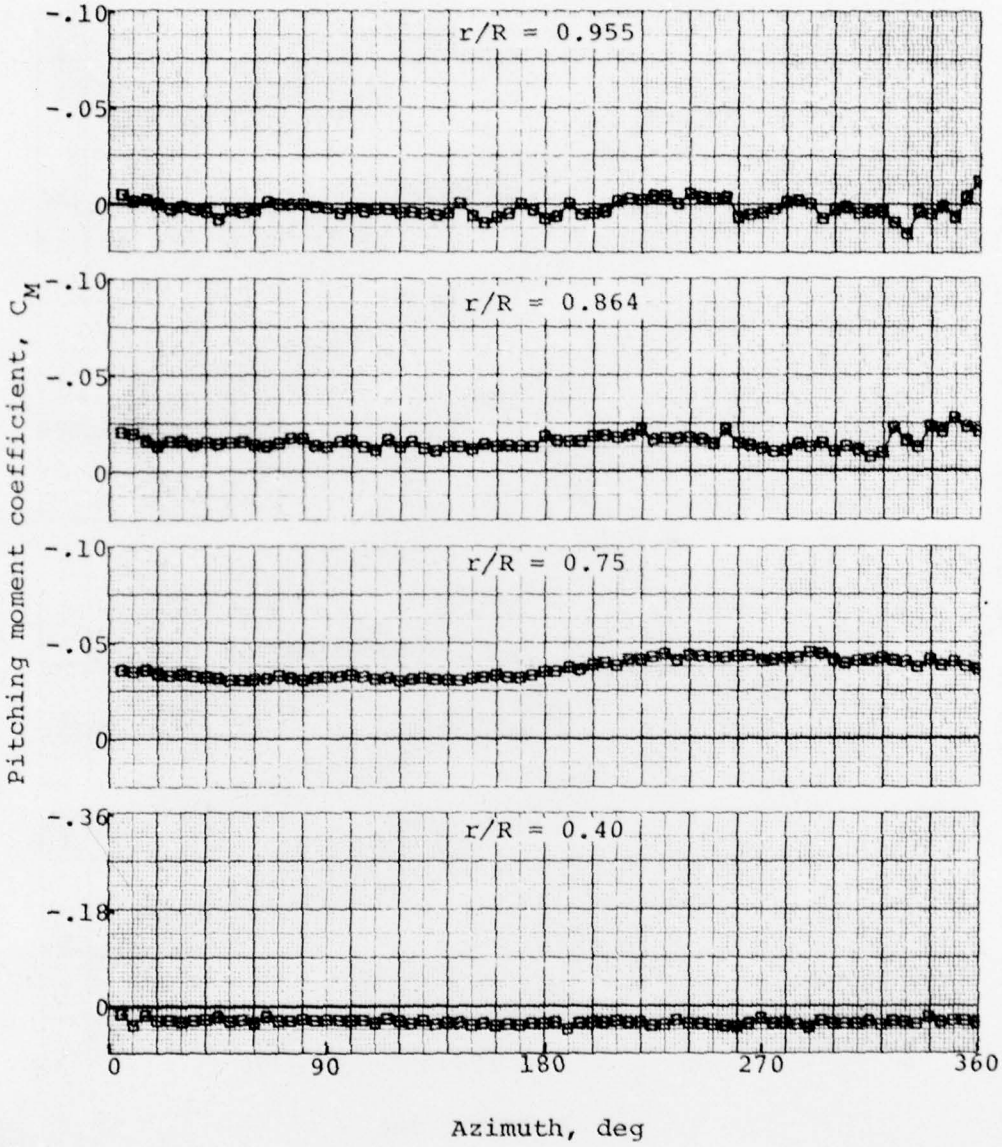

Figure A-10. Measured pitching moment coefficient versus azimuth, record 723, 8100 pounds gross weight, OGE hover at 100 feet.

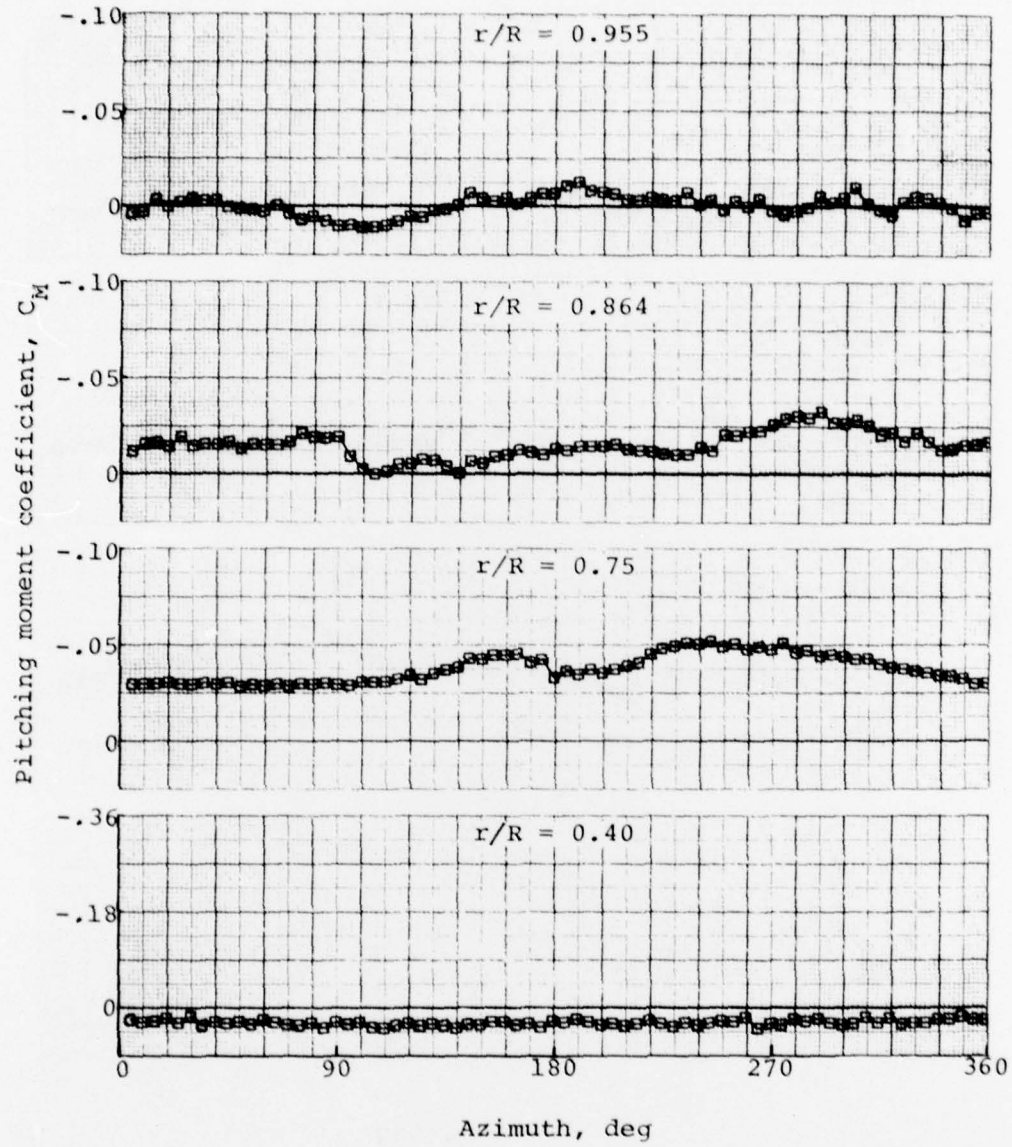

Figure A-11. Measured pitching moment coefficient versus azimuth, record 724, 8100 pounds gross weight, forward flight at 10 knots.

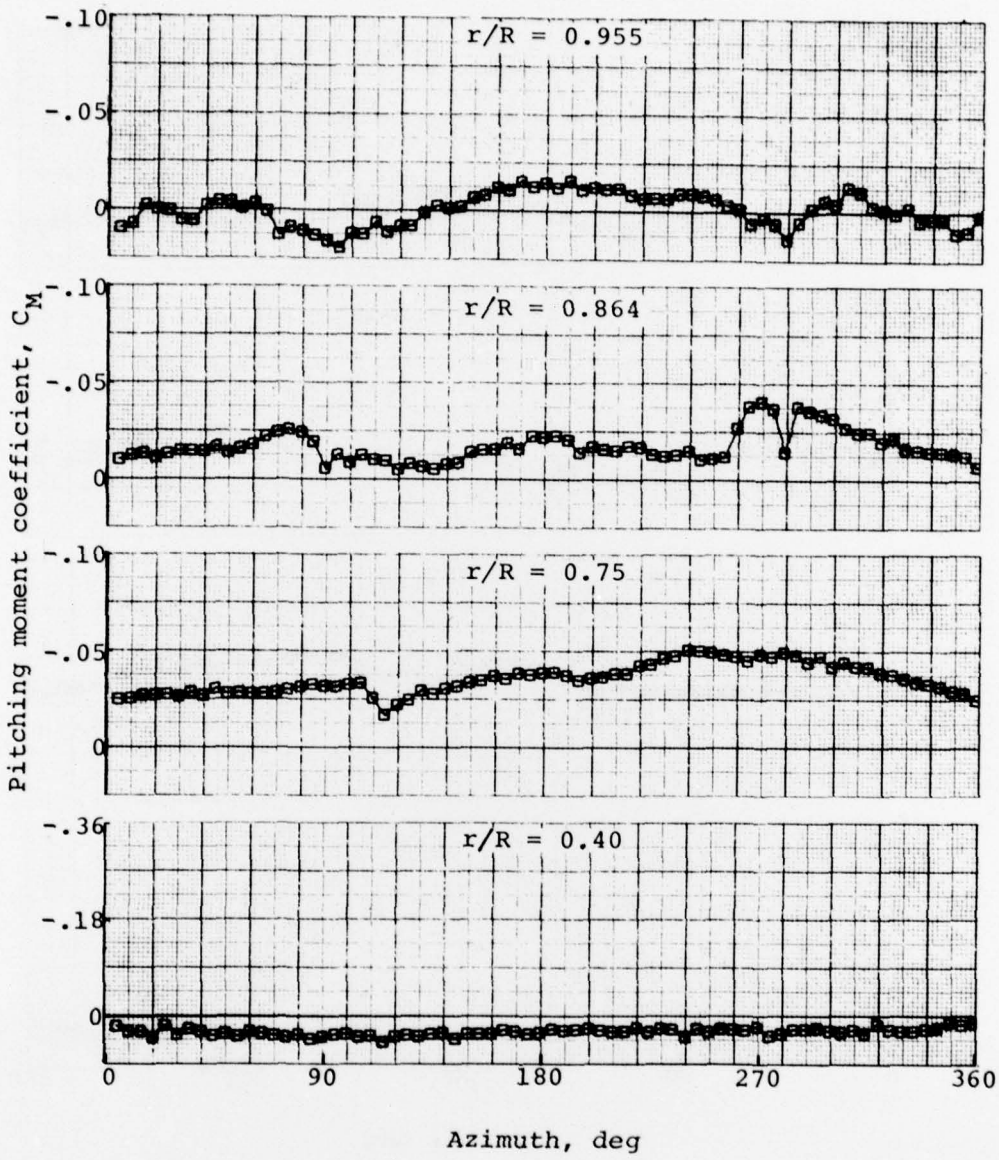

Figure A-12. Measured pitching moment coefficient versus azimuth, record 725, 8100 pounds gross weight, forward flight at 20 knots.

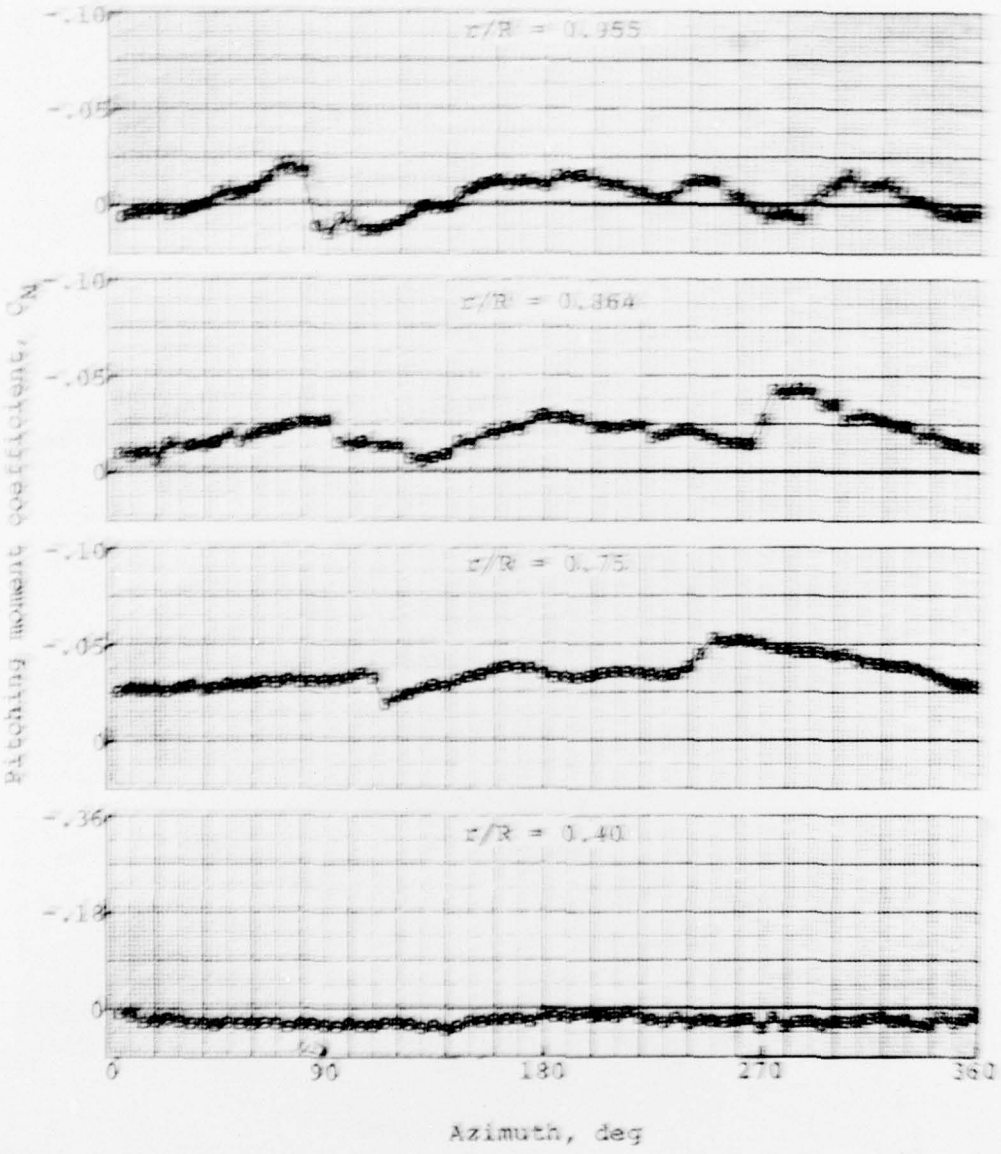

Figure A-13. Measured pitching moment coefficient versus azimuth, record 726, 8100 pounds gross weight, forward flight at 30 knots.

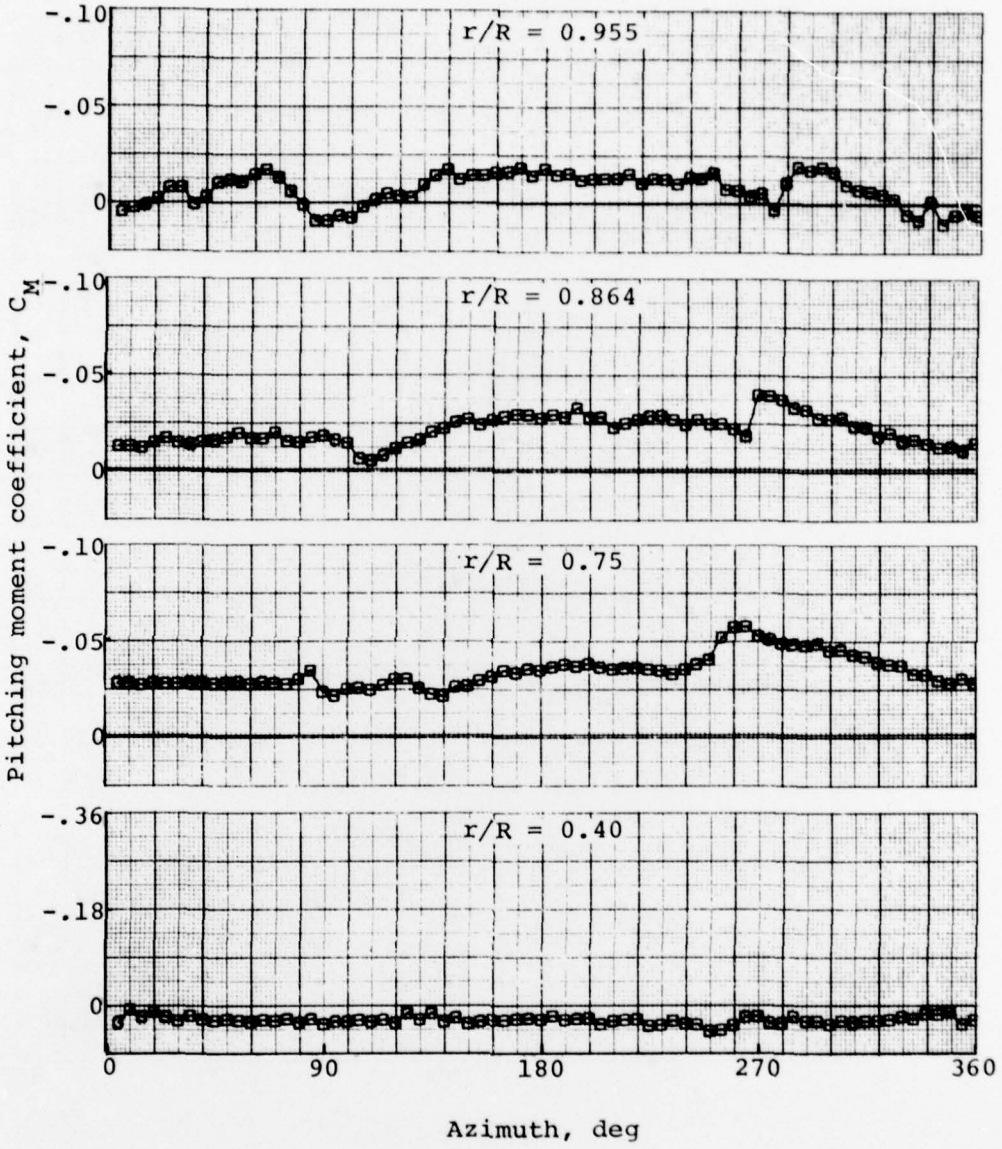

Figure A-14. Measured pitching moment coefficient versus azimuth, record 727, 8100 pounds gross weight, forward flight at 40 knots.

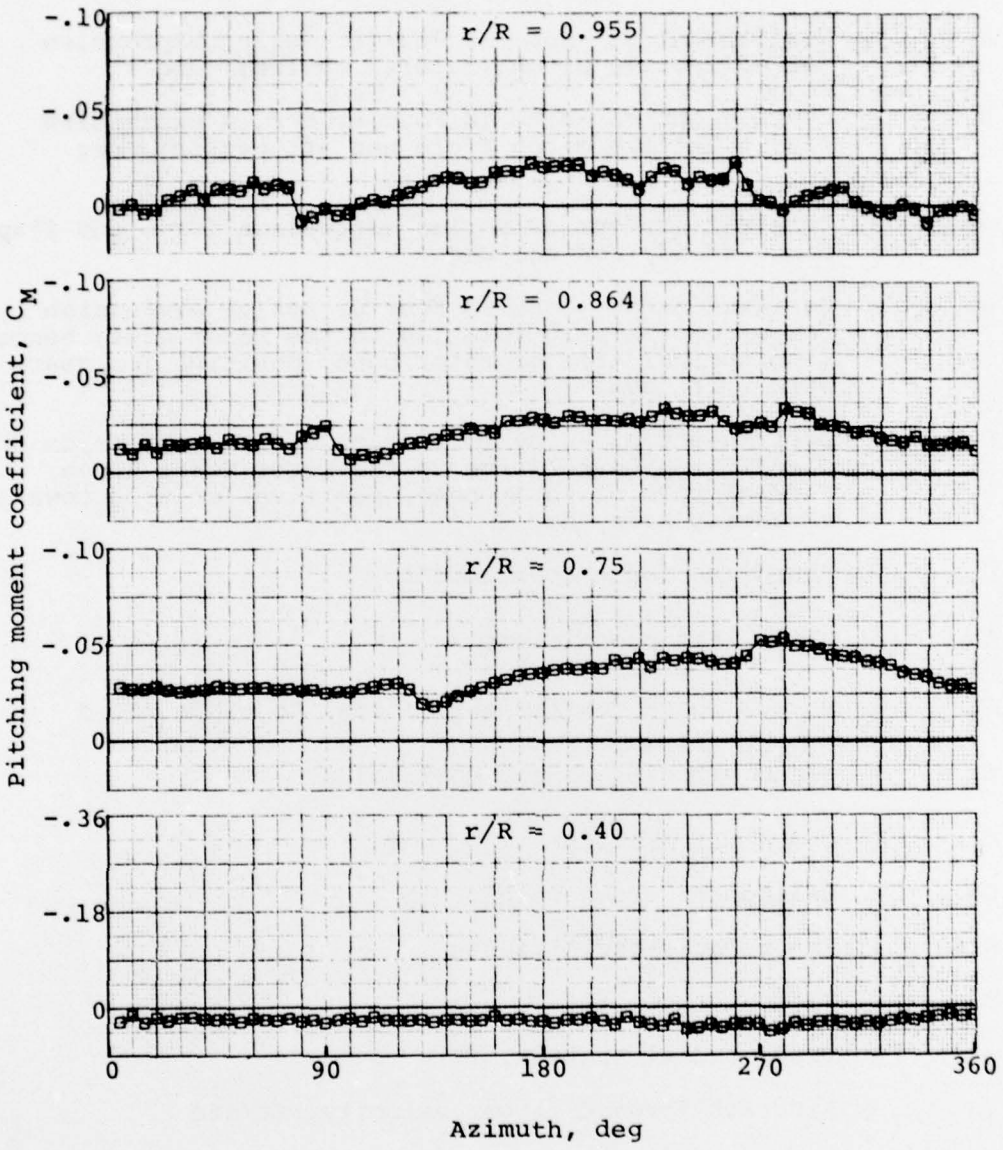

Figure A-15. Measured pitching moment coefficient versus azimuth, record 728, 8100 pounds gross weight, forward flight at 50 knots.

LIST OF SYMBOLS

A_{1_c} - Coefficient of -cosψ in Fourier series expression for collective pitch (lateral cyclic), deg

B_{1_c} - Coefficient of -sinψ in Fourier series expression for collective pitch (fore and aft cyclic), deg

a_o - Constant in Fourier series expression for blade flapping, steady coning, deg

a_1 - Coefficient of -cosψ in Fourier series expression for blade flapping relative to the rotor mast; hence, longitudinal tilt of rotor cone, positive for rearward tilt, deg

b_1 - Coefficient of -sinψ in Fourier series expression for blade flapping relative to the rotor mast; hence, lateral tilt of rotor cone, positive for tilt toward advancing side, deg

C_c - Chordwise force coefficient

C_L - Blade lift coefficient

C_N - Normal force coefficient, normal to blade chord

C_M - Blade pitching moment coefficient

cg - Center of gravity

GW - Helicopter gross weight, lb

KIAS - Knots Indicated Airspeed

R - Blade radius, ft

r - Blade radial station, ft

V - Aircraft forward flight velocity, ft/sec

X - Blade chordwise station, ft

θ_o - Blade collective pitch angle between plane normal to the shaft and zero lift line of the blade, deg

ψ - Blade azimuth angle measured from rearmost point of rotor in direction of rotation, deg

Ω - Rotor angular velocity, rad/sec